University of Alberta

Examination of Braided Composite Geometric Factors Using Three Dimensional Digital Image Correlation Measurement Techniques

by

Cheequn Leung

A thesis submitted to the Faculty of Graduate Studies and Research in partial fulfillment of the requirements for the degree of

Master of Science

Department of Mechanical Engineering

Fall 2012

Edmonton, Alberta

Abstract

The objective of this thesis is to develop and validate an optical measurement tool for composite braided structures and use this tool to examine important variables, braid radius and angle, under tensile loading and to perform initial studies.

Current deformation measurement techniques used on composite braids were reviewed. Techniques were compared to one another in terms of their ability to address difficulties specific to braided composites.

A digital image correlation based optical measurement system was used. Three tests were performed to determine the accuracy of the system. These include a rigid body motion test, a strain test, and a surface reconstruction test. Main sources of error of the optical measurement system are evaluated and discussed.

The braid radius and angle of tubular braided composites under tensile loading was assessed. The effects of braid radius and angle change on calculation of stress and elastic moduli are highlighted.

Table of Contents

List of Tables

List of Figures

Glossary :

- Braiding : A two dimensional composite preform manufacturing technique.
- Braid angle : The angle between the longitudinal and fiber strand travel direction of the braided composite.
- CC : Cross correlation.
- SCC : Stereo cross correlation.
- Closed mesh braid : A braid architecture with a tight meshing.
- CLPT : Classical laminated plate theory.
- Diamond braid : A 1x1 fiber strand crossover pattern braid architecture.
- Lamina : A thin composite layer.
- Meso scale: On the scale of a unit cell.
- Mandrel : A rod where fibers are arranged on to create a preform during braiding.
- Subset : A subdivision of an image in which digital image correlation calculations are performed.
- Unit cell : A repeating element in a braided composite which represents the general braided structure.
- **Nomenclature :**
- x, y, z : Global coordinate system.
- i, j : Local coordinates within a subset window.
- l, m: Pixel coordinates of an image.
- C_{cc} : The cross correlation criterion.
- M : The subset size in pixels.
- $f(l_i,m_j)$: A function describing the grayscale intensity of a reference image.
- $g(l'_i,m'_j)$: A function describing the grayscale intensity of a deformed image.
- $u(i, j)$: The displacement vector in the x-direction at coordinates (i, j).
- $v(i, j)$: The displacement vector in the y-direction at coordinates (i, j).
- $d_{i=0,1,2}$: Polynomial coefficients for least squares fitting.

- $e_{i=0,1,2}$: Polynomial coefficients for least squares fitting.
- p_1, p_2 : The coordinates for point 1 and point 2 respectively.
- a, b, b_1, b_2, c : Circle fitting equation coefficients.
- r : The outer surface nominal radius of a tubular braided composite.
- t : The wall thickness of a tubular braided composite.
- θ : The braid angle of a braided composite.
- Ex : Longitudinal elastic modulus of a braided composite.
- Ey : Transverse elastic modulus of a braided composite.
- Gxy : Shear modulus of a braided composite.

Chapter 1: Introduction

1.1 Motivation

Two dimensional composite braids are composed of reinforcing fibers, arranged in an angle-ply architecture, impregnated with a cured matrix. The reinforcing fiber strands of a composite braid are all interlocked leading to improved fatigue and impact resistance [1]. The interlocking fibers result in a rough uneven surface [2]. The use of composite braids is increasing and has been applied in the automotive, aerospace, sporting, and biomedical fields [3]. The design and application of composite braids is dependent on the accuracy of developed models describing composite braid behaviour.

Numerous models have been developed to predict the elastic constants of composite braids. A model was developed, by Carey et al. [4], based on classical laminated plate theory (CLPT) to determine the elastic constants of closed mesh 2D composite braids. The model was compared to other developed models and experimentally validated to a degree. A sensitivity analysis was then done to determine the sensitivity of elastic constants to elastic constants of the composite constituents [5]. A regression-based design model (RBDM) was developed to include open mesh braided composites [6]. The open mesh model was looked at with a focus on the effect of undulation length on elastic properties [7]. This study also attempted to experimentally validate the model through tensile testing of open mesh tubular composite braids.

Models provide a level of composite braid understanding but currently have limited experimental validation. Variables critical to elastic properties of tubular composite braids, as described in models [6, 8, 9], include radius, and braid angle. Current measurement techniques for these variables do not provide sufficient accuracy and consistency for design purposes. In addition the variables are held constant for calculations of stress and elastic properties. The influence of various loading conditions

on radius and braid angle has not been studied. Understanding how loading can affect these critical variables may help to explain the response of composite braids under loads and change how experimental data for composite braids is collected and interpreted.

1.2 Thesis Objectives

In this thesis, an optical measurement system based on 3D digital image correlation, will be developed and validated to characterize composite braid behavior under tensile loading conditions. This was undertaken as current measurement techniques are inadequate to assess critical dimensional variables, such as braid angle and radius, which are paramount in developing analytical models and fundamentally understanding braided composite elastic behaviour. These two key variables will be examined for Kevlar-Epoxy tubular composite braids as a function of tensile loading.

1.3 Thesis Scope

This thesis concentrates on the development of a measurement system to examine composite braid behavior under tensile loading conditions. It is a further focus to discuss the impact of these behaviours on theoretical and experimental work. Multiple measurement techniques are looked at to determine a technique that is capable of addressing measurement challenges inherent in composite braids. Tubular Kevlar epoxy composite diamond braids were evaluated.

1.4 Thesis Outline

This thesis is written in a paper format and consists of six chapters. Chapter 2 focuses on methods and techniques used to measure deformation of composite materials. The advantages and disadvantages of each technique are discussed and compared to one another. The application of the 3D Digital Image Correlation (DIC) optical measurement system on composite braids is developed and validated in Chapter 3. Three tests are

performed to determine the measurement system accuracy in body motion measurement, strain measurement, and tubular braid radius measurement from 3D surface reconstruction. A version of Chapter 3 was published at the CSME International Congress 2012. Chapter 4 evaluates the change in radius of tubular composite braids resulting from tensile loading, while in Chapter 5 the change in braid angle of tubular composite braids under similar loads is examined. Chapters 4 and 5 are written as individual papers for journal submission. Results are summarized in Chapter 6, as well as general conclusions and potential future work. A detailed description of the MATLAB programs used to measure braid radius and braid angle are provided in Appendix A.

1.5 References

[1] J. S. Tate, A. D. Kelkar, and R. Bolick, "Performance Evaluation of Notched Biaxial Braided Composites," *Vacuum*, pp. 20-23, 2004.

[2] J. J. Crookston, A. C. Long, and I. A. Jones, "A summary review of mechanical properties prediction methods for textile reinforced polymer composites," *Proceedings of the Institution of Mechanical Engineers, Part L: Journal of Materials: Design and Applications*, vol. 219, no. 2, pp. 91-109, Jan. 2005.

[3] P. Potluri, A. Manan, M. Francke, and R. Day, "Flexural and torsional behaviour of biaxial and triaxial braided composite structures," *Composite Structures*, vol. 75, no. 1–4, pp. 377-386, Sep. 2006.

[4] J. Carey, M. Munro, and A. Fahim, "Longitudinal Elastic Modulus Prediction of a 2-D Braided Fiber Composite," *Journal of Reinforced Plastics and Composites*, 2011.

[5] J. Carey, A. Fahim, and M. Munro, "Predicting Elastic Constants of 2D-Braided Fiber Rigid and Elastomeric-Polymeric Matrix Composites," *Journal of Reinforced Plastics and Composites*, vol. 23, no. 17, pp. 1845-1857, Nov. 2004.

[6] J. Carey, M. Munro, and A. Fahim, "Regression-based model for elastic constants of 2D braided/woven open mesh angle-ply composites," *Polymer Composites*, vol. 26, no. 2, pp. 152-164, Apr. 2005.

[7] C. Ayranci, D. Romanyk, and J. P. Carey, "Elastic Properties of Large-Open-Mesh 2D Braided Composites: Model Predictions and Initial Experimental Findings," *Polymer*, 2010.

[8] J. Carey, A. Fahim, and M. Munro, “Design of braided composite cardiovascular catheters based on required axial, flexural, and torsional rigidities.,” *Journal of biomedical materials research. Part B, Applied biomaterials*, vol. 70, no. 1, pp. 73-81, Jul. 2004.

[9] C. Ayranci and J. Carey, “2D braided composites: A review for stiffness critical applications,” *Composite Structures*, vol. 85, no. 1, pp. 43-58, Sep. 2008.

Chapter 2: Textile Composite Deformation Measurement Techniques

2.1 Introduction

Fiber reinforced plastic composites (FRPC), which consist of matrix and reinforcing fibers, are particularly beneficial because of their high specific stiffness and strength [1] and have seen an increased use in the aerospace, sports and biomedical fields [2]. Composite materials come in a variety of architectures, generally called textile composites, which have improved fatigue and impact resistance characteristics compared to laminate structures [3]. To best use composite materials and architectures in engineering design, an understanding of their behavior to applied loads is vital.

Braids are one of the oldest composite structures. In braided composites, contrary to laminates, strands are interlocked during the manufacturing process, thus improving load distribution and giving more balanced properties [3]. Interlocked fibers also remove the problem of delamination that occurs in composite laminates [4].

The surface of braided composite is generally rough due to the crossover and undulation of fibers tows [1], as can be seen for the diamond braided composite unit cell of Figure 2.1. The crossover regions produce peaks while the undulation regions create valleys. The epoxy does smooth the surface to an extent but is dependent on the amount of epoxy applied and the method of application. During matrix impregnation of fibers, the outside surface of the preform can be completely covered with a matrix layer [5] or be textured by the nature of the strand topology; this is seen in Figure 2.1, where ridges are clearly visible.

Figure 2.1 – A diamond braid composite architecture with a highlighted unit cell.

Properties of braided composites depend on braid angle, volume fractions, unit cell geometry, strand thickness and constituent materials [6]. When modeled, the elastic properties of braids are assessed based on a single unit cell and applied across the repeating structure [1]. It is therefore vital that when performing experimental work, for model validation, to determine elastic constants of braids accurately.

Composites are complex structures to assess for deformation and strain due to various geometric factors and composition, as noted above. It can be difficult to measure deformations as a result of surface features, large deformations, non-homogeneous strain fields or other factors [7].

Deformation measurement can give insight into composite structure behavior. Current deformation measurement techniques can be divided into contact and non-contact approaches.

The objective of this chapter is to investigate and compare the multiple deformation measurement techniques currently used for composite material starting by a general description of the techniques followed by a discussion of their applicability, benefits and weaknesses.

2.2 Deformation Measurement Techniques

2.2.1 Contact techniques

Strain Gauges

Strain gauges measure strain in the direction of alignment through the change in electrical resistance resulting from sample surface deformation. They provide deformation measurements over a sample surface at the location where they are permanently fixed to, making strain gauge measurements susceptible to local inhomogeneity [8]. The composite structure and materials can cause variations in deformation, for example when the fiber and matrix materials have very different stiffness [9]. To minimize the variations, larger strain gauges should be used and in the case of textile composites the strain gauge should extend beyond one unit cell. Strain gauges only measure local average strain at the location of placement and the direction of alignment. Conventional strain gauges have a maximum strain of ±3%.

Extensometers

Extensometers measure the average strain between two contact points on a sample surface. There are both contact and non-contact extensometers. Contact extensometers are clipped onto the sample, while non-contact extensometers use either lasers or video tracking of markers. Extensometers can give an average strain of the sample but cannot provide a full strain field. There are very few studies that use extensometers as the

primary method for measuring composite braid deformations. Rather they are used to verify the strain measured using other techniques such as interferometry or DIC.

2.2.2 Non-Contact Techniques

Interferometry

Interferometry has been used in many studies as a method of determining full field deformations in composites [10–20]. Interferometry measures the deformation of an object by recording the light field scattered from the object [14]. The scattered light field of an undeformed body will be different from that of the deformed body. By comparing the reference to deformed scattered light fields a displacement field can be extracted. There are specific types of interferometry such as Moiré, holographic, and electronic speckle pattern interferometry (ESPI). Moiré Interferometry can provide in-plane deformation, while holographic interferometry is focused on out-of-plane features.

Moiré interferometry requires the attachment of a grating to the sample surface. Laser light is diffracted off the grating producing a Moiré pattern. The deformed grating Moiré pattern is superimposed with an undeformed grating Moiré pattern resulting in a pattern that shows contours of displacement. The technique is capable of resolving displacements less than 1micrometer [21]. Strains, rotations, and shear strains can be determined [14]. The technique can provide full field strain data in real time [14].

Holographic interferometry is capable of creating three dimensional images of an object using the interference pattern generated between a reference and object beam [21]. If the object is deformed the deformation can be measured from a resulting pattern of interference fringes. However, there are strict requirements when recoding deformations over time. For real time measurements the object must be returned to the original position to prevent distortion of fringes. Another requirement is that applied displacements must

be expected and controlled. Unintentional displacements result in a loss of registration between the fringe pattern image and the object. This method has not been applied for the characterization of textile composites. However, it allows for the measurement of out of plane deformations that Moiré interferometry cannot.

ESPI uses laser light to illuminate an object and create a speckle pattern. The pattern is superimposed with a reference beam pattern from the same laser creating fringe patterns that can be used to determine deformation [21]. For this method interference fringe patterns are generated using electronic signal processing and computer techniques. Fringe patterns require unwrapping before they can be analysed. Deformation measurement resolution for ESPI is dependent on the wavelength of the laser being used which is in the nanometer range. A consistent laser wavelength is required as well as stability in the local environment. Temperature, humidity and vibration all need to be strictly controlled [15]. A compact sensor is fixed to the object eliminating problems associated with relative movement between the sensor and the object surface [22]. As a result ESPI does not suffer from previous methods inability to deal with rigid body motions.

Digital Image Correlation

Digital image correlation was developed by Peters et al. [23]. The DIC method can measure full field displacements in both two and three dimensions. The method first requires the application of a random speckle pattern to the surface of the region of interest [24]. The region is then successively imaged over the loading history of the sample. The applied speckling pattern is tracked through the successive images and correlated to give displacement vector fields. To track the patterns between a reference and deformed image, the images are divided into subsets. A correlation algorithm, which compares the grayscale intensities between a reference and deformed image, is applied to each subset to determine a location of maximum correlation. Equation (1) is a cross-

correlation criterion where functions *f* and *g* are the grayscale intensities of the reference and deformed image subsets [25], respectively. The subset size is given by the variable M. The index for the subset is given by *i* and *j*. The variables *l* and *m*, and *l'* and *m'* are coordinates of a point within the subset of the reference and deformed image respectively.

$$C_{cc} = \sum_{i=-M}^{M} \sum_{j=-M}^{M} [f(l_i, m_j) g(l_i^{'}, m_j^{'})] \quad (1)$$

The vector from the center of the subset to the location of maximum correlation is the displacement vector for that subset. With displacement measurements calculated from each subset of the grid, a full field vector displacement field can be created.

As previously mentioned, the DIC is capable of measuring full field displacements in both two and three dimensions; but there are differences in the setup for each scenario. A single camera is suitable for in-plane measurements (2D); however stereo imaging is required for out-of-plane measurements (3D). Stereo imaging can provide more information and is applicable to complex geometries; however the technique itself is more complex. Triangulation is used to determine the physical 3D surface points from images [26]. Three dimensional DIC is particularly useful for complex geometries; for example tubular braided composites, where the sample surface does not remain in a single plane.

2.3 Discussion

In this section, the use of these deformation measurement techniques in studies as well as their advantages and disadvantages will be discussed. The techniques will then be compared to one another in terms of their ability to address the challenges of measuring deformation in a fiber reinforced composite material.

Contact techniques were commonly used but have seen a decrease recently. A study by Harte and Fleck [27] measured the average strain response of composite tubes under compression with the use of strain gauges. Strain gauge rosettes with strain ranges of 20% measured strain in the axial and hoop directions. Strain gauges with large gauge lengths were used to minimize the effects of local inhomogeneous strains on the average value. To measure fiber direction strain, additional small strain gauges were applied to the surface of single tows. Large strain gauges may have the required gauge length to measure strains on composites. However, strain gauge size can become an issue and most strain gauges are unable to cover the required strain range [7]. Strain gauges do not cope well with surface damage [27].

A study by Juss et al. [24] obtained strain measurements with strain gauges and extensometers. Extensometers were clipped onto coupon specimens before the specimens were loaded. The measurements were used to compare and verify the accuracy of DIC technique. As with strain gauges, extensometers are not always able to cover the required strain range or deal with surface damage [7]. Also extensometers could not be clipped onto tubular specimens due to the lack of edges.

Non-contact measurement techniques have been increasingly used for composite research. There are many studies that have applied interferometry techniques to composites [15, 16, 18–20]. However, the studies focus on composite laminates rather than textile composites. Studies by Hale and Ifju [11, 12] utilized Moiré interferometry to examine the strain distribution in textile composites. Moiré interferometry displacement fields can be easily affected by irregularities in the composite architecture. Microcracking and broken fibers in the composite affect the displacement fields [11]. Misalignment of fibers can cause considerable scattering of experimental strains. When multiple affects are present it becomes difficult to interpret the data. Moiré interferometry is therefore

more effective for idealized two dimensional samples with minimal variation from expected fiber architecture.

A study by Amaro et al. [15] used ESPI for damage detection on laminated composites. Composite laminates were impacted with a drop weight test. Fringe patterns were generated and analysed to locate the presence of damage in the composite. Interferometry techniques do not require contact with a sample surface. They can measure deformations over an area and in real time with a resolution of less than 1micrometer. Measurements can be made in three dimensions and surfaces can be reconstructed. There are also limitations when applying interferometry techniques. Different interferometry techniques should be used depending on what measurements are desired. Each interferometry requires specialized equipment. Moreover, there is a high degree of equipment setup and specimen preparation required before these techniques can be applied. Most interferometry techniques have strict requirements to maintain system stability [28]. These requirements include consistent temperature, humidity, and laser wavelength, as well as any factors that can affect the laser. Processing times for interference fringe patterns are long. In addition, at high strains the fringe spacing becomes small, making the fringe patterns difficult to unwrap.

Many studies have used DIC to characterize the properties and behaviour of composite materials under different loading conditions. In these studies composite materials were tested in tension [29–34], bending [31, 35–37], under fatigue loading [38, 39] and internal pressure [40–42].

The majority of studies that characterize composites with 3D DIC involve examining composite materials in a state of tension. Studies by Ivanov [29, 30] examined triaxial braid characteristics and behaviour. Deformation fields were calculated from tensile test

images using DIC. The deformation fields were used to determine homogeneity, constitutive properties, orientation within the composite, onset of damage, and to validate finite element meso-scale models. The meso scale is on the scale of a braided composite unit cell. The noise associated with DIC was investigated. Results are most highly affected by noise during the initial stages of deformation. Unfortunately, this is often also the region of interest for composites as cracks can begin to appear at strains of 0.3% [30].

Berube [35] used DIC to strain map composite lamina under bending. Lamina samples were subjected to a four point bend test to determine flexural strength and modulus. This method was found to be effective for locating areas of damage on the composite surface and monitoring progression of failure.

In a study by Giancane [38] fatigue testing was performed on composite lay-up coupons with and without notches. The goal was to analyze damage onset and evolution. Samples were imaged repeatedly during cyclic loading. Using DIC, deformation maps were created from the images to follow damage evolution by identifying areas with concentrated strains. A similar study by Broughton [39] used composite coupons with holes in the middle. This study looked at the relation between damage evolution and load or loading cycles. The hole produces stress concentrations around it that were analysed by focusing DIC locally around these concentrations.

The last common test type using DIC is pressure testing of pipes, tubes or pressure vessels. Tung and Sui [41] studied composite tubes with a crack introduced into their pipe samples. DIC was used to examine the strain concentrations surrounding the manufactured crack in the pipe while subjected to internal pressure. Composite wrapped pressure vessels were investigated by Revilock [40]. The pressure vessels were subjected to internal pressures capable of causing failure to the pressure vessels. The pressurization

and bursting of the pressure vessel was imaged using DIC. The strain maps were able to show large increases in strain at locations of failure just before the vessels burst. Surface reconstructions were used to show the expansion of the pressure vessel resulting from pressurization.

The DIC method is non-contact, simplifying specimen preparation and removing errors that may come from surface effects or failure [43]. Full field measurement allows for heterogeneous testing. The gauge length can be adapted to match the scale of interest [44]. Depending on optics and software, the DIC method can range greatly in cost. There are also disadvantages to DIC. Setup time for a DIC system can be long. Appropriate optics and speckling must be selected depending on the desired measurement. Any change in the setup of the optics requires a new calibration. The calibration procedure is time consuming and can lead to inaccurate measurements if performed improperly. All measurements made using DIC are obtained from the captured images. Any factors that can affect the contrast of the captured images, for example shadows or reflections, can impact deformation measurements. These measurements describe the surface deformation of a sample, but cannot provide information as to what is occurring underneath the surface. The processing time for images is dependent on the resolution and number images, but is generally high.

The inhomogeneous nature of composites, grouped with the fiber interaction of textile architecture lead to non-uniform deformation fields. Many studies measured the deformation of composites using contact techniques such as strain gauges [7, 9, 24, 27], and extensometers [4, 7, 24]. Contact methods are able to average the deformation over a length, but are unable to give details regarding the specific deformations experienced over an area. Contact measurement systems are very susceptible to the substrate surface, which can be unevenly textured and incur damage during loading. The surface of a

composite can experience large strains and requires a measurement technique with a sufficiently large strain range [7]. These surface factors make attachment of measurement devices to the surface of a braided composite sample difficult, which can produce inaccurate readings, and may damage measurement devices.

A full field strain measurement technique can overcome the problems described with contact measurement systems by measuring strains over the entire or selected sample surface. Recently, an increasing number of studies have begun to use digital image correlation (DIC) [24, 26–47] and interferometry [11–14, 48–51], both of which are non-contact full field techniques. DIC is able to distinguish locations with strain concentrations and thus allow for filtering out spurious strains [37]. Strain concentrations and defects on composite surfaces can also be found in interferometry fringe patterns [15]. Interferometry techniques are able to resolve displacements on the nanometer scale in three dimensions with the proper laser wavelength [21]. DIC is also capable of resolving displacements of less than one micrometer in three dimensions but this is dependent on the resolution of the cameras and the optics setup used [25]. The stability requirements of interferometry are strict, limiting its use [52]. Rigid body motions can cause decorrelation between the object and reference beam which can affect the fringe patterns and thus, deformation measurements [21]. DIC can measure rigid body motions and discern between deformation and rigid body motion. Both ESPI and DIC can make out of plane measurements but require changes in equipment, optics, and test setup.

Many challenges are due to the surface of composites. Uneven surfaces and complex geometries make bonding and attachment of contact measurement devices difficult. Contact devices such as strain gauges and extensometers require removal before sample failure to prevent damage to the device [34]. Examining changes on the surface over time, for example failure or crack coalescing and propagation requires full field

deformation measurements [42]. DIC and Interferometry are non-contact and can provide full field deformation measurements. In addition, both techniques are capable of reconstructing the surfaces imaged in 3D for topographical measurements. The rough surface of textile composites can introduce challenges for optical measurement systems. The introduction of curvature, for example a tubular composite braid, can further complicate this. Surface roughness and curvature introduce shadows and reflections that can affect the speckling patterns and thus, DIC deformation calculations as well. This speckling pattern problem can potentially be alleviated by using a fluorescent speckling pattern as describe in a study by Berfield [46]. A certain depth of field is required to keep all features of surface roughness and curvature in focus. The optics used in DIC must take this into consideration. Depth of field is commonly not a problem for ESPI because the viewing systems used have a small aperture resulting in a large depth of field [21].

The region of interest and strain limit can differ greatly between each composite structure. Thus, it is beneficial for the technique used to easily adjust to any region of interest or strain limit. The size of strain gauges and extensometers can be adjusted to fit most regions of interest. However, properly sized strain gauges and extensometers may be limited for small regions of interest and may also be difficult to handle. Interferometry and DIC can be adjusted to fit any region of interest. For interferometry techniques such as ESPI, higher strains result in smaller fringe spacing. Compact fringe patterns resulting from sufficiently high strains become difficult to unwrap and analyse. The region of interest captured will depend on the optics used for both interferometry and DIC. Being a non-destructive technique with no upper strain limit, DIC is well suited to cyclic fatigue tests or testing of viscoelastic properties such as hysteresis [47].

As shown in a study by Tao [47], DIC is capable of giving strain measurements in real-time. This feature requires more computational power and thus a reduction in

measurement frequency. Tao successfully made strain measurements at 10Hz. Interferometry is also capable of providing real-time measurements [48].

Generally, contact techniques are less expensive. Interferometry cost is dependent on the desired accuracy of the measurement. A light source, a detector, optical equipment, a PC, post processing software, and stability requirement equipment are all required to perform interferometry. DIC cost is variable as the technique can be performed with even simple web cameras. However, if greater resolution is required over a small region of interest more expensive cameras and magnification may be required. The cost of both non-contact techniques is highly dependent on the desired measurements.

The setup time for the contact techniques is relatively short. Both strain gauges and extensometers require calibration to relate the voltage change to a strain. The devices then require attachment to the surface of a sample. The extent of post processing is short. The non-contact techniques require much more setup time. The equipment must be setup depending on the type of sample and type of measurement. The stability requirements for ESPI increase setup time. The systems then must be calibrated, which is a time consuming process. For DIC, if the position of the cameras used is shifted a new calibration procedure must be performed for that position. DIC requires that a speckling pattern be applied to the surface of a sample to create recognizable contrast. Post processing for both interferometry and DIC can be done with software. The processing times are dependent on the resolution of the images and the number of images captured, as well as the computational power of the computing device.

2.4 Conclusions

Deformation measurement challenges, including non-uniform deformation and surface features, of composite materials were presented. The advantages and limitations of

different deformation measurement techniques were assessed. These techniques are strain gauges and extensometers, as well as interferometry and digital image correlation.

Although contact techniques do not provide enough information to fully characterize complex composite architectures, measurements made at low strains have been shown to be reliable for composite materials. Contact measurement techniques are well established and understood. Thus, they provide good sources for comparison when attempting to verify the measurements made from non-contact techniques.

Interferometry and DIC share many advantages. They can both make full field deformation measurements in three dimensions. This allows both techniques to evaluate the inhomogenous deformation that occurs in braided composites and other composite architectures. Both are very adaptable techniques that can be adjusted for specific sample geometries and deformation resolutions. The light sources used for both interferometry and DIC are critical to reducing the noise in a system. The surface roughness of composite braids presents a problem for the lighting and speckling pattern applications when using DIC. Both interferometry and DIC have long setup times and potentially long post processing times.

The two non-contact techniques are both applicable to the evaluation of composite materials deformation. Braided composite unit cell sizes are on the millimeter scale. The nanometer range resolution makes interferometry good for small measurements but is not required for the deformations expected for braided composites. DIC can easily provide resolutions of 1micrometer, which is more appropriate for the evaluation of braided composite unit cells. The localized strains on a braided composite can be high. As long as the surface remains within the captured images, the DIC technique can measure these strains. High strains result in small fringe pattern spacing for ESPI and make unwrapping

and analysis of deformation difficult. Finally, the strict stability requirements of ESPI increase setup times and limit the usage of the technique. Overall, DIC is the more robust and applicable technique capable of braided composite deformation measurement.

2.5 References

[1] J. J. Crookston, A. C. Long, and I. A. Jones, "A summary review of mechanical properties prediction methods for textile reinforced polymer composites," *Proceedings of the Institution of Mechanical Engineers, Part L: Journal of Materials: Design and Applications*, vol. 219, no. 2, pp. 91-109, Jan. 2005.

[2] J. Carey, A. Fahim, and M. Munro, "Design of braided composite cardiovascular catheters based on required axial, flexural, and torsional rigidities.," *Journal of biomedical materials research. Part B, Applied biomaterials*, vol. 70, no. 1, pp. 73-81, Jul. 2004.

[3] J. S. Tate, A. D. Kelkar, and R. Bolick, "Performance Evaluation of Notched Biaxial Braided Composites," *Vacuum*, pp. 20-23, 2004.

[4] A. Harte, "On the mechanics of braided composites in tension," *European Journal of Mechanics - A/Solids*, vol. 19, no. 2, pp. 259-275, Mar. 2000.

[5] J. Carey, M. Munro, and A. Fahim, "Longitudinal Elastic Modulus Prediction of a 2-D Braided Fiber Composite," *Journal of Reinforced Plastics and Composites*, 2011.

[6] M. M. Shokrieh and M. S. Mazloomi, "An analytical method for calculating stiffness of two-dimensional tri-axial braided composites," *Composite Structures*, vol. 92, no. 12, pp. 2901-2905, Nov. 2010.

[7] M. Fouinneteau and A. K. Pickett, "Failure Characterisation of Heavy Tow Braided Composites Using Digital Image Correlation (DIC)," *Applied Mechanics and Materials*, vol. 5–6, pp. 399-406, 2006.

[8] J. E. Masters and P. G. Ifju, "Strain Gage Selection Criteria for Textile Composite Materials," *Society*, vol. 19, no. 3, pp. 152-167, 2012.

[9] E. Lang, "The effect of strain gage size on measurement errors in textile composite materials," *Composites Science and Technology*, vol. 58, no. 3–4, pp. 539-548, Apr. 1998.

[10] W. Q. Yin, N. M. Strickland, T. C. Chen, M. Haile, and P. G. Ifju, "Residual Stress Characterization of Plain Woven Composites," *Society of Experimental Mechanics*, 2009.

[11] R. Hale, “An experimental investigation into strain distribution in 2D and 3D textile composites,” *Composites Science and Technology*, vol. 63, no. 15, pp. 2171-2185, Nov. 2003.

[12] R. Hale and M. Villa, “Influence of Opposing Wave Nesting in Compression-Loaded Composites,” *Journal of Composite Materials*, 2011.

[13] P. Ifju, “The use of moiré interferometry as an aid to standard test-method development for textile composite materials,” *Composites Science and Technology*, vol. 53, no. 2, pp. 155-163, 1995.

[14] D. Post and B. Han, “Moire Interferometry,” in *Springer Handbook of Experimental Solid Mechanics*, 2nd ed., 1993, pp. 297-364.

[15] A. M. Amaro, P. N. B. Reis, M. F. S. F. de Moura, and J. B. Santos, “Damage detection on laminated composite materials using several NDT techniques,” *Insight - Non-Destructive Testing and Condition Monitoring*, vol. 54, no. 1, pp. 14-20, Jan. 2012.

[16] D. Van Hemelrijck, A. Makris, C. Ramault, E. Lamkanfi, W. Van Paepegem, and D. Lecompte, “Biaxial testing of fibre-reinforced composite laminates,” *Proceedings of the Institution of Mechanical Engineers, Part L: Journal of Materials: Design and Applications*, vol. 222, no. 4, pp. 231-239, Oct. 2008.

[17] J. P. Quinn, A. T. McIlhagger, and R. McIlhagger, “Examination of the failure of 3D woven composites,” *Composites Part A: Applied Science and Manufacturing*, vol. 39, no. 2, pp. 273-283, Feb. 2008.

[18] J. T. Ruan, M. Shen, J. W. Tong, S. B. Wang, F. Aymerich, and P. Priolo, “Experimental Investigation of Impacted and Non-Impacted Composite Laminates under Compressive Loading,” *Advanced Materials Research*, vol. 284–286, pp. 607-610, Jul. 2011.

[19] W.-C. Wang, C.-W. Su, and P.-W. Liu, “Full-field non-destructive analysis of composite plates,” *Composites Part A: Applied Science and Manufacturing*, vol. 39, no. 8, pp. 1302-1310, Aug. 2008.

[20] G. Kim, S. Hong, K.-Y. Jhang, and G. H. Kim, “NDE of low-velocity impact damages in composite laminates using ESPI, digital shearography and ultrasound C-scan techniques,” *International Journal of Precision Engineering and Manufacturing*, vol. 13, no. 6, pp. 869-876, May 2012.

[21] G. L. Cloud, *Optical Methods of Engineering Analysis*, 1st ed. New York, NY, USA: Press Syndicate of the University of Cambridge, 1995, p. 503.

[22] T. Siebert, H.-R. Schubach, and K. Splitthof, “Recent developments and applications for optical full field strain measurement using ESPI and DIC,” vol. 7997, p. 79972B-79972B-6, 2010.

[23] W. H. Peters and W. F. Ranson, “Digital Imaging Techniques in Experimental Stress Analysis,” *Optical Engineering*, vol. 21, no. 3, pp. 427-432, 1982.

[24] K. Juss, J. Kotlarski, and P. Mertiny, “Detection of Matrix Cracking and Leakage in FRPC Tubes through Digital Image Analysis.”

[25] B. Pan, K. Qian, H. Xie, and A. Asundi, “Two-dimensional digital image correlation for in-plane displacement and strain measurement: a review,” vol. 062001, 2009.

[26] J.-J. Orteu, “3-D computer vision in experimental mechanics,” *Optics and Lasers in Engineering*, vol. 47, no. 3–4, pp. 282-291, Mar. 2009.

[27] A. Harte, “Deformation and failure mechanisms of braided composite tubes in compression and torsion,” *Acta Materialia*, vol. 48, no. 6, pp. 1259-1271, Apr. 2000.

[28] P.-C. Hung and A. S. Voloshin, “In-plane strain measurement by digital image correlation,” *Journal of the Brazilian Society of Mechanical Sciences and Engineering*, vol. 25, no. 3, pp. 215-221, Sep. 2003.

[29] D. Ivanov, S. Ivanov, S. Lomov, and I. Verpoest, “Strain mapping analysis of textile composites,” *Optics and Lasers in Engineering*, vol. 47, no. 3–4, pp. 360-370, Mar. 2009.

[30] D. Ivanov, K. Vandenbosche, S. Ivanov, F. Baudry, S. Lomov, and I. Verpoest, “Strain mapping analysis of various textile composite and noise filtering of the data,” 2007.

[31] P. Carpentier and A. Makeev, “Novel Methods for Assessment of Three-Dimensional Constitutive Properties for Composites,” *Key Engineering Materials*, vol. 452–453, pp. 401-404, Nov. 2010.

[32] M. Karahan, “Investigation of damage initiation and propagation in 2 x 2 twill woven carbon/epoxy multi-layer composites,” *Textile Research Journal*, vol. 81, no. 4, pp. 412-428, Feb. 2011.

[33] X. Gao, W. Shao, and H. Ji, “Study on mechanical properties and damage behaviors of Kevlar fiber reinforced epoxy composites by digital image correlation technique under optical microscope,” *Symposium A Quarterly Journal In Modern Foreign Literatures*, vol. 7657, p. 76571L-76571L-6, 2010.

[34] J. Nader and H. Dagher, “3D Hybrid Ballistic Fabric Testing Using a 3D Digital Image Correlation System,” *Experimental Techniques*, vol. 35, no. 2, pp. 55-60, Mar. 2011.

[35] K. A. Berube and R. Lopez-anido, “Full-field Strain Measurements for Determining Mechanical Properties of Marine Composite Laminates,” *Mechanical Engineering*, pp. 2-9, 2008.

[36] A. Makeev, C. Ignatius, Y. He, and B. Shonkwiler, “A Test Method for Assessment of Shear Properties of Thick Composites,” *Journal of Composite Materials*, vol. 43, no. 25, pp. 3091-3105, Oct. 2009.

[37] R. Lopez-anido and L. Muszynski, “Image Correlation Analysis Applied to Measurement Laminated Composites of Shear Strains in,” pp. 163-166, 1980.

[38] S. Giancane, F. W. Panella, R. Nobile, and V. Dattoma, “Fatigue damage evolution of fiber reinforced composites with digital image correlation analysis,” *Procedia Engineering*, vol. 2, no. 1, pp. 1307-1315, Apr. 2010.

[39] W. R. Broughton, M. R. L. Gower, M. J. Lodeiro, G. D. Pilkington, and R. M. Shaw, “An experimental assessment of open-hole tension–tension fatigue behaviour of a GFRP laminate,” *Composites Part A: Applied Science and Manufacturing*, May 2011.

[40] D. M. Revilock Jr, J. C. Thesken, B. H. Suite, W. Conshohocken, and B. S. Forsythe, “3D Digital Image Correlation of a Composite Overwrapped Pressure Vessel During Hydrostatic Pressure Tests.”

[41] S.-H. Tung and C.-H. Sui, “Application of digital-image-correlation techniques in analysing cracked cylindrical pipes,” *Sciences-New York*, vol. 35, no. October, pp. 557-567, 2010.

[42] R. Scheuer and P. Mertiny, “Analysis of Surface Strains and Leakage Behavior in Composite Pipes and Vessels Using Digital Image Correlation Technique,” *Solutions*, pp. 1-7, 2009.

[43] F. Hild and S. Roux, “Digital Image Correlation: from Displacement Measurement to Identification of Elastic Properties - a Review,” *Strain*, vol. 42, no. 2, pp. 69-80, May 2006.

[44] A. Willems, S. Lomov, I. Verpoest, and D. Vandepitte, “Optical strain fields in shear and tensile testing of textile reinforcements,” *Composites Science and Technology*, vol. 68, no. 3–4, pp. 807-819, Mar. 2008.

[45] G. Nicoletto, G. Anzelotti, and E. Riva, “Mesoscopic strain fields in woven composites: Experiments vs. finite element modeling,” *Optics and Lasers in Engineering*, vol. 47, no. 3–4, pp. 352-359, Mar. 2009.

[46] T. A. Berfield, J. K. Patel, R. G. Shimmin, P. V. Braun, J. Lambros, and N. R. Sottos, “Micro- and Nanoscale Deformation Measurement of Surface and Internal Planes via Digital Image Correlation,” *Experimental Mechanics*, vol. 47, no. 1, pp. 51-62, Jan. 2007.

[47] G. Tao and Z. Xia, “A non-contact real-time strain measurement and control system for multiaxial cyclic/fatigue tests of polymer materials by digital image correlation method,” *Polymer Testing*, vol. 24, no. 7, pp. 844-855, Oct. 2005.

[48] H. Fein and P. Such, "Holographic Interferometry: Nondestructive tool," *Physics*, no. September, pp. 3-4, 1997.

[49] J. Lee, J. Molimard, A. Vautrin, and Y. Surrel, "Application of grating shearography and speckle shearography to mechanical analysis of composite material," *Composites Part A: Applied Science and Manufacturing*, vol. 35, no. 7–8, pp. 965-976, Jul. 2004.

[50] J. Lee, J. Molimard, A. Vautrin, and Y. Surrel, "Digital phase-shifting grating shearography for experimental analysis of fabric composites under tension," *Composites Part A: Applied Science and Manufacturing*, vol. 35, no. 7–8, pp. 849-859, Jul. 2004.

[51] P. Potluri, R. J. Young, K. Rashed, A. Manan, and Y. T. Shyng, "Meso-scale strain mapping in UD woven composites," *Composites Part A: Applied Science and Manufacturing*, vol. 40, no. 12, pp. 1838-1845, Dec. 2009.

[52] T. C. Chu, W. F. Ranson, and M. A. Sutton, "Applications of digital-image-correlation techniques to experimental mechanics," *Experimental Mechanics*, vol. 25, no. 3, pp. 232-244, Sep. 1985.

Chapter 3: Validation of DIC as an Effective Tool for Composite Tubular Braid Characterization

A version of this chapter has been published as: Leung, C. K., Melenka, G., Nobes, D. S., and Carey, J. P., "Validation of DIC as an Effective Tool for Composite Tubular Braid Characterization," *CSME International Congress 2012*, pp. 1-6, 2012.

3.1 Introduction

Braided composites are used in the biomedical, sports and aerospace fields as well as other applications [1]. They can offer high strength and stiffness to low weight ratio parts. In addition the properties of a braided composite are highly tailorable. To maximize the ability to design composite braid parts, our understanding of composite braid mechanical behaviours must be advanced. Measurement of the mechanical response of a braided fiber polymer composite is important in determining their mechanical behaviours. Many methods have been used to make these measurements on fiber reinforced polymer composites. They can be categorized as contact methods, which includes strain gauges [2–5] and extensometers [1, 2], or non-contact optical methods such as interferometry [6–8] and digital image correlation (DIC) [9–13].

Contact measurement methods are often used to provide averaged data over the measurement area. These devices are simple, reliable and well understood. They require a location of contact with test samples, which can be difficult to find on the potentially rough surface of a braided composite [2]. Strain gauges and extensometers are not always able to cover the required strain range or deal with surface damage [2] Braided composites are inhomogeneous structures, making it difficult to accurately describe meso-scale behaviour with averaged data [13, 14]. Non-contact optical measurement methods provide full field measurements, making these techniques particularly useful for heterogeneous materials such as composites [10]. In addition, full field measurements can

be more easily compared to mechanical models and thus can be used to validate such models [11]. These techniques are becoming commonly used in damage onset and crack propagation studies [3, 16]. This may lead to process control for industrial applications [10]. However, optical measurement techniques are not without limitations. They all require measurement system stability, as an instability could be inaccurately identified as components of mechanical behaviour in the region of interest [9]. There is also a high degree of data processing involved with these methods [9]. Non-contact methods are preferable for analysis of localized behaviour with full field measurements [12]. DIC requires a lower level of processing and can be done with simple equipment [17].

3.2 Digital Image Correlation

3.2.1 Basic Description

Two dimensional DIC, as described by Chu et al. [9], is a full field optical measurement technique that compares the grayscale intensities of subsequent images of a loaded sample to identify their corresponding relative motion and hence strain. Each image is divided into a grid of square subsets. A correlation algorithm is applied in consecutive images for each subset. Within the resolved 2D correlation function for each subset, the vector from the center of the region to the position of maximum correlation is resolved as the average displacement for that subset [18]. For 3D DIC, there are two cameras and thus two reference and correlated images [19]. The four images are correlated to each other to find the resulting displacement vectors in 3D. A smaller subset size will result in a higher density of vectors. Also, multi-pass and subset offset can be used to increase accuracy and spatial resolution.

Strain is measured by applying the pointwise local least-squares fitting technique to displacement fields. A square strain window is selected to calculate the strains at a point in the DIC calculated displacement field using equation (1) [20].

$$u(i,j) = d_0 + d_1 l + d_2 m$$
$$v(i,j) = e_0 + e_1 l + e_2 m \quad (1)$$

The local coordinates in the image are l and m, while coordinates within the strain window are given by i and j. The original displacements are $u(i,j)$ and $v(i,j)$. The polynomial coefficients to be determined are $d_{i=0,1,2}$ and $e_{i=0,1,2}$. The polynomial coefficients are solved using the least-squares method. Strain is calculated by comparing neighboring displacement vectors to one another, producing a displacement gradient that is strain.

Calibration is an important part of the DIC process. It allows the proper spatial scales to be applied to all images and gives the relative position and angle between the two cameras [19]. For this study of 3D DIC, a 2D calibration plate was used, which is sufficient for applying scales to in plane directions (x and y directions). To apply a scale in the out of plane direction (z direction), three images of the calibration plate were taken at a known distance interval in the z direction. The relation between image focus and location in the z direction can now be applied as the out of plane scale.

The objective of this study is to demonstrate that digital image correlation (DIC) is an applicable measurement tool for composite braid characterization. In addition, the feasibility of fluorescent speckling on braided composites for DIC is examined. The study outlines three tests conducted to validate the use of DIC for analyzing the mechanical response of braided composites. The purpose of these tests was to evaluate DIC accuracy in measuring rigid body motion, strain measurement, and 3D surface reconstruction. The results from the tests are presented and discussed.

3.2.2 Sources of Measurement Error

There are sources of error that affect the DIC measurement system. The stereomicroscope set the relative camera angle between the two cameras at approximately 6˚. The relative camera angle was determined from a relative camera geometry model, which was calculated using a pinhole camera model [21]. A shallow relative camera angle decreases the out-of-plane resolution and increases displacement errors [22]. A drop in relative camera angle from 45˚ to 10˚ increases the *z* displacement error from 4% to 13% [22].

Another source of error stems from using a 2D calibration target for a 3D calibration. In-plane scales are set by the calibration target dot spacing. However, out-of-plane scales were set by shifting the calibration plate in the *z*-direction by 25.4μm increments using micrometer translation stages with 12.7μm minimum resolution. Misalignment of the translation stage with the *z*-direction can cause further discrepancy between the expected and actual motion applied to the calibration target. This affects the applied *z*-scale and decreases the accuracy of out of plane calculations such as *z*-displacement and surface reconstruction.

Measurement errors can also come from the cross-correlation algorithm. A small subset size reduces correlation quality, whereas larger subsets increase correlation quality but decrease the displacement vector field density [10]. The speckle size can also influence determining the location of correlation peaks. A study by Synnergren [23], suggests a mean speckle size of 2 pixel diameters to minimize this error. Uniform lighting conditions are required for correlation. Increasing luminosity increases the errors, while decreasing luminosity decreases the errors until correlation is not possible [10]. The overall error for strain measurement can be determined by applying rigid body motions and measuring the strains [10].

3.3 Procedure and Methods

3.3.1 Experimental Setup

The camera system used to capture images is shown in Figure 3.1. The system includes a 3-axis traverse, two CCD cameras (LaVision Imager Intense, LaVision GmbH, Göttingen, Germany), and a stereo microscope (Zeiss Stereo Discovery V8, Carl Zeiss MicroImaging Gmb, Göttingen, Germany). Lighting was provided by a 2.64" ring light (Edmund Optics, Barrington, NJ, USA) with a 365nm black-light (Edmund Optics, Barrington, NJ, USA). A Commercial software (DaVis version 8.0.6 StrainMaster 3D, LaVision GmbH, Göttingen, Germany) was the DIC software used to convert captured images into surface maps and full field measurements. The array size for the cameras is 1376x1040 pixels. For the current work when an image is spatially scaled the relation is ~162 pixels per millimeter. An interrogation window of 64x64 was used for DIC processing and has a resolution of 0.025 pixels. The resolution of the camera system is 1.54µm.

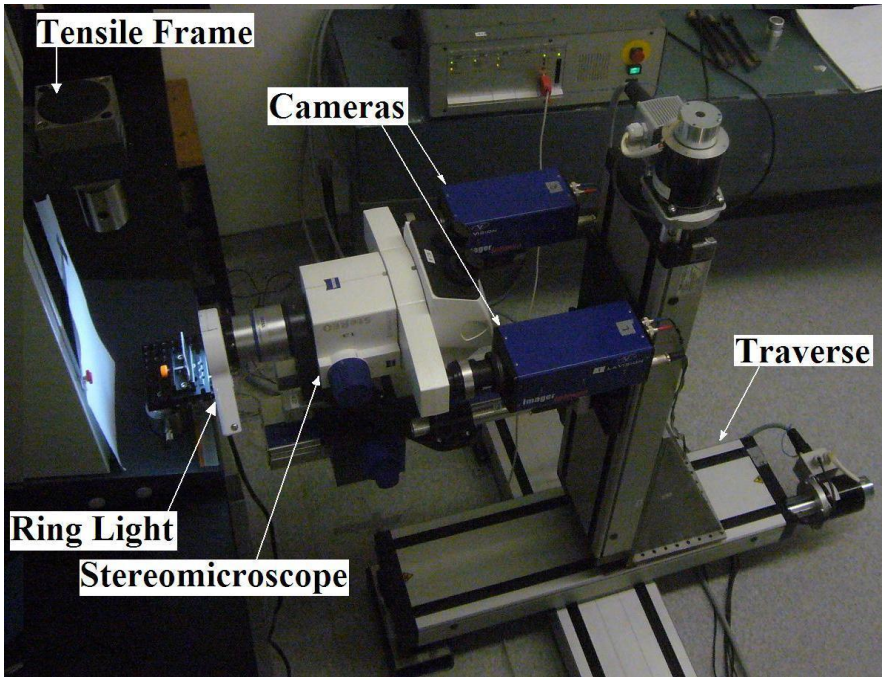

Figure 3.1 – The experimental setup used showing the two cameras fixed into the stereomicroscope which is mounted on a three axis traverse.

3.3.2 Stereo-DIC Processing

The captured images were processed using commercial software (DaVis 8.0.6, LaVision) to produce displacement vector fields and 3D surface reconstructions. Raw images were first preprocessed using a subtract sliding minimum filter with a 5 pixel filter size. The filter subtracts the average grayscale intensity from the entire image, removing background intensities and giving greater contrast to the speckle pattern. The residual shift between the two images in a stereo image pair is refined using six passes with decreasing subset sizes. The first three passes used 64x64 pixel subsets followed by three more passes using 32x32 pixel subsets. All passes had an overlap of 75%. A multi-pass correlation scheme with decreasing subset size was used to create the vector fields. A single correlation pass was performed with 256x256 pixel subsets to capture any large motions that may occur due to sample failure. This is followed by three correlation passes using 64x64 pixel subsets. Smoothing was performed using a 3x3 pixel smoothing filter. This filter removes noise by determining the output value of each pixel as a weighted average of pixels in the subset.

3.3.3 Sample Preparation

Composite braided tubes were manufactured using a braider (Steeger USA K80-72, Steeger USA, Inman, South Carolina). The composites were made from Dyneema fibers and a thermoset epoxy and can be seen in Figure 3.2. The thermoset epoxy consists of resin (EPON Resin 825, Resolution Performance Products, Pueblo, CO) and a hardener (Ancamine 1482, Air Products and Chemicals, Allentown, PA) at a 100:19 weight ratio. The coordinate system used has the x and y directions in the image plane and the z direction positive coming out of the page as shown in Figure 3.2

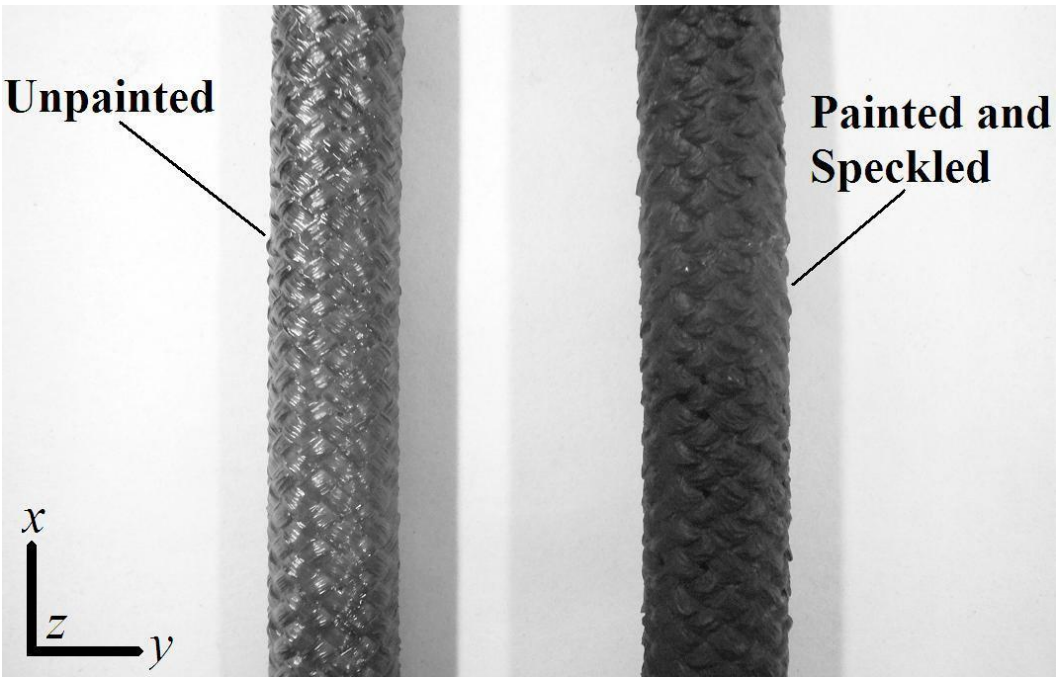

Figure 3.2 - Braided composite tubes before and after paint and speckling.

To ensure that the sample surface can be tracked, a speckle pattern must be applied to the surface to improve image contrast. Speckling should contain high information content (i.e high speckle density) to effectively track a surface pattern [19]. Fluorescent speckling was used, following Berfield [24], to reduce lighting effects such as reflections or shadows. The speckle patterns were applied using an airbrush (custom-B micron, Iwata-medea Inc, Portland OR), operated at a pressure of 450 kPa (~65 psi). As the airbrush is gravity fed, the fluorescent paint was thinned to improve flow. The paint and thinner used was ~1:2 mixture of fluorescent paint (Createx 5404, Createx Colors, East Granby CT) and reducer (Createx W100 Wicked, Createx Colors, East Granby CT).

An example of the resulting speckle pattern on a composite braid is shown in Figure 3.3. This method of speckling produced a high density of dots ranging in size with the smallest at 2x2 pixels and some larger speckles reaching up to 5x5 pixels. The speckles contrast strongly against the black background, providing the necessary pattern for DIC.

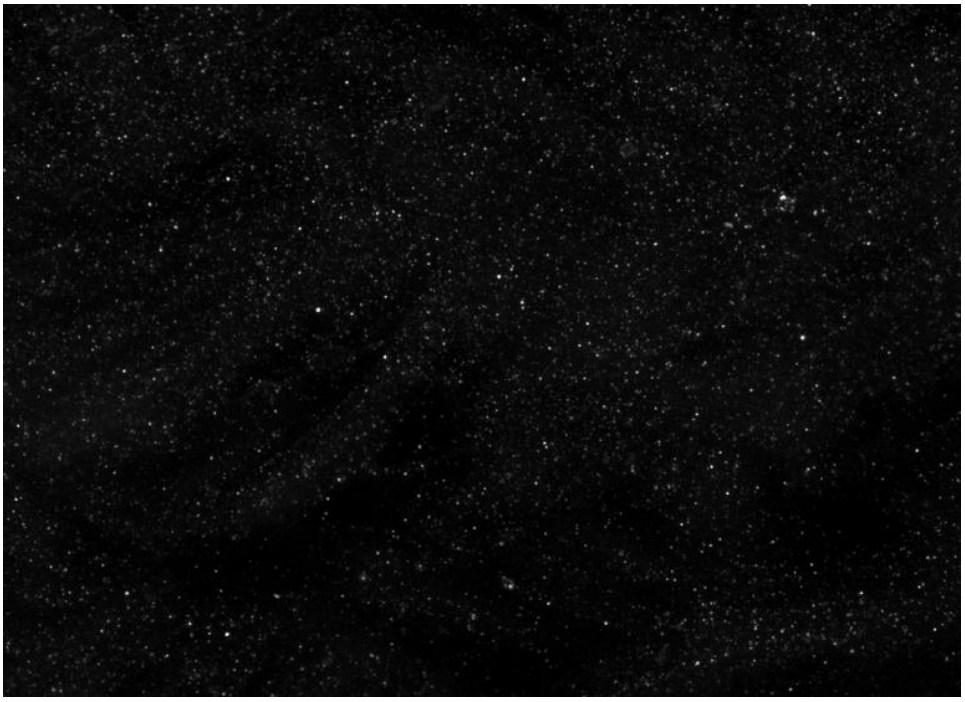

Figure 3.3 - A speckled composite flat braid image with a filter applied to increase the contrast.

3.3.4 Rigid Body Motion Experiment

A flat composite braid was painted black and speckled (Figure 3.3). The surface of the flat composite braid is highly uneven. The fluorescent speckling can be seen as white dots through the stereomicroscope under a black light. Images were taken of the braid at a neutral position. Rigid body motion, both in the image plane (*y* axis) and out of plane (*z* axis) were applied to the braid at set intervals of 25.4μm, using a micrometer driven stage with a resolution of 25.4±12.7 μm. An image was captured at each interval, for a total of 20 intervals. The images were compiled to create image data sets each consisting of 21 images. Using DIC, the vector field was calculated for each image set.

The accuracy of rigid body motion measurement was assessed through direct comparison of applied and measured motions. Plots presenting a slope of 1 and a correlation coefficient of 1 demonstrate strong agreement between applied and measured displacements [25].

3.3.5 Strain Measurement in Tension Experiment

To evaluate the DIC system strain measurement accuracy the DIC strain measurement was compared to another measurement device. Extensometers have been used with composites and have been shown to accurately measure strain [3].

Composite braided tubes were subjected to uniaxial tension using a tensile frame (Synergie 400, MTS Systems Corporation, Eden Prairie, MN) with a 500±0.25N load cell (SMT2, Interface, Scottsdale, AZ), while being imaged by the DIC system as shown in Figure 3.4. An axial extensometer (634.11F-2X, MTS Systems Corporation, Eden Prairie, MN), with a 25.4mm gauge length, was also used in each test to measure the strain. The extensometer voltage readings were extracted using an analog to digital converter (ADC-8-250, LaVision GmbH, Göttingen, Germany). The measured strains from both devices were compared directly. If the two measurements match perfectly the slope should equal 1. The error is the percentage difference between the slope of the plot and 1.

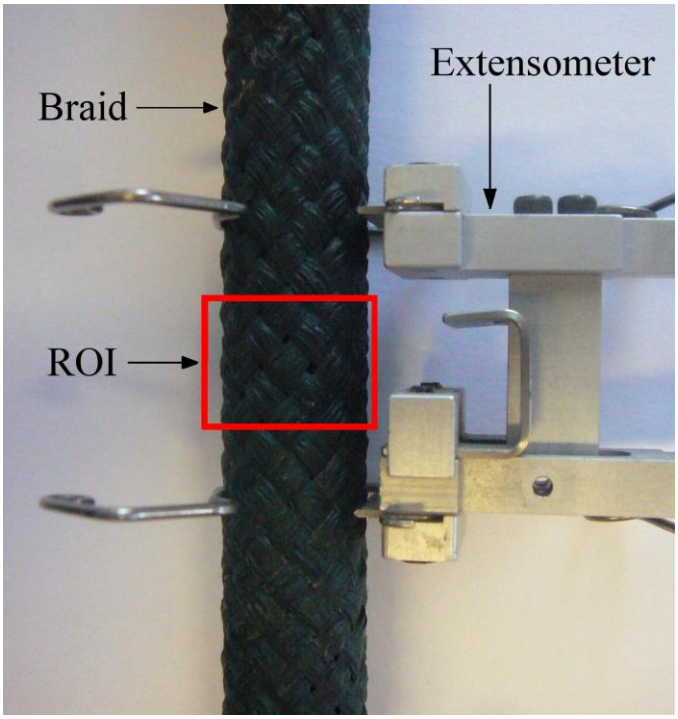

Figure 3.4 – A composite braided tube fitted with an extensometer. Within the red box is the region of interest (ROI) where the camera images were captured.

3.3.6 3D Surface Reconstruction Experiment

To determine the accuracy of surface reconstruction, radius measurements of a cylinder were made using a digital caliper (Mastercraft, Canadian Tire) and the DIC system were compared. Measurements were made on three Teflon calibration cylinders with smooth surfaces (Figure 3.5). The cylinders were painted black and speckled. The radii of the cylinders were measured ten times each along the length with the caliper which had a resolution of 10±5μm. The cylinders were then imaged with the stereomicroscope system shown in Figure 3.1. The surface was recreated and proper dimensions were applied through the calibration process. The coordinates for a string of points running laterally along the cylinder surface were selected. Points were fitted to a circle using equations (2) and (3), which minimize the sum of squared radial deviations and give a circle radius [26]. Equation (2) relates the coordinates of two points to coefficients. The equation is minimized to solve for the coefficients. Variables p_1 and p_2 are the coordinates for point 1 and 2 respectively, while a, b_1, b_2, and c are coefficients. The norm of b_1 and b_2 are given by $\|b\|$. Equation (3) relates the coefficients from (2) to the radius given by r.

$$(p_1 + \frac{b_1}{2a})^2 + (p_2 + \frac{b_2}{2a})^2 = \frac{\|b\|^2}{4a^2} - \frac{c}{a} \tag{2}$$

$$r = \sqrt{\frac{\|b^2\|}{4a^2} - \frac{c}{a}} \tag{3}$$

For the DIC measurements, each cylinder image was divided vertically into three zones: top, middle, and bottom. The radius in each zone was measured three times. A total of nine radius measurements were performed with DIC for each cylinder.

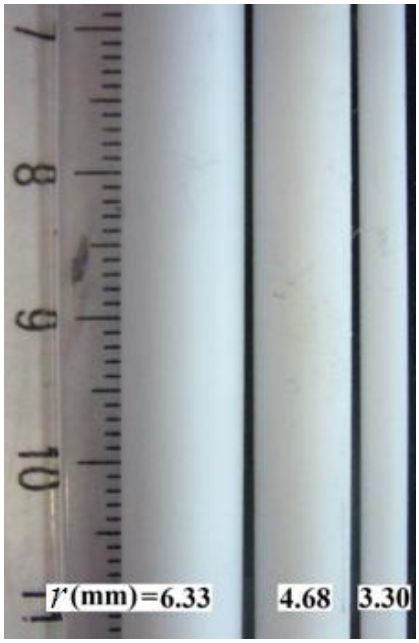

Figure 3.5 – The three Teflon cylinders with radii of 6.33mm, 4.68mm, and 3.30mm

All DIC radius measurements were made using custom post-processing software (Matlab, Math Works Inc, Natick, MA). The points taken from the generated surface create a curve. The edges of these curves are noisy because of the loss of focus in these regions of the images. From both ends of the curve 5% of the total points were cropped to remove any effects due to loss of focus. The circle center can be determined by finding the point with a common distance to all points along the curve. The distance from the center point to any point along the curve is the radius. With a center point and a radius a circle can be estimated as shown with the example data set in Figure 3.6.

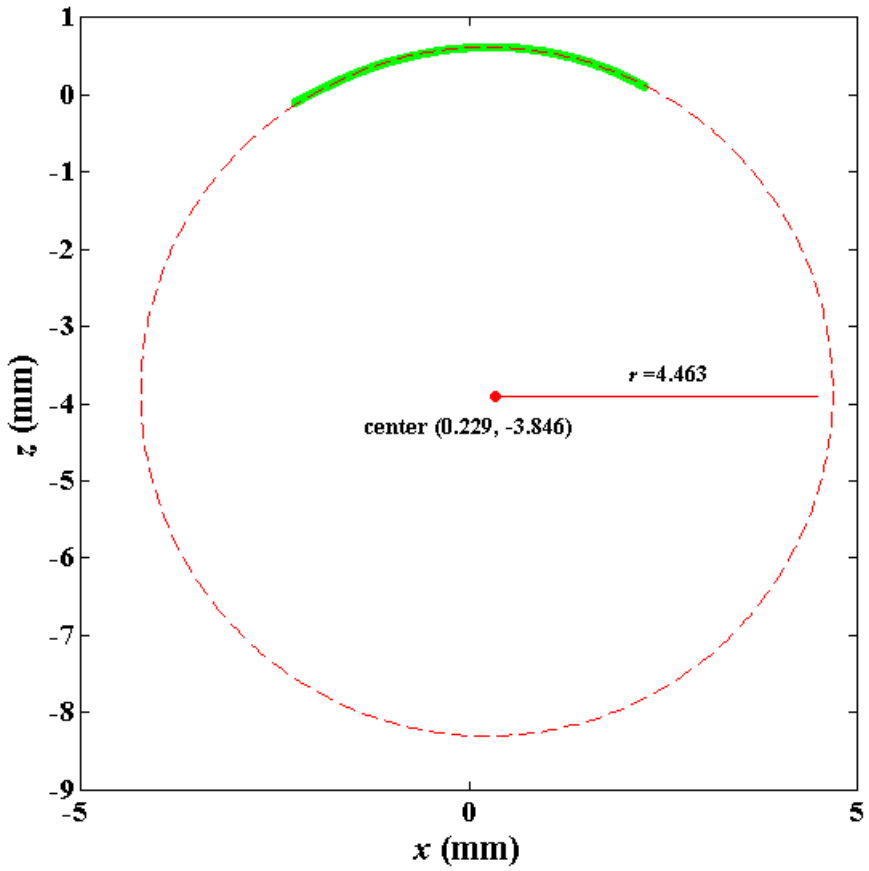

Figure 3.6 – A circle fitter generated image showing the estimated circle (dotted line) and surface map points (thick line).

3.4 Results and Discussion

3.4.1 Rigid Body Motion

Displacement matching results are depicted in Figure 3.7 for the in plane measurements and Figure 3.8 for the out of plane measurements. The DIC correlated displacements are directly compared to the physical displacement of the plate. The average difference and standard deviation between correlated and physical displacement for in and out of plane was found to be 1.38±0.54% and 2.14±0.71%, respectively. Correlated and physical displacements match poorly at the last point for out of plane motion. This could be due to the plate reaching the limits of the focal plane.

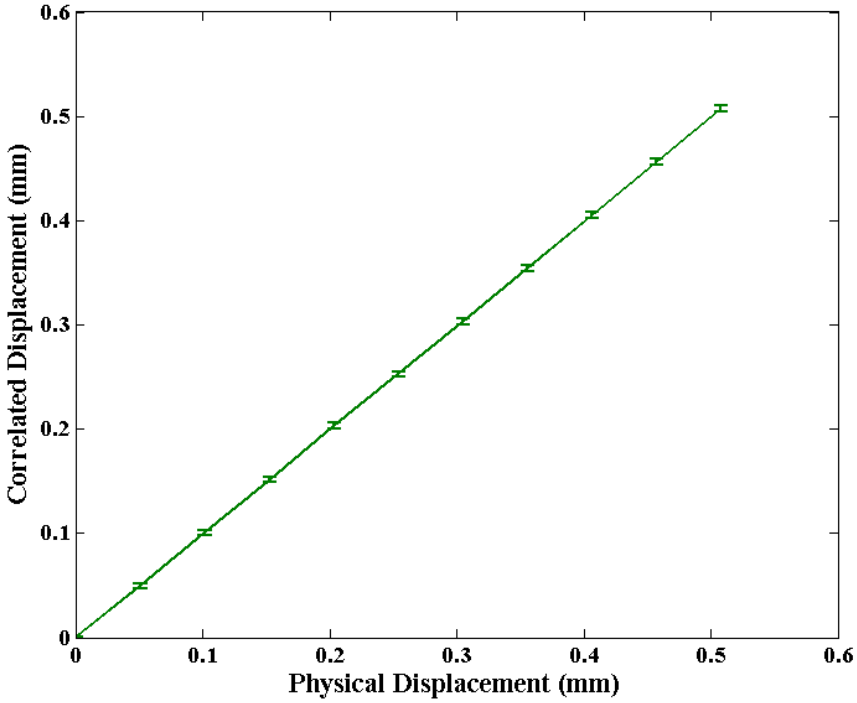

Figure 3.7 – In plane rigid body motion matching of correlated and physical displacements.

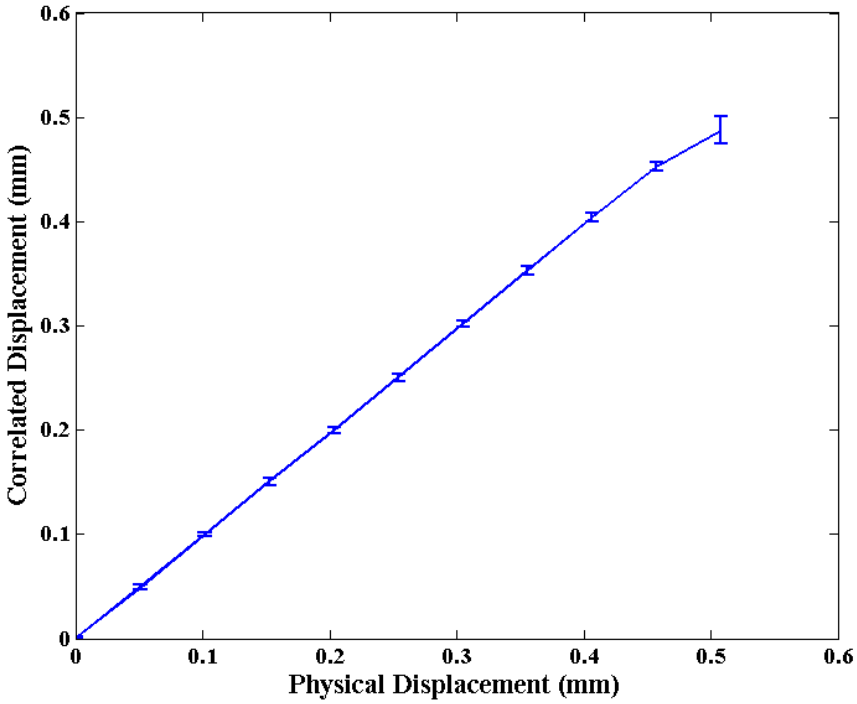

Figure 3.8- Out of plane rigid body motion matching of correlated and physical displacements.

Measurement residual at each interval of the rigid body motion test are displayed in Figure 3.9. The measurement residual is the difference between DIC correlated and physical displacement at each interval. The in plane residual ranges from -4.03 to 1.45µm, while the out of plane residual ranges from -4.61 to 7.70µm. It can be noted that while the residual for both are low, it is lower for in plane compared to out of plane.

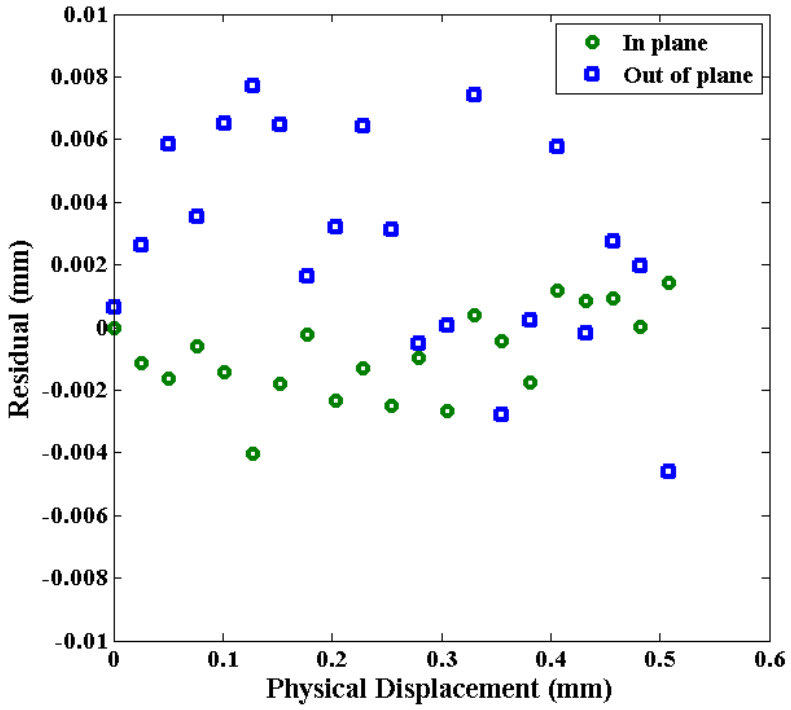

Figure 3.9 – Residual motion for in and out of plane rigid body motion relative to the physical displacement interval.

There are two reasons for the discrepancy between in and out of plane accuracy. A cause of error for out of plane measurements is the calibration procedure. Calibration for out of plane motion required manual motion of the calibration plate. The plate was shifted in the *z* direction using a micrometer driven stage, thus introducing human error to the applied *z* scale. Furthermore, the cameras are oriented at a shallow angle of 6˚ relative to each other, as determined through the calibration process. This angle is set by the optics of the stereo microscope. Wider relative camera angles increase the out of plane resolution,

whereas shallow angles improve in plane resolution [19]. The out of plane measurement error is expected to be roughly three times that of the in plane [22].

The results from rigid body motion testing provide a basis for validating DIC for use with braided composite tubes. Strain is derived from the correlated displacement vector field [18]. Thus, the accuracy of displacement measurements will directly affect strain measurements. Additionally, the use of a flat braid gives confidence that DIC is capable of creating accurate displacement vector fields for rough uneven surfaces.

3.4.2 Strain Measurement in Tension

The strain measurement comparison between the extensometer and DIC is shown in Figure 3.10. All test results directly compared the extensometer measured strain to the DIC correlated strain. The plot curve was fitted to a linear trend line giving the curve a slope of 1.0184. The correlated strain shows a strong match to the extensometer strain for braid sample 1. Plots for the remaining tests were of similar fit to that shown in Figure 3.8. The average difference between correlated and extensometer strain was found to be 1.6%.

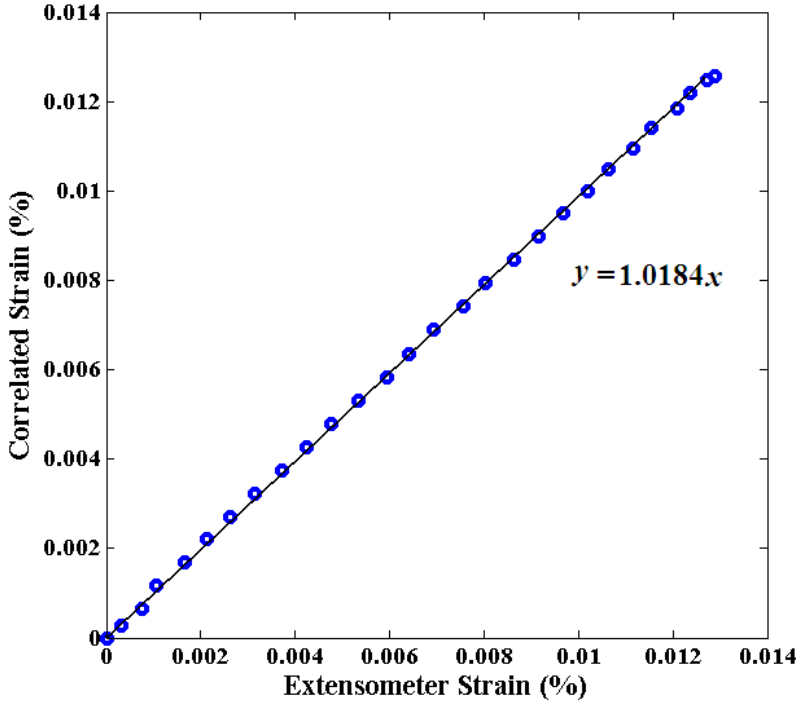

Figure 3.10 – A comparison of DIC correlated strain and extensometer strain of a Kevlar49/Epoxy composite tubular braid. A linear trendline (black) is fit to the data point shown as blue circles.

Accurate strain measurement is essential to characterizing the meso scale behaviour of braided composite tubes with DIC. Elastic constants can be found through strain using Hooke's law [27]. Numerical and finite element models describing braid behaviour can be experimentally validated with 3D DIC characterization [11]. It would also be possible to study unit cell behaviour and the interactions between fiber and matrix or between the fiber bundles themselves.

3.4.3 3D Surface Reconstruction

The cylinder radius measurements from surface reconstruction are shown in Table 3.1. The caliper measurement results reported radii of 3.30±0.02mm, 4.88±0.02mm, 6.49±0.01mm for cylinders 1, 2, and 3 respectively. The low standard deviation is expected as the samples have a constant radius and smooth surfaces. The DIC measurements for radius are most consistent for cylinder 3. For cylinder 1 the average

measured radius increases from top to bottom. This increasing measurement value is likely due to a slight misalignment of the cylinder relative to the vertical plane of the camera system. Misalignment relative to this plane means the top of the cylinder tilts towards or away from the camera. The string of points used to determine radius was taken laterally across the surface of the cylinder, and would show slightly different ellipses from top to bottom for a tilted cylinder. Another source of error is the calibration scale applied to these images. The surface reconstruction is largely dependent on the accuracy of the applied scales through the calibration procedure. An error in the applied scale for any of the three axes will result in an inaccurate surface, and thus an error in measurement. The largest difference between measurements is found at the bottom of cylinder 2, with a difference of -4.91%. The average difference and standard deviation, for surface reconstruction, is 2.45±1.54%.

Table 3.1 - The caliper and reconstructed surface measurements of smooth polymer cylinders and their percentage differences.

	Caliper Radius		**Reconstructed Radius**				
Cylinder	Average ± Standard Deviation (mm)	Location	1 (mm)	2 (mm)	3 (mm)	Average ± Standard Deviation (mm)	Difference (%)
1	3.30±0.02	Top	3.21	3.20	3.18	3.33±0.11	0.90%
		Mid	3.33	3.36	3.36		
		Bot	3.45	3.40	3.45		
2	4.87±0.02	Top	4.70	4.67	4.75	4.68±0.05	-3.99%
		Mid	4.68	4.69	4.71		
		Bot	4.57	4.61	4.70		
3	6.49±0.01	Top	6.36	6.37	6.35	6.33±0.04	-2.47%
		Mid	6.28	6.27	6.28		
		Bot	6.36	6.37	6.33		

When measuring the radius of cylindrical objects with smooth surfaces the difference between reconstructed surface measurements and calipers is minimal. However, when

sample surface roughness and features are introduced the measurements become different. Calipers contact the high points of surface features giving outer radius measurements based on the peaks of these features. DIC reconstructed surface measurements include all surface features and measure the average radius based on these features. Furthermore, the camera system resolution of 1.54μm is far greater than the 10μm resolution of a caliper. This level of detail enables the examination of sample surface topography using DIC reconstructed surfaces. Tracking the geometry of the braided tubes, subjected to a variety of conditions, can be achieved through DIC surface reconstruction. The stereomicroscope system enables tracking even on the meso scale. Caliper measurements cannot easily be made while a sample is subjected to loading.

3.5 Conclusions

A stereomicroscope camera system was assembled to perform 3D DIC on tubular braided composites. Three experiments were carried out to demonstrate the accuracy of the system both generally and for use on composite braids. Rigid body motion test results indicate that DIC with this camera system is able to accurately observe these motions both in and out of plane within 1.38±0.54% and 2.14±0.71% respectively. The matched strain profiles obtained from uniaxial tensile testing give confidence to the application of DIC to braided composite tubes. The strain test results show that DIC is able to accurately measure strain within 1.6%. The radius measurement test results suggest that the surface recreation capability of DIC is accurate within 2.45%. Larger errors were found in the *z* direction rigid body motion test and 3D surface reconstruction. This is because both tests were highly dependent on out of plane measurements. The accurate measurements from the three tests suggest that the fluorescent speckling method is applicable to composite braid surfaces. Furthermore, DIC can be used to examine surface features of samples subjected to loading conditions.

In future it may be beneficial to use a 3D calibration plate or to automate the motion of the calibration plate in the *z* direction. This would remove any human error associated with the current calibration procedure and further improve rigid body motion and surface recreation accuracy.

3.6 References

[1] J. Carey, M. Munro, and A. Fahim, "Longitudinal Elastic Modulus Prediction of a 2-D Braided Fiber Composite," *Journal of Reinforced Plastics and Composites*, 2011.

[2] M. Fouinneteau and A. K. Pickett, "Failure Characterisation of Heavy Tow Braided Composites Using Digital Image Correlation (DIC)," *Applied Mechanics and Materials*, vol. 5–6, pp. 399-406, 2006.

[3] K. Juss, J. Kotlarski, and P. Mertiny, "Detection of Matrix Cracking and Leakage in FRPC Tubes through Digital Image Analysis."

[4] E. Lang, "The effect of strain gage size on measurement errors in textile composite materials," *Composites Science and Technology*, vol. 58, no. 3–4, pp. 539-548, Apr. 1998.

[5] A. Harte, "Deformation and failure mechanisms of braided composite tubes in compression and torsion," *Acta Materialia*, vol. 48, no. 6, pp. 1259-1271, Apr. 2000.

[6] P. Ifju, "The use of moiré interferometry as an aid to standard test-method development for textile composite materials," *Composites Science and Technology*, vol. 53, no. 2, pp. 155-163, 1995.

[7] J. Lee, J. Molimard, A. Vautrin, and Y. Surrel, "Application of grating shearography and speckle shearography to mechanical analysis of composite material," *Composites Part A: Applied Science and Manufacturing*, vol. 35, no. 7–8, pp. 965-976, Jul. 2004.

[8] P. Potluri, R. J. Young, K. Rashed, A. Manan, and Y. T. Shyng, "Meso-scale strain mapping in UD woven composites," *Composites Part A: Applied Science and Manufacturing*, vol. 40, no. 12, pp. 1838-1845, Dec. 2009.

[9] T. C. Chu, W. F. Ranson, and M. A. Sutton, "Applications of digital-image-correlation techniques to experimental mechanics," *Experimental Mechanics*, vol. 25, no. 3, pp. 232-244, Sep. 1985.

[10] H. Haddadi and S. Belhabib, "Use of rigid-body motion for the investigation and estimation of the measurement errors related to digital image correlation

technique," *Optics and Lasers in Engineering*, vol. 46, no. 2, pp. 185-196, Feb. 2008.

[11] S. Lomov et al., "Full-field strain measurements for validation of meso-FE analysis of textile composites," *Composites Part A: Applied Science and Manufacturing*, vol. 39, no. 8, pp. 1218-1231, Aug. 2008.

[12] A. Willems, S. Lomov, I. Verpoest, and D. Vandepitte, "Optical strain fields in shear and tensile testing of textile reinforcements," *Composites Science and Technology*, vol. 68, no. 3–4, pp. 807-819, Mar. 2008.

[13] D. Ivanov, S. Ivanov, S. Lomov, and I. Verpoest, "Strain mapping analysis of textile composites," *Optics and Lasers in Engineering*, vol. 47, no. 3–4, pp. 360-370, Mar. 2009.

[14] C. Ayranci, D. Romanyk, and J. P. Carey, "Elastic Properties of Large-Open-Mesh 2D Braided Composites: Model Predictions and Initial Experimental Findings," *Polymer*, 2010.

[15] C. Ayranci and J. P. Carey, "Experimental Validation of a Regression-Based Predictive Model for Elastic Constants of Open Mesh Tubular Diamond-Braid Composites," *Polymer*, 2011.

[16] S. Giancane, F. W. Panella, R. Nobile, and V. Dattoma, "Fatigue damage evolution of fiber reinforced composites with digital image correlation analysis," *Procedia Engineering*, vol. 2, no. 1, pp. 1307-1315, Apr. 2010.

[17] F. Hild and S. Roux, "Digital Image Correlation: from Displacement Measurement to Identification of Elastic Properties - a Review," *Strain*, vol. 42, no. 2, pp. 69-80, May 2006.

[18] B. Pan, K. Qian, H. Xie, and A. Asundi, "Two-dimensional digital image correlation for in-plane displacement and strain measurement: a review," *Measurement Science and Technology*, vol. 20, no. 6, p. 062001, Jun. 2009.

[19] M. A. Sutton, J. J. Orteu, and H. W. Schreier, *Image Correlation for Shape, Motion and Deformation Measurements*, 1st ed. New York, NY: Springer Science and Business, 2009, p. 321.

[20] B. Pan, K. Qian, H. Xie, and A. Asundi, "Two-dimensional digital image correlation for in-plane displacement and strain measurement: a review," vol. 062001, 2009.

[21] LaVision GmbH, "DaVis 80 Product Manual - Imaging Tools." Gottingen, Germany, p. 114, 2011.

[22] N. J. Lawson and J. Wu, "Three-dimensional particle image velocimetry: experimental error analysis of a digital angular stereoscopic system," *Victoria*, vol. 1455, 1997.

[23] P. Synnergren, “Measurement of three-dimensional displacement fields and shape using electronic speckle photography,” *Library*, pp. 0-8, 1997.

[24] T. A. Berfield, J. K. Patel, R. G. Shimmin, P. V. Braun, J. Lambros, and N. R. Sottos, “Micro- and Nanoscale Deformation Measurement of Surface and Internal Planes via Digital Image Correlation,” *Experimental Mechanics*, vol. 47, no. 1, pp. 51-62, Jan. 2007.

[25] W. Navidi, *Statistics for Engineers and Scientists*, 1st ed. New York, NY: McGraw Hill, 2006, p. 869.

[26] G. H. Golub and R. Strebel, “Least-Squares Fitting of Circles and Ellipses,” *Update*, vol. 34, pp. 558-578, 1994.

[27] E. Popov and T. Balan, *Engineering Mechanics of Solids*, 2nd ed. Upper Saddle River, New Jersey: Prentice-Hall, Inc., 1998, p. 864.

Chapter 4: Tubular Composite Braid Radius Change Under Tensile Loading

4.1 Introduction

Braided composites are used in many industries and their use continues to grow [1] since they are capable of providing necessary strength and stiffness. The stiffness of a tubular composite braided structure is geometrically dependent on the radius and wall thickness, in addition to its elastic modulus [2]. Studies have looked at the relations between wall thickness, braid angle, and braid radius because of their importance in characterizing composite braids as structural components [3, 4]. Thus, knowing the tube's radius is valuable for stiffness critical applications and composite braid modeling. A new technique, digital image correlation (DIC), is now being used for textile-based composites to characterize elastic properties and geometries.

Studies that apply DIC to textile composites commonly focus on the onset and growth of damage. In some studies, DIC reconstructed surfaces were used as a visualization tool for damage progression of fiber composite pressure vessels [5, 6]. Others have used 3D DIC to reconstruct and measure surfaces of cylinders [7, 8], and a satellite dish [9]. These studies focused mainly on the ability to reconstruct an accurate surface using DIC. A further study, by Luo and Chen [10], measured the curved surface of a cylinder under axial loading. This expanded surface measurements to include deformation.

The length, radius and braid angle of a tubular braid preform are all dependent on one another [3, 11]. When a braid preform is loaded in the axial direction the braid lengthens in the axial direction, decreasing the radius and braid angle of the braid. In an epoxy matrix composite braid, similar behaviour is expected from the reinforcing fibers; however, the rigid matrix prevents large scale deformations to occur. If the braid radius experiences changes, the cross sectional area of the sample will also change, altering

stress calculations and affecting the accuracy of predictive models [12, 13]. Using the instantaneous cross sectional area to calculate stress and elastic properties may provide more accurate experimental data for modeling.

For this study 3D digital image correlation was used to measure surface deformation and reconstruct the surface of the composite braid samples. The technique measures surface deformation by comparing the relative gray scale intensities between a reference and deformed image [14]. The reference and deformed images are divided into square subsets forming a grid. Each subset contains variations in gray scale, which are used to match the subset between a reference and deformed image. A correlation algorithm is applied within each subset to find the location of peak correlation between the reference and deformed image. The vector from the center of the subset to the location of peak correlation is the average displacement vector for the subset. The reference and deformed image are cross correlated (CC) to give a vector displacement field. The progression from 2D vector fields to the calculation of 3D vector fields is outlined in Figure 4.1. Surfaces are reconstructed by first identifying similar points between stereo image pairs. A stereo cross correlation (SCC) process uses the identified points to find the corresponding points between the two images. Mapping functions, which were calculated during calibration, are then used to determine the *x*, *y*, and *z* coordinates of all points giving surface height. The mapping functions and the surface height are then used to combine the two vector displacement fields from camera 1 and 2 to create a 3D vector field [15].

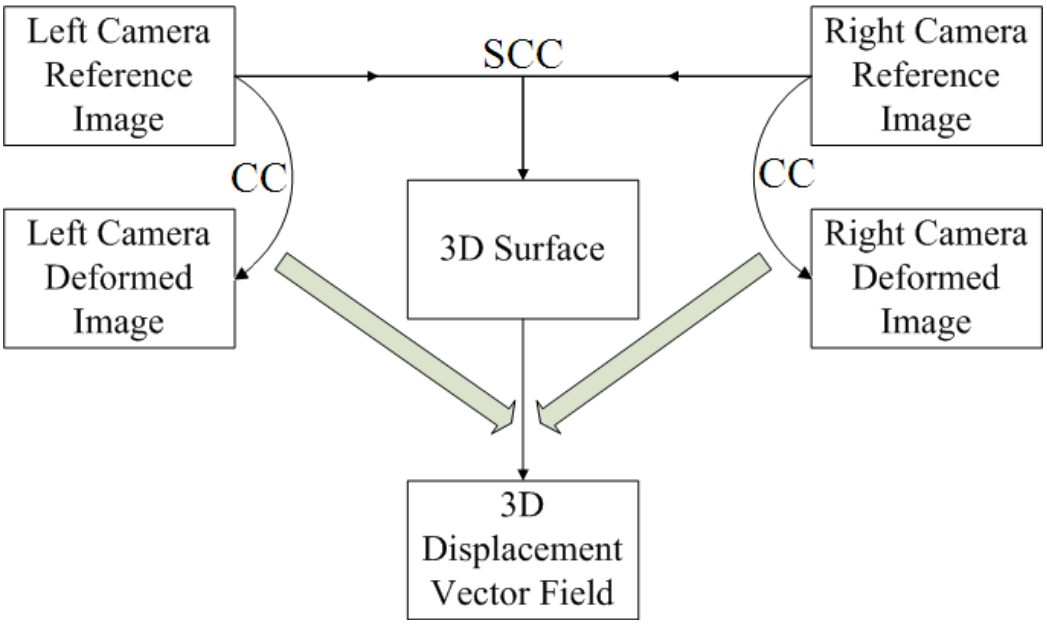

Figure 4.1 – A flowchart displaying the calculation of 2D vector fields using cross correlation (CC) and surface height using stereo cross correlation (SCC). 3D vector fields are calculated using 2D vector fields and surface height.

This study aims to investigate the change in outer surface nominal radius of tubular composite braids during progressively increasing tensile loading using surfaces reconstructed from 3D DIC. It further aims to provide insight on the impact of radius changes on experimental measurements and theoretical work.

4.2 Procedure and Methods

4.2.1 Experimental Setup

The testing equipment used for this study can be seen in Figure 4.2(a). The two charged-couple device (CCD) cameras (LaVision Imager Intense, LaVision GmbH, Gottingen, Germany) used for capturing images were attached to a stereomicroscope (Zeiss Stereo Discovery V8, Carl Zeiss MicroImaging Gmb, Gottingen, Germany). The stereomicroscope was mounted onto a rail extending from the three axis translation stage (LES 5, isel Germany AG, Eichenzell, Germany). The translation stage allowed the camera views to move between multiple regions of interest during a test with a resolution of 1µm. A tensile frame (MTS, Eden Prairie, MN USA) was used to load the tubular

braids axially. Load data was obtained from the tensile frame's ±1000lb load cell (661.12B, MTS, Minneapolis, MN, USA), which has an error of 1.5%. Controlling the translation stages and triggering the cameras to capture an image was performed from the control PC (see Figure 4.2(b)).

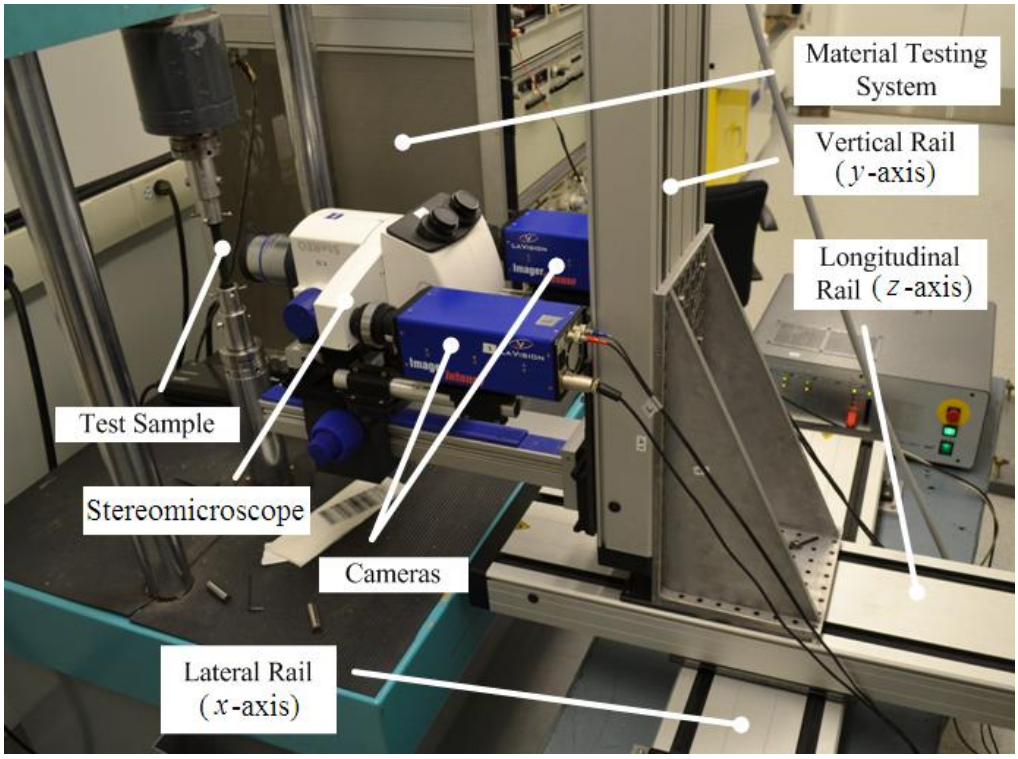

(a)

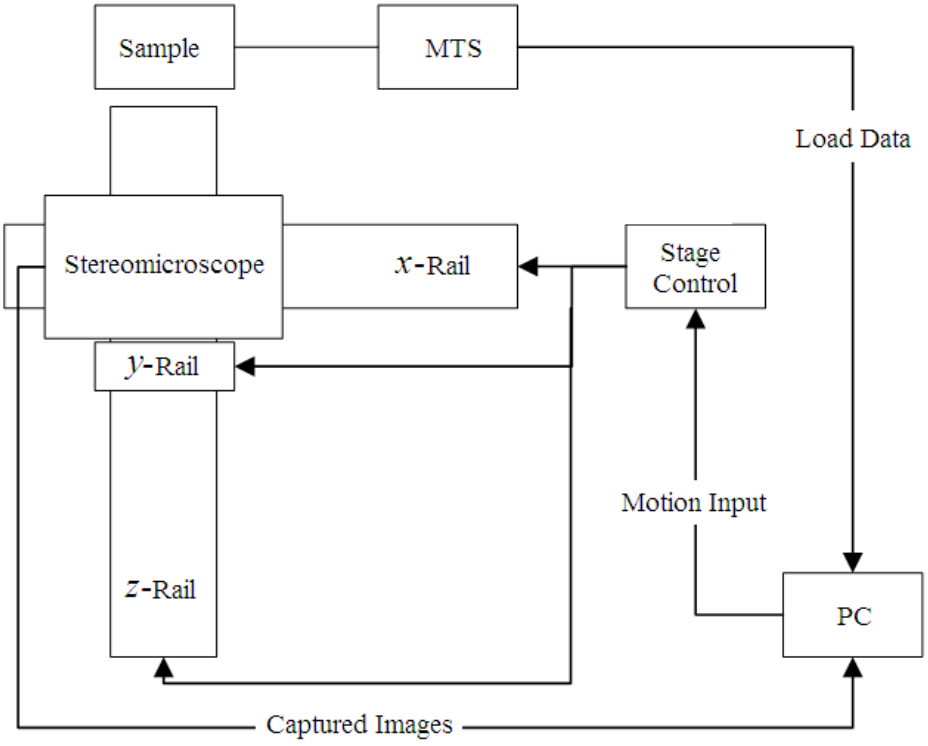

(b)

Figure 4.2 – A (a) photo and (b) schematic of the experimental setup.

4.2.2 Sample Preparation

Tubular diamond braided composites were used in this study as was done in Ayranci and Carey [12]. The braided sock preforms were produced using a braider (Steeger USA K80-72, Steeger USA, Inman, South Carolina) configured to produce diamond braid patterns. Kevlar fibers (Kevlar 49, 5680 Denier, Dupont, Mississauga, Ontario, Canada) were used as the reinforcement material. A diamond braid preform architecture and a post cure composite braid are shown in Figure 4.3. The coordinate system convention is also given in this figure with the *x*-axis positive to the right, *y*-axis positive upwards, and the *z*-axis positive coming out of the page. The preform was placed over a smooth Teflon mandrel with an outer diameter of 11.39±0.03mm. Fibers were manually impregnated with a thermoset epoxy consisting of an EPON Resin 825 (Resolution Performance Products, Pueblo, CO) and an Ancamine 1482 hardener (Air Products and Chemicals, Allentown, PA) mixed at a 100:19 weight ratio. The braids were placed upright in an oven to ensure an even coating and allowed to cure for 2 hours at 110˚C, as done previously [12]. The cured braids were cut to length and bonded to end tabs using the same epoxy resin and curing process as the braid matrices.

Figure 4.3 – A braided preform and cured braid with the coordinate system convention.

A total of 31 braided samples were manufactured with the following average ± standard deviation geometric characteristics: braid angles of 42.48±1.96˚, gauge lengths of 90.82±1.54mm, wall thicknesses of 1.02±0.05mm, and outer radii of 6.65±0.06mm. Gauge length and wall thickness measurements were made using a digital caliper (0-150mm ±10µm, Mastercraft, Canadian Tire). Outer radius measurements were made three times on each braid sample using a micrometer (Outside Micrometer 0-25mm ±5µm, Mitutoyo, Mississauga, Ontario, Canada). The measurements of all samples were averaged together.

A randomized speckle pattern was applied to the surface of the braids to perform DIC based measurements as detailed in Leung et al [8]. Braids were first painted with a flat black spray paint (Indoor/Outdoor, Krylon Products Group, Cleveland, OH) to reduce light reflections, and give a cleaner speckling surface. A fluorescent paint (Createx 5404, Createx Colors, East Granby, CT) and reducer (Createx W100 Wicked, Createx Colors,

East Granby CT) was used at a 2:1 ratio. The fluorescent speckle pattern was applied using the mixed paint and an airbrush (custom-B micron, Iwata-medea Inc, Portland OR), similarly to a DIC study by Berfield [16]. To excite the fluorescent particles, a 2.64" ring light (Edmund Optics, Barrington, NJ, USA) with a 365nm black-light (Edmund Optics, Barrington, NJ, USA) was used. The resulting speckling patterns without and with a flat black paint background are found in Figures 4.4(a) and 4.4(b) respectively. Figures 4.4(c) and 4.4(d) are the resulting speckle patterns after a subtract sliding minimum filter is applied to the images. The speckle pattern without the black background has formed lines with the fluorescent particles, decreasing the speckling density. When the black background is applied, the fluorescent particles do not form solid lines and the particle density is more consistent throughout the image; this is the desired pattern for DIC.

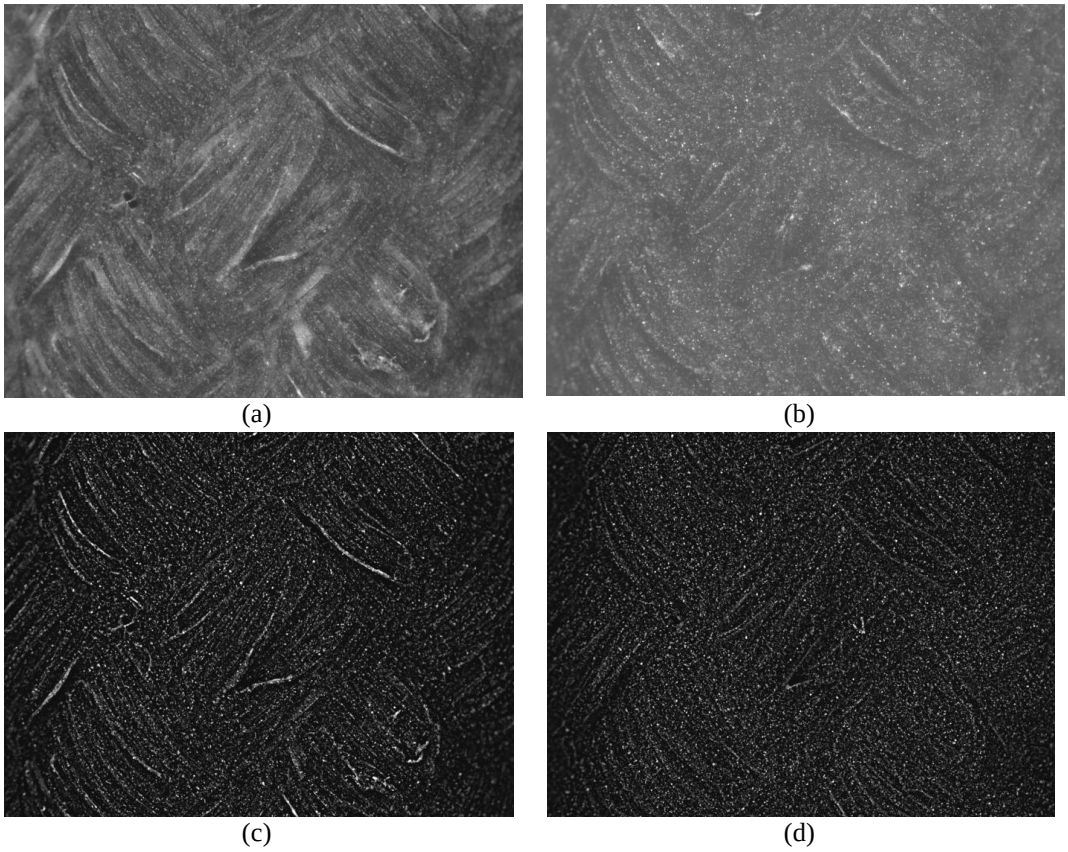

Figure 4.4 – (a) Speckled braid without black paint background; (b) speckled braid with black paint background; (c) speckle pattern after filtering without black paint background; and, (d) speckle pattern after filtering with black paint background.

4.2.3 Calibration Procedure

Calibration of the camera system is of great importance when using a multiple cameras for surface measurements [17]. Errors in 3D surface reconstruction can stem from calibration and system setup [18]. The intrinsic and extrinsic camera parameters are determined through the calibration process [19]. Lens defect and displacement distortions are corrected through the intrinsic parameters. Relative camera positions and orientations are described through the extrinsic parameters. The calibration process also applies a scale to the images. For this study, a 2D calibration plate was used for a 3D calibration. The in-plane scales (x and y) were defined from the 0.5mm dot spacing of the calibration plate. The out-of plane scale (z) was defined with moving the calibration plate in the out of plane direction by known amounts, using a micrometer driven stage. This calibration procedure was validated in a previous study using the same camera system [8].

4.2.4 Post Processing and Surface Reconstruction

A total of 60 stereo image pairs were captured for each sample with 20 stereo image pairs in each image set of the three regions of interest. Starting with a unit cell located at the mid span of the sample, every other unit cell along the axial direction was chosen. The areas containing the unit cells are defined as region 1, 2 and 3 as shown in Figure 4.5. The center of each of these regions of interest is spaced approximately 9mm apart from one another on the sample tubular braids.

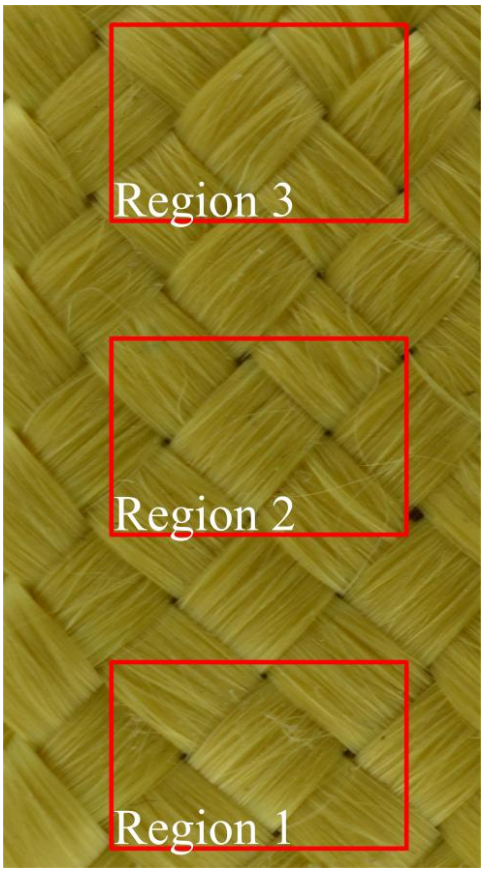

Figure 4.5 - Location of imaged unit cells relative to one another on a single sample.

Post processing of the image sets was performed using a commercial software (DaVis version 8.0.6 StrainMaster 3D, LaVision GmbH, Gottingen, Germany). The subtract-sliding-minimum filter was applied to all images to increase the contrast in the images. Captured images without (Figure 4.4(a) and (b)) as well as with (Figure 4.4(c) and (d)) the application of the filter are shown. The stereomicroscope has a shallow focal depth; as a result, the left and right side of the images were out of focus. These were masked out prior to creating the surfaces. A reconstructed composite braid surface is shown in Figure 4.6. The reconstructed surface has a resolution of 1390x1060 pixels. With the stereomicroscope magnification, details of fiber bundles within each strand can be clearly discerned.

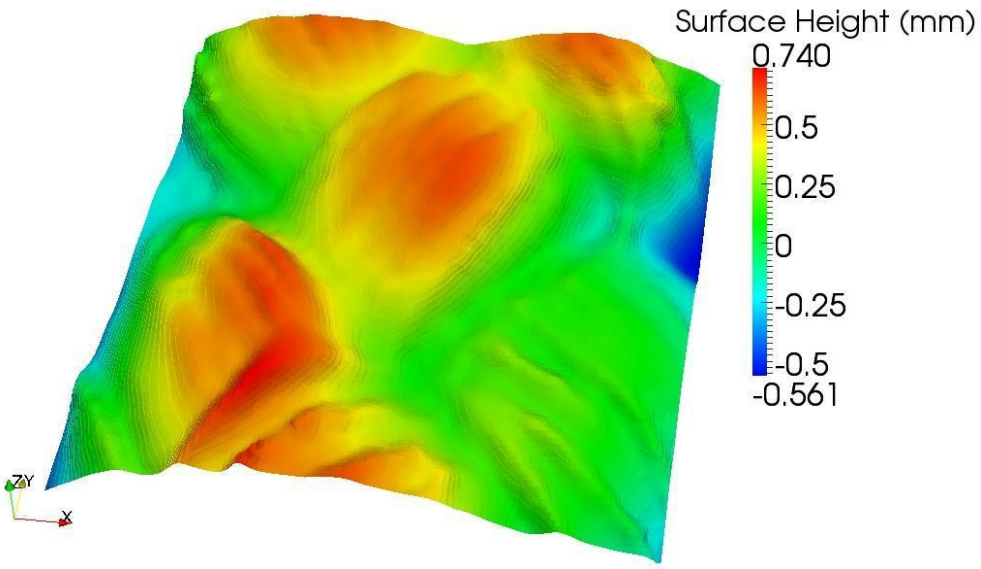

Figure 4.6 – A surface reconstruction from a stereo image pair. The zero in the scale represents the mid span of the focal depth.

Displacement vector fields that describe the surface motion of the composite braids during testing, as shown in Figure 4.7, were calculated using multiple passes. A 256x256 pixel size subset was used for the first pass, followed by three passes with a smaller 64x64 pixel subset. All passes used a 75% overlap. The larger subset of the first pass is meant to capture the largest motions observed during the test. The largest motions would occur in the frames that captured sample failure. The smaller subset passes would capture the smaller motions observed between most frames and would also give a much denser field of displacement vectors.

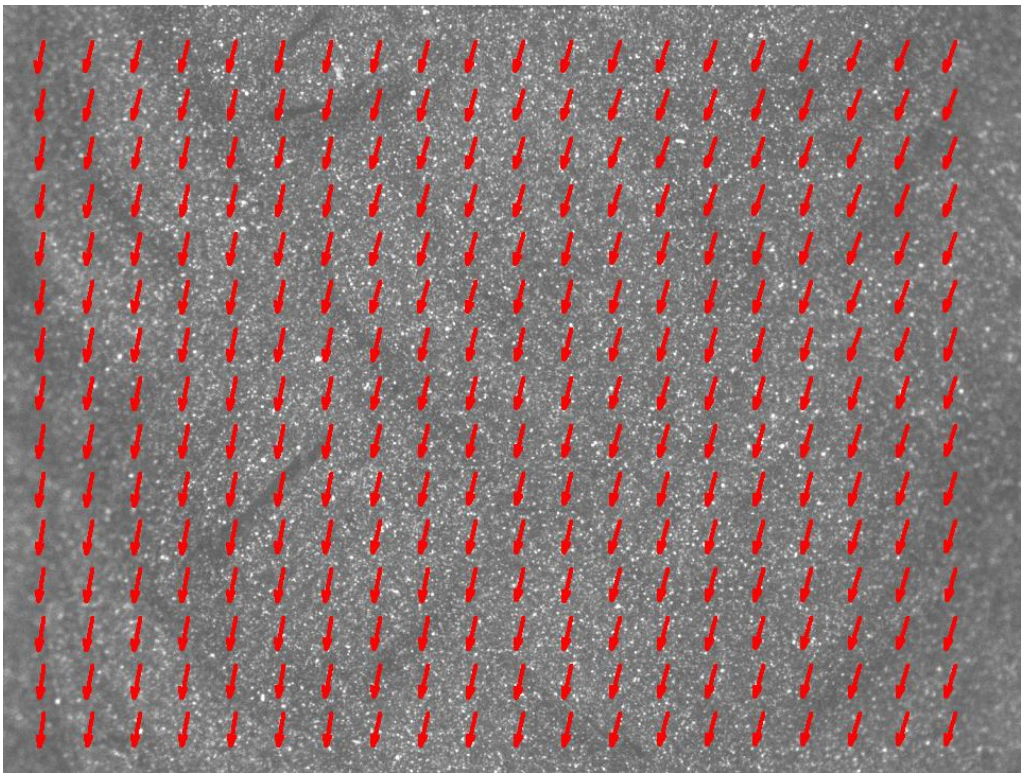

Figure 4.7- The displacement vector field of a composite braid under loading. The vector density has been reduced for clarity.

Strain of the test samples was measured using the DIC calculated displacement fields. The area of the displacement field used to calculate the strain can be seen in Figure 4.8. The neighboring displacement vectors within the selected area are compared to one another. The difference is a displacement gradient, which is the strain.

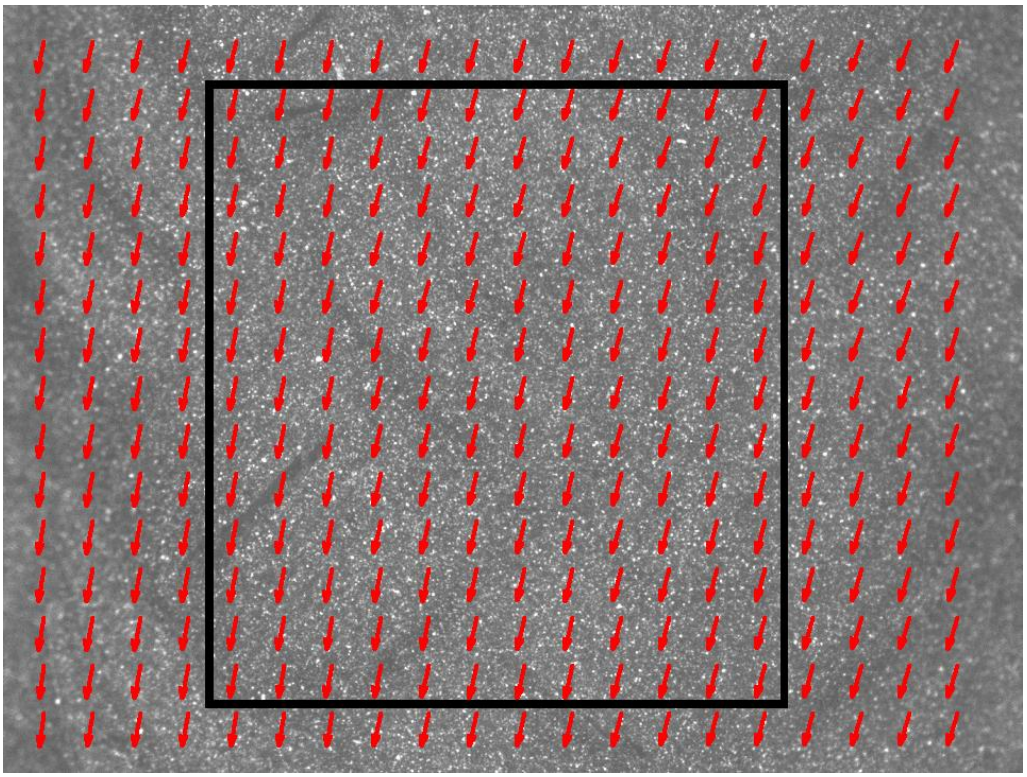

Figure 4.8 – The area of the displacement vector field from which strain is calculated.

4.2.5 Radius Measurements by Circle Fitting

Braid radii were measured from the reconstructed surfaces. An unpainted braid can be seen in Figure 4.9. The selected point can be seen in on the central unit cell. A lateral cross section is taken from this point and is depicted by a white line. The selected point is tracked throughout all subsequent images to ensure that the same cross section is measured. Out of focus regions at the left and right edges of the image can also be seen.

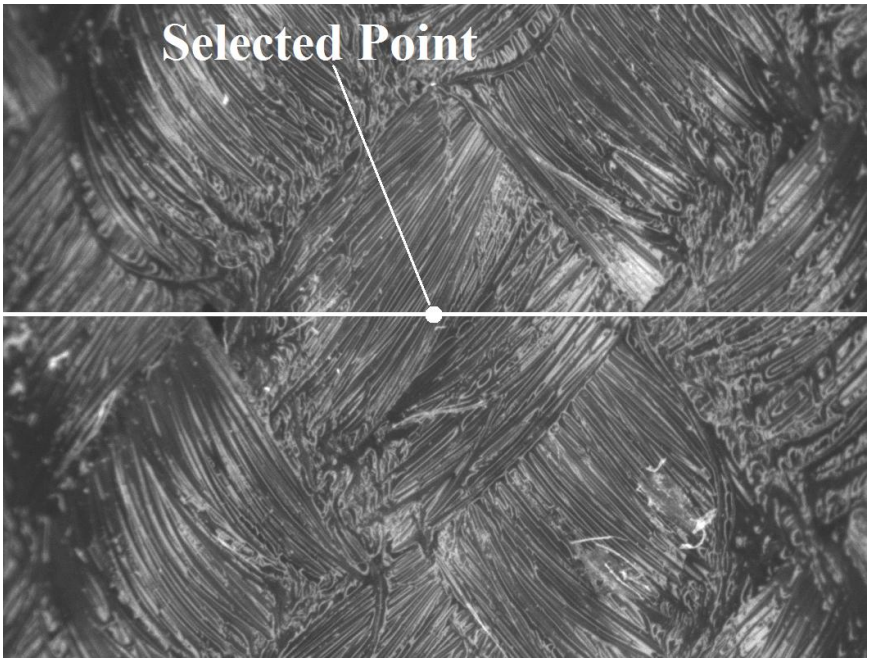

Figure 4.9 – An unpainted braid image with the selected point and cross section line in white.

The data at both ends of the cross section was trimmed to remove any surface that was reconstructed from out of focus regions in the captured images. The locations of the lateral limits are represented by the vertical lines in Figure 4.10.

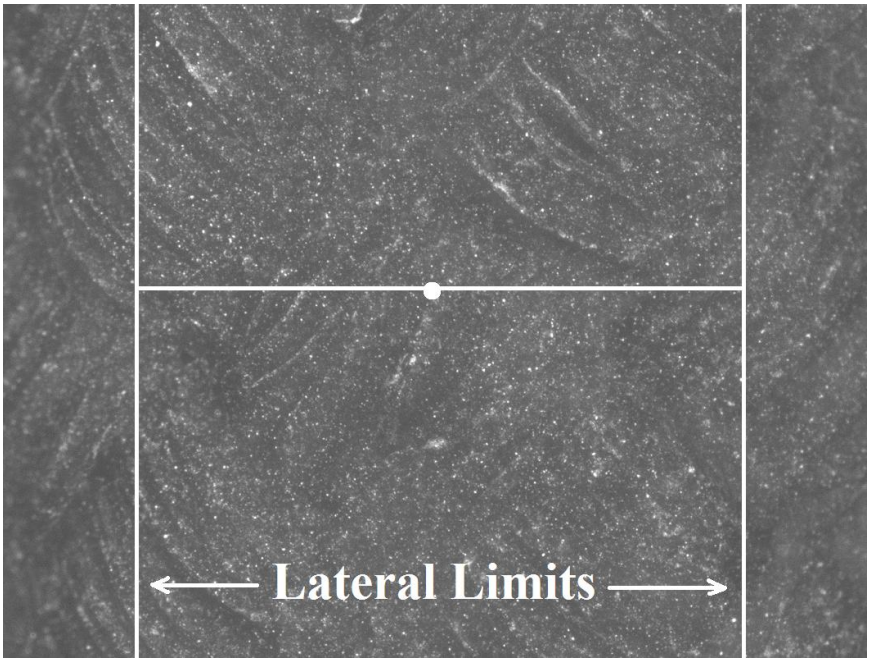

Figure 4.10 – A speckled braid image with out of focus edges (outside the lateral limits) removed from cross section line.

The cross section taken from the surface height map can be seen in Figure 4.11. The remaining cross section consists of a string of points that are approximated to fit a circle.

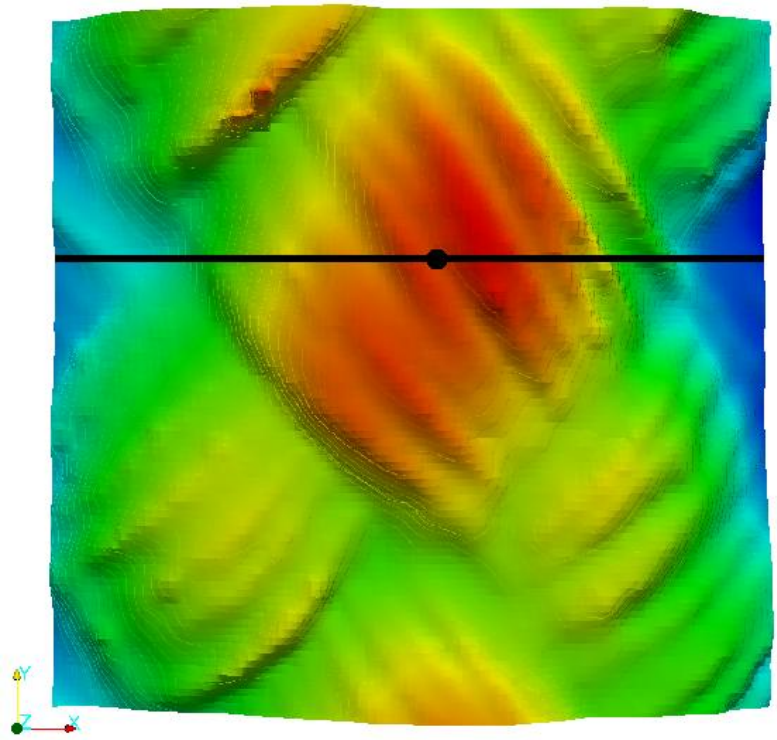

Figure 4.11 – A 3D surface reconstruction with the selected surface perimeter.

The estimated circle is created by minimizing the sum of squared radial deviations from all points on the cross section using equations 1 and 2 [20]. The coefficients *a, b_1*, *b_2*, and *c* are solved for using the coordinates from point 1 and 2, as represented by p_1 and p_2. $\|b\|$ is the norm of b_1 and b_2**.** The radius of the estimated circle, represented by *r*, can then be found using the coefficients from equation 1.

$$(p_1 + \frac{b_1}{2a})^2 + (p_2 + \frac{b_2}{2a})^2 = \frac{\|b\|^2}{4a^2} - \frac{c}{a} \quad (1)$$

$$r = \sqrt{\frac{\|b^2\|}{4a^2} - \frac{c}{a}} \quad (2)$$

An example of a circle fit plot is shown in Figure 4.12. The cross section is shown in green, while the dashed red line is the estimated circle fit to the cross section.

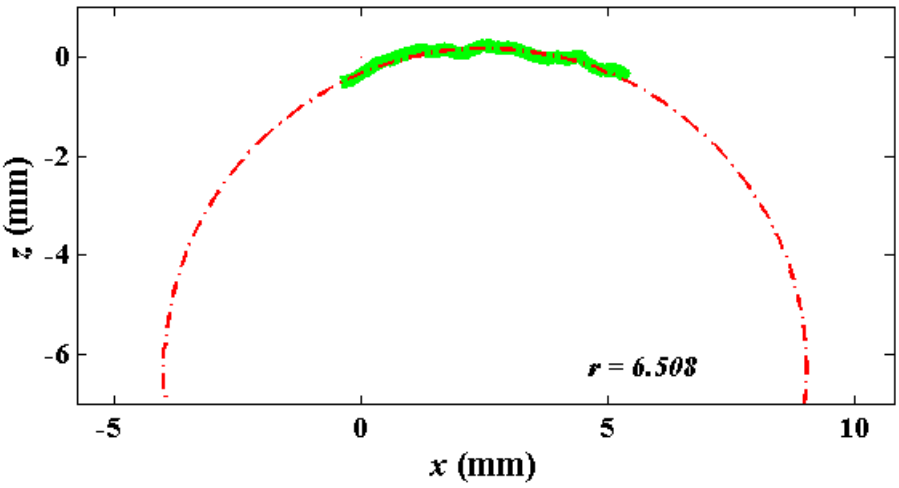

Figure 4.12 – A circle fit plot with the estimated circle (red dashed line) fit to the reconstructed surface perimeter (green).

During testing, the braid continues to shift in the captured images as the sample is pulled in the axial direction. The measurement point selected in the first frame must be tracked through subsequent frames to ensure that the same location of the braid is measured. The DIC displacement vector fields calculated from the image sets were used for this. The displacement vectors are equally spaced in a grid that corresponds with the captured images. Displacement vectors from the grid subsets directly neighboring the measurement point, a 3x3 matrix of vectors, were averaged (Figure 4.13). The average of the displacement vectors was added to the first frame measurement point and is used in the next frame. This allows for the braid motion to be tracked and the measurement location to remain in at the same location on the braid. The lateral limits are also shifted with the measurement point.

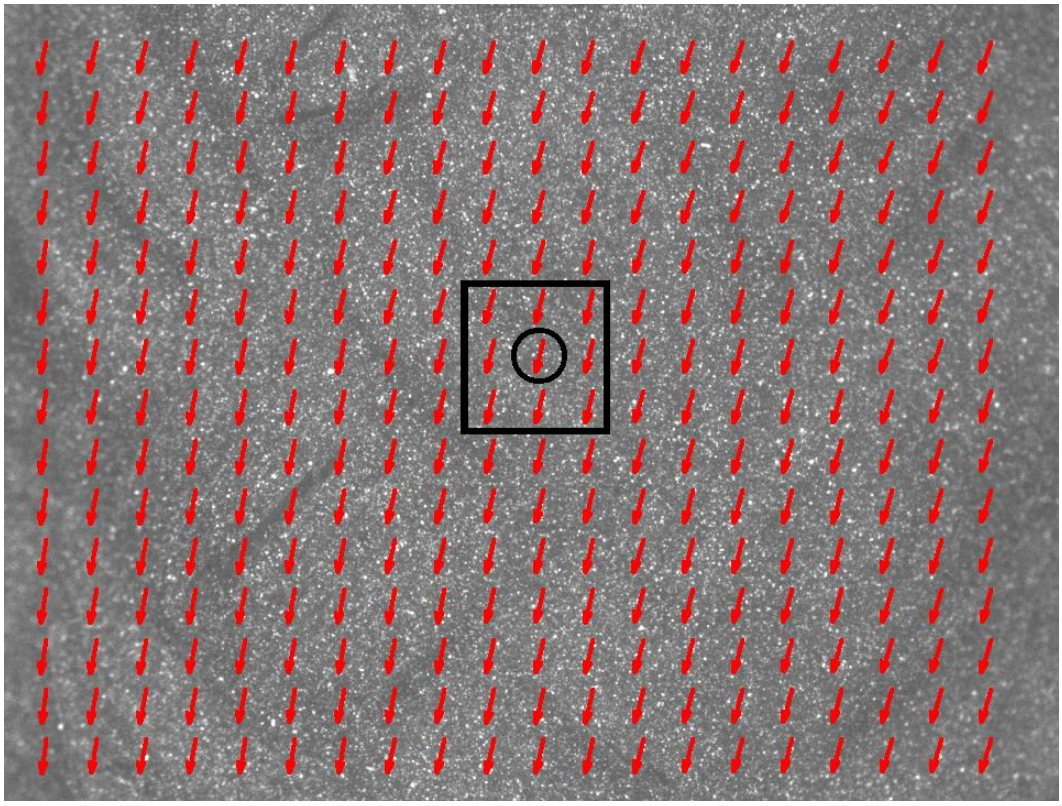

Figure 4.13 – A displacement vector field with the selected point vector (in circle) and the averaged displacement vectors used for tracking (in square)

The radii were measured with two different methods, an area method and a band method. The area method radius measurements are an average of 60 cross section measurements, with equal spacing of 10 data rows between each measurement, over the unit cell. The line at the selected point is the reference cross section. Thirty measurements are made on and above the reference cross section, with the remaining thirty made below. The band method averaged radii measurements over five consecutive cross sections. The line at the selected point is the central cross section. Cross sections are also measured on two lines directly above and two below the central cross section. The average of these five cross sections is the average radii for that frame. The measurement locations for the area and band method are illustrated in Figures 4.14(a) and (b).

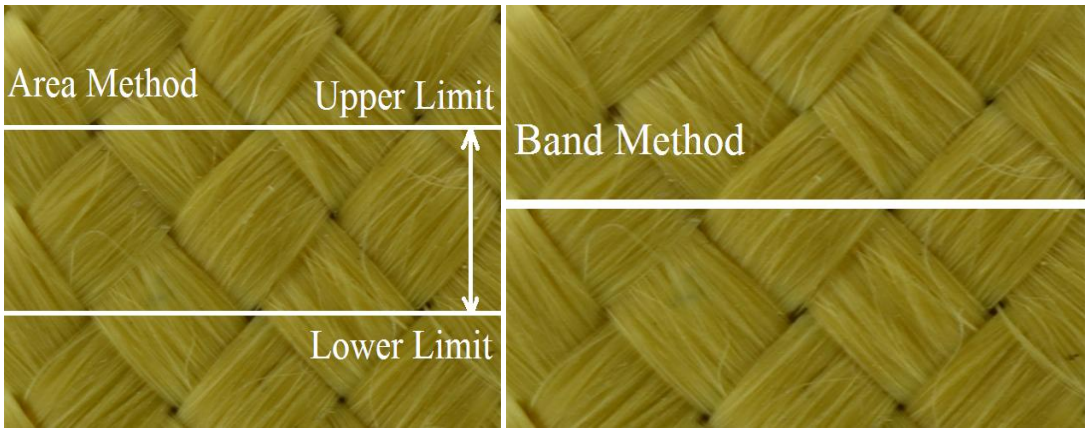

(a) (b)

Figure 4.14 – The radius measurement locations when using the (a) area and (b) band method.

The circumference of the braid contains ten unit cells. However, only a single unit cell fits comfortably within the field of view of the camera system. The cross sections can range from containing a single unit cell peak in the middle to having two peaks at the edges of the cross section. Radius measurements using the band method were made at three different locations in the unit cell, as defined in Figure 4.15, to examine how the local surface roughness and limited braid surface can affect radius measurement. The valley is centered where the edge of four strands touch. The peak is centered in the middle of the crossover region where one strand crosses directly over another. The middle is equidistance from both the valley and peak.

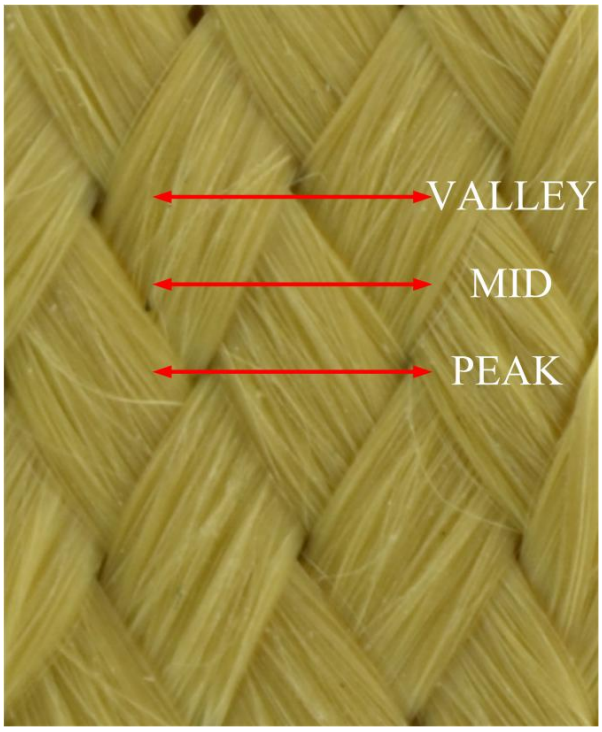

Figure 4.15 – A mapping of the three locations within a unit cell where band method measurements were taken.

4.2.6 Camera Traverse Stability Test

To determine consistency across the braid, image sets were captured over three unit cells on each sample. These unit cells are contained in the three regions. Region 1 is the unit cell located at the mid span of sample gauge length. Imaging started from region 1 and progressed through to regions 2 and 3. As a result of the downward stroke of the testing machine, complete image sets show the unit cell moving downward through the field of view. To maintain the unit cells in the field of view, the unit cells were centered at the top of the initial image frame.

The cameras are traversed between the three regions multiple times during a test. If the traverse does not return the cameras to the same location each time a stereo image pair is captured, the resulting images will include both test sample and camera motion. Repeatability of the system to precisely return to each of the three positions was assessed. A composite braid sample was used for this test. The cameras were focused on region 1

and an image pair was captured. The cameras were then traversed approximately 9mm to region 2, and back down to region 1, where another image pair was captured. This was repeated until an image set containing a total of twenty image pairs were captured in region 1. The image set was processed to produce displacement vector fields, which describe the displacement of the imaged surface. The processing and displacement vector field details were described previously.

4.2.7 Preliminary Radius Measurement under Tensile loading Test

A preliminary tensile test was performed on a polyvinylchloride (PVC) tube sample with a gauge length of 99.31mm and outer radius of 4.90±0.12mm. Outer radius is an average of five measurements made along the length of the PVC tube using a micrometer. This test was performed to ensure that the radius of a tubular object subjected to loading can be measured. The speckle pattern was applied to the surface of the sample as described previously. The sample was fixed into the tensile frame and pulled for a total stroke of 12mm. Two frames of the test were captured before loading was applied. A total of 20 stereo image pairs were captured over the duration of the test. Strain measurements were made using DIC displacement vector fields. Radius measurements for this test were obtained both using the micrometer and the DIC area method. The micrometer radius measurement was averaged over ten measurements.

4.2.8 Braid Radius Measurement Under Tensile Load Test

A braid sample was secured in the grips of the tensile frame. The cameras were centered and focused in region 1, where the coordinates of the translation stage are recorded. The cameras were then traversed upwards to unit cells in region 2 and 3 to ensure that the cameras are properly centered and focused in these regions. Before the first test was run, the sample was removed from the tensile frame to perform the camera calibration procedure at each of the three regions. The calibration could be applied to all other tests

as long as the cameras captured images at the same locations for all tests. The sample was then reinserted into the tensile frame. The image capturing procedure begins with a stereo image pair captured in region 1, before traversing the cameras to region 2 and 3. Scanning through the three regions once captures one stereo image pair of each region for a total of six images per scan. Two scans are completed without applied loading to ensure that the initial unloaded state of the sample is captured. After two scans, the tensile frame loading is started and the sample begins to strain. The axial loading was stroke controlled with a pull rate of 7.6μm/s for a total stroke of 2.86mm. The stroke is continuous throughout the test. During loading, the cameras scan over the three regions a total of twenty (20) times, creating complete image sets of 20 stereo image pairs for each region. A total of sixty (60) stereo image pairs are captured for each test sample. The image capturing and tensile frame loading is then stopped, the current test sample is removed and the next test begins. The relation between stroke reached at each image set frame is provided in Figure 4.16. At maximum stroke the samples are expected to reach a strain of 2.9%. This level of strain is beyond the expected failure point, which is approximately 1.5% strain for similar braid angles [21]. The total stroke was chosen to allow for braid radius change to be evaluated through to failure. When the matrix has cracked and can no longer maintain a rigid tubular shape, the braid is considered to have failed.

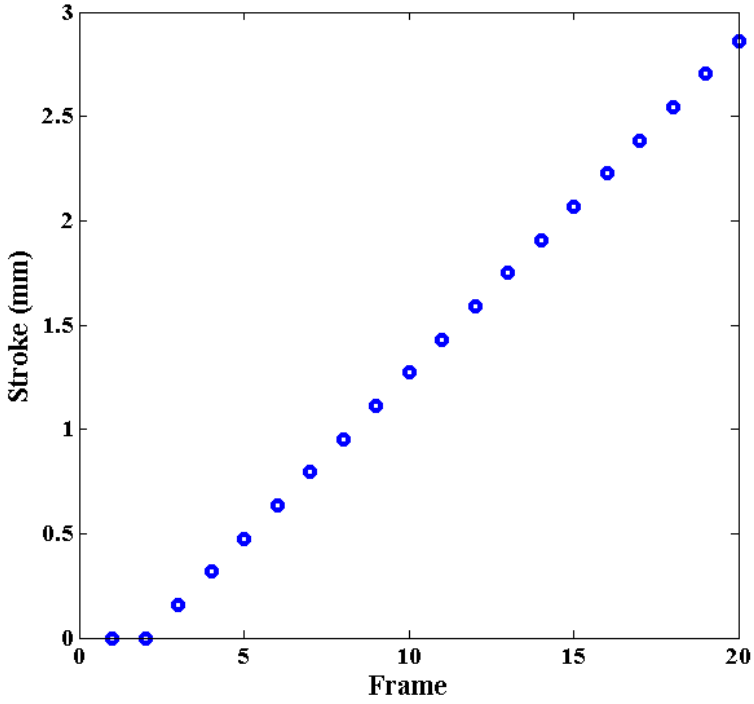

Figure 4.16 –Tensile frame stroke as a function of the frame captured by the stereomicroscope. Loading was started after capturing the second frame.

4.3 Results and Discussion

4.3.1 Camera Traverse Stability Test Results

The displacement vector fields are averaged to give the overall displacement in the *x*, *y*, and *z* directions, as seen in Figure 4.17. The largest displacements in the *x*, *y*, and *z* directions are 1.6µm, -3.7µm, and 5.9µm respectively. The average displacement per frame in the *x*, *y*, and *z* directions are 0.7µm, 1.4µm, and 2µm respectively. This is expected, as the translation stages have a resolution of 1 µm. The stroke applied to samples between subsequent frames in the composite braid tensile tests is 159µm in the *y* direction. The average camera motion displacements in the *x*, *y*, and *z* directions are 0.45%, 0.9%, and 1.25% of the stroke motion respectively, which are on the same scale as the resolution of the camera system (1.54µm). The shifts in the *x* and *y* directions are minor compared to the size of the captured image frames (8.854mm by 6.674mm). While

traversing, the orientation and relative position of the cameras is maintained, and thus should not affect the calibration.

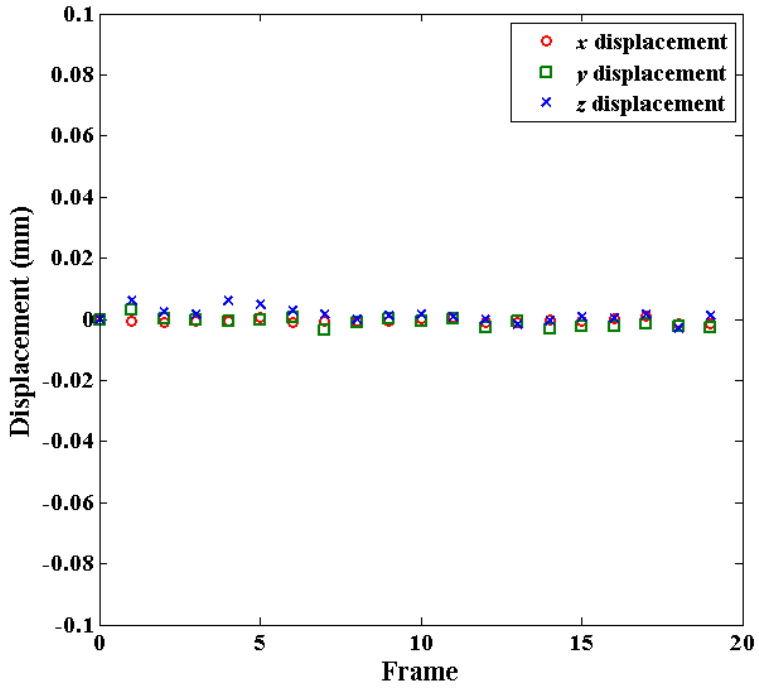

Figure 4.17 - – *x*, *y*, and *z* displacement results of the camera traverse stability test.

4.3.2 Preliminary Radius Measurement under Tensile loading Test Results

The radius change of the PVC tube as a result of strain in the axial direction is presented in Figure 4.18. When measuring the PVC tube radius using the micrometer, the measurement arms contact the surface of the tube, pushing in the tube walls, potentially giving a smaller radius. The initial DIC radius measurement of 5.02mm overestimates the micrometer radius measurement of 4.90±0.12mm by 2.5%. The DIC measurements do not contact the tube, and thus make an initial radius measurement on an undeformed sample and should be more accurate. During loading the sample became taut after the 4th frame and began to strain. A stroke of 12mm, or an expected strain of 12.08% on the 99.31mm long sample, should occur over the 16 remaining. A final strain of 11.7% was

measured by DIC. At this final strain, the DIC measured radius of the sample has reduced by 5.1% to 4.762mm.

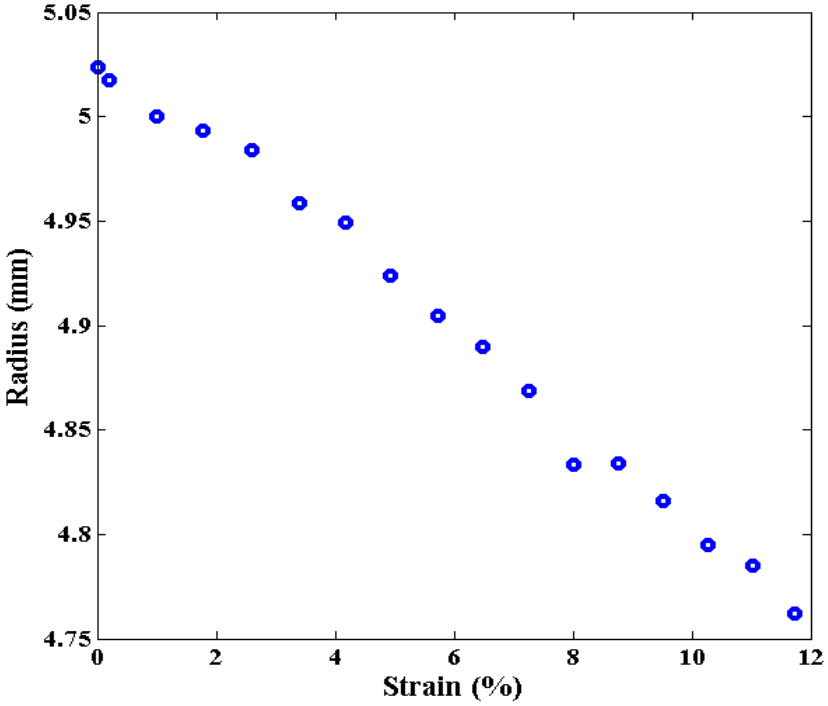

Figure 4.18 – The radius decrease of a PVC tube as it is strained in the axial direction

4.3.3 Braid Radius Measurement Under Tensile Load Test Results

Within each test, a braided composite sample is loaded unaxially from an unloaded state to failure. The stereomicroscope cameras captured this motion with the left and right cameras and 3D surfaces were reconstructed. The progression of one test sample from an unloaded state to failure is shown in Figure 4.19, as captured by the cameras and reconstructed surfaces. In an unloaded state (Figure 4.19(a)) the high points of the surface are above the middle of the focal plane. The zero position in the scale provided in the 3D reconstructions is at the middle of the focal plane. The sample is loaded, reaching strains of 0.69% in Figure 4.19(b) and 1.87% in Figure 4.19(c). Cracks begin to form in the matrix of the composite, and can be seen in bottom right edge of the central unit cell in the surface reconstruction of Figure 4.19(d). Matrix cracks grow and coalesce, allowing

the braid surface to shift quickly. At complete failure, reinforcing fibers can be seen between surface gaps in the left and right camera images of Figure 4.19(e). Surface gaps show up in the 3D reconstructed surface as ridges, which can be seen at numerous locations of the surface reconstruction. The DIC system calculated average strains of 4.20% and 8.82% in Figure 4.19(d) and (e), respectively. However, these strains could be inaccurate due to the matrix cracking that allows separated pieces of the speckled surface to shift apart. It is also possible to measure strains locally on the surfaces to determine differences between regions. The surface heights of the reconstructed braid surface recedes by 0.5623mm in the *z*-direction at a strain of 1.82% just before failure. This can be seen by referring to the scale in the surface reconstructions as the peak of the central unit cell shifts from red in Figure 4.19(a) to yellow in Figure 4.19(d).

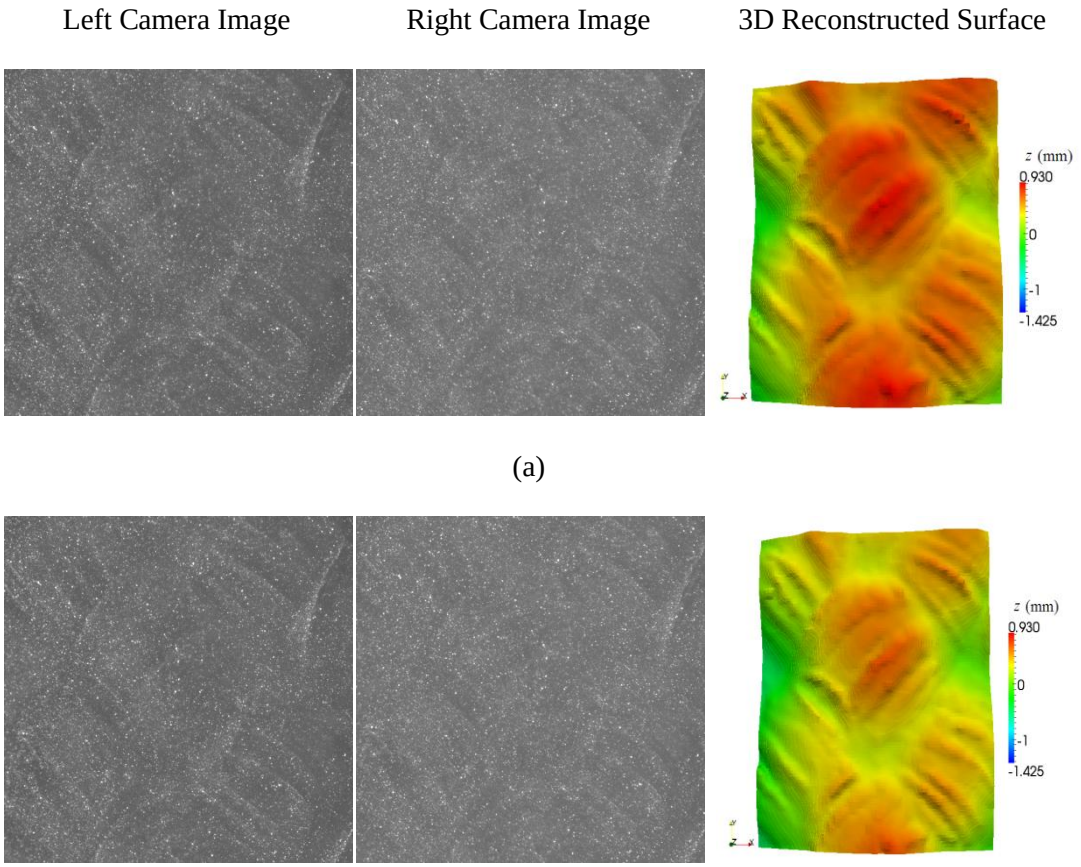

(a)

(b)

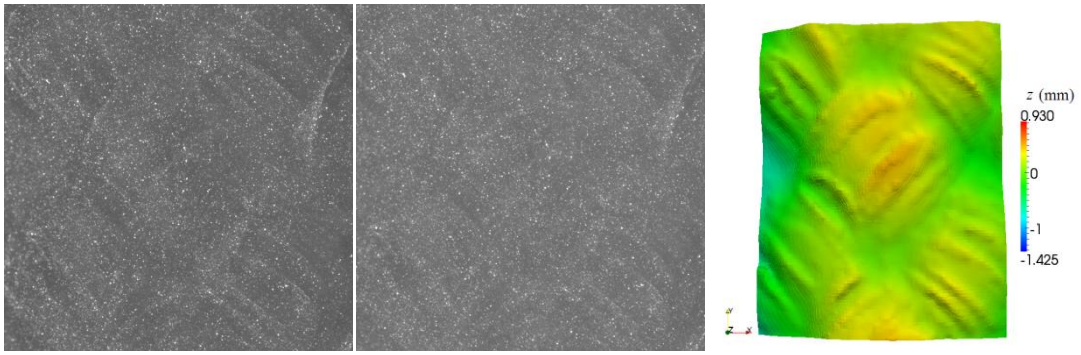

(c)

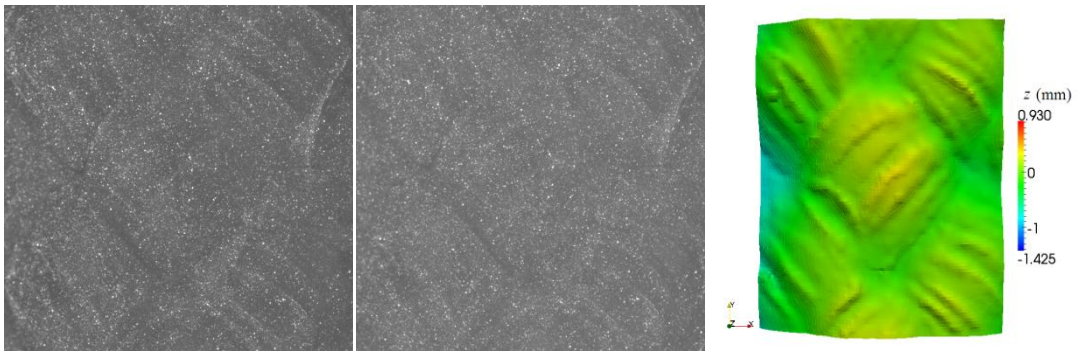

(d)

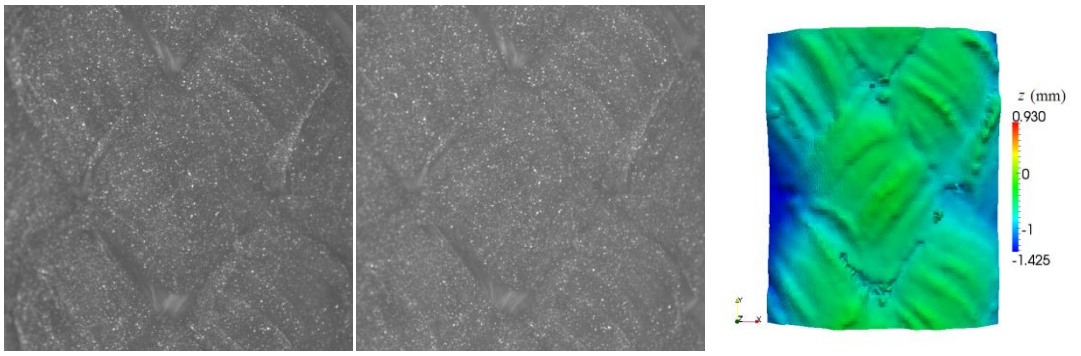

(e)

Figure 4.19 – The left and right camera images with the resulting 3D surface of one test sample as it progresses from (a) an unloaded state to (e) failure

The 3D surface reconstructions in Figure 4.19 can be looked at again using a colour scale relative to the highest point (largest *z* value) on the surface. The new surfaces are presented in Figure 4.20. The red and yellow regions can be seen growing as we progressing from Figure 4.20(a) to Figure 4.20(e). This indicates that the unit cells are flattening. In Figure 4.20(e) a large amount of the surface has become red and yellow. The central unit cell appears to have receded towards the rest of the braid as the matrix cracked and is unable to maintain the original shape of the braid.

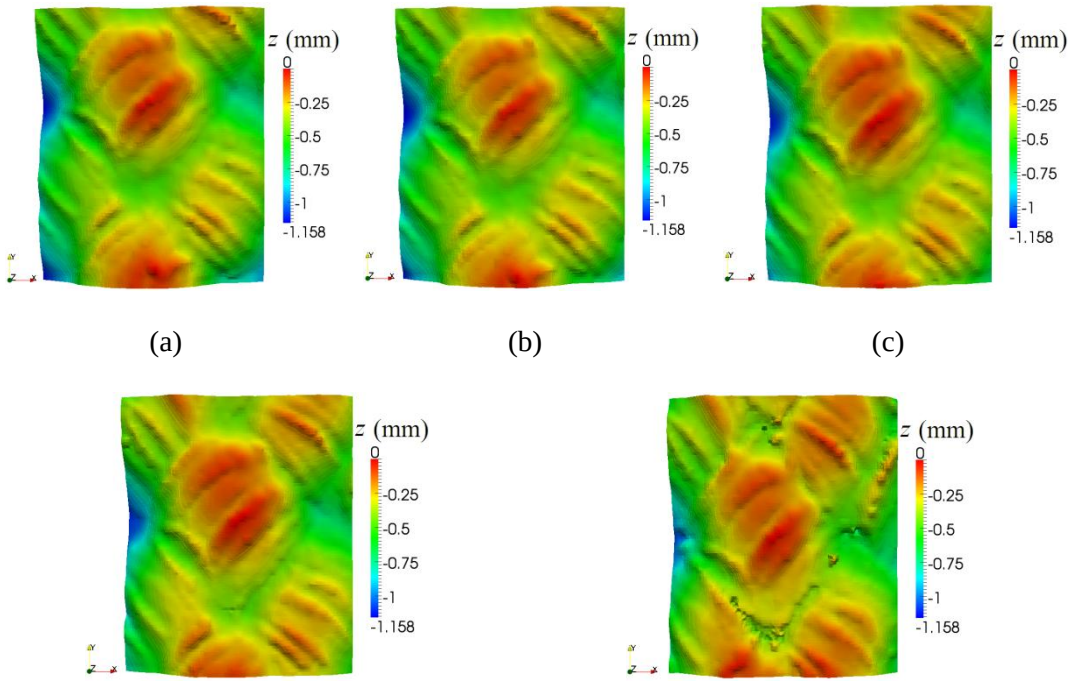

Figure 4.20 – Three dimensional surfaces of a test sample as it progresses from (a) an unloaded state to (e) failure. The colour scale is relative to the highest point on the surface.

Samples reached an average strain of 1.57±0.48% before failure occurred. The average initial braid angles of the samples were 42.48±1.96˚. A proposed model for longitudinal elastic modulus from a study by Carey [22] predicts moduli of 7.8GPa, 7Gpa, and 6GPa at braid angles of 40°, 42.5, and 45° respectively. The braid angle variation means the

strains can deviate by 10% above and 14% below the mean. Displacements and strains were calculated from the images. However, matrix cracking was not always present at the location where images were captured. Images with large crack formation may have experienced local stress and strain concentrations, and would result in larger calculated strains compared to image sets with little or no cracking. The manual application of epoxy matrix resin to the fiber preform can produce in an imperfect matrix, resulting in local stress and strain concentrations. Finally, the braids may experience combined loading due to misalignments between the end tabs. These factors contribute to the deviation in strains reached at failure.

4.3.3.1 Radius measurement results using the area method

The area method radius measurements in region 1 for all samples over the entire test duration are given in Figure 4.21(a). The average measured radius of the unloaded samples is 5.36±0.40mm. A sharp drop in the measured radius is an indication that the sample has failed. Failures occur as early as frame 14, with the majority failing at frame 18. In Figure 4.21(b), radius measurements made after sample failure are not shown. Sample measurements made after sample failure are removed in all further plots, unless otherwise specified.

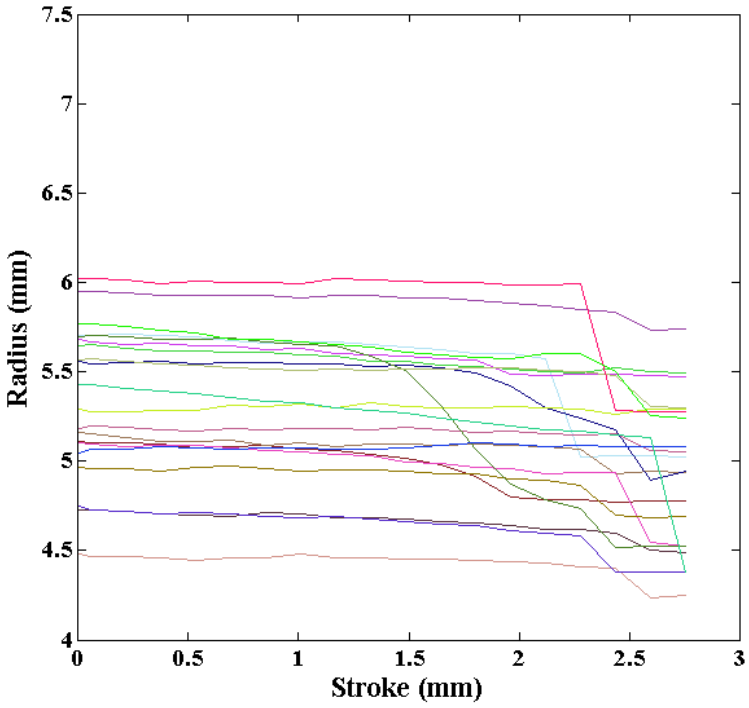

(a)

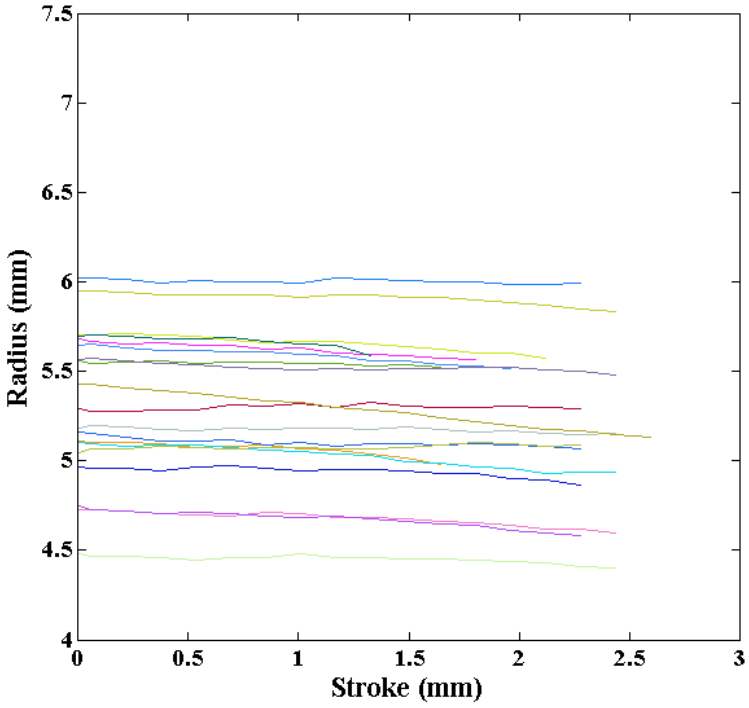

(b)

Figure 4.21 – The area method radius measurements of all samples (a) for full image sets and (b) with measurements after sample failure removed.

The relation between stroke and average strain in region 1 for all samples is given in Figure 4.22. Early sample failure, at frame 14, corresponds to a stroke of 1.802mm and strain of 1.14±0.44%. The latest sample failures occur at frame 18, at a stroke of 2.438mm and strain of 1.62±0.84%. The average strain reached by samples before failure is 1.57±0.48%. All strains were calculated from the displacement vector fields.

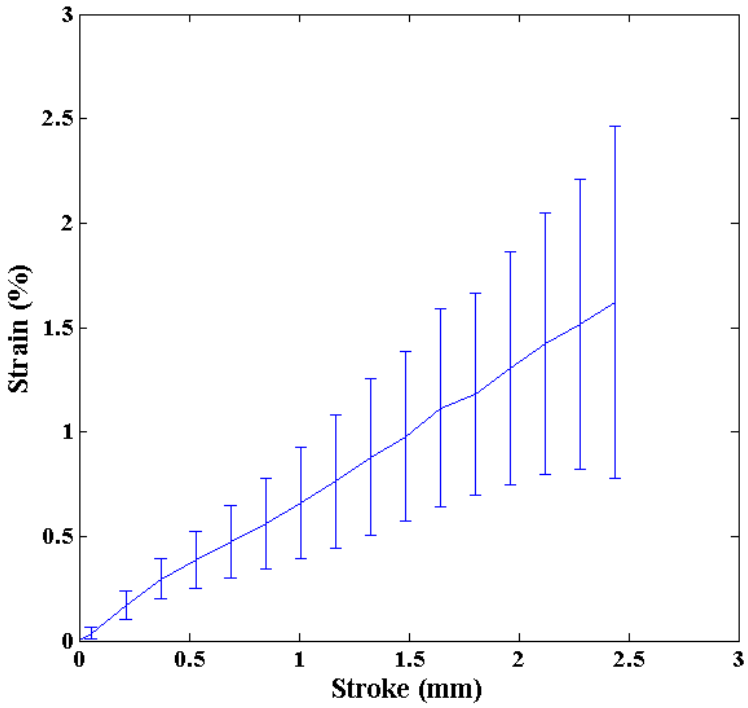

Figure 4.22 – The average strain as a function of stroke for all samples in region 1

The difference in radius measurement between the initial frame (frame 1) and a later frame gives the change in radius of a sample resulting from loading. The cumulative change in radius at each frame was averaged over all samples and is shown in Figure 4.23. At the final frame the average total radius change of all samples is -0.072±0.095mm. The standard deviations increase throughout the test, maintaining a standard deviation of a similar magnitude to the average change.

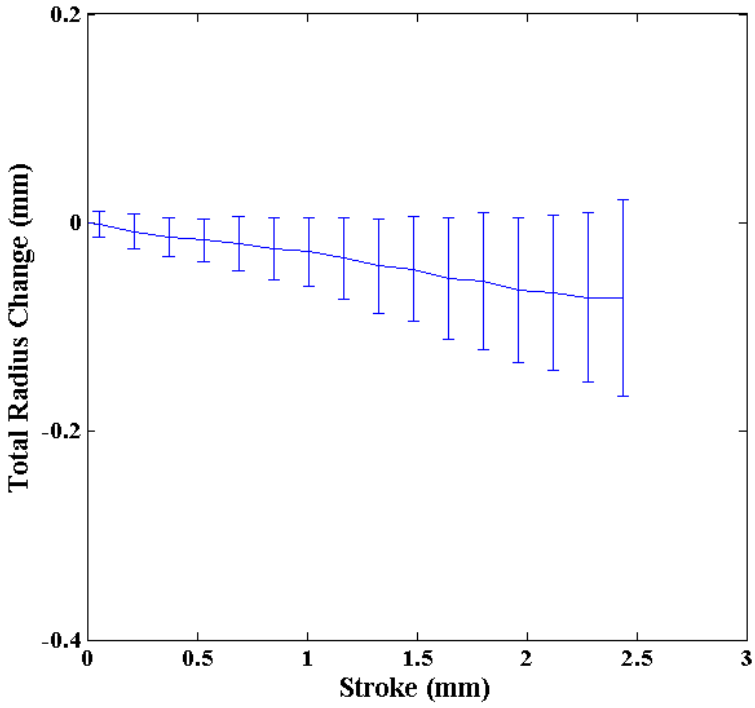

Figure 4.23 – The total radius change as a function of stroke for all samples in region 1 using the area method

To investigate the rate of radius change, the increments of radius change between each subsequent frame were calculated (Figure 4.24). The average incremental radius change between subsequent frames of all samples in region 1 is -0.005±0.011mm.

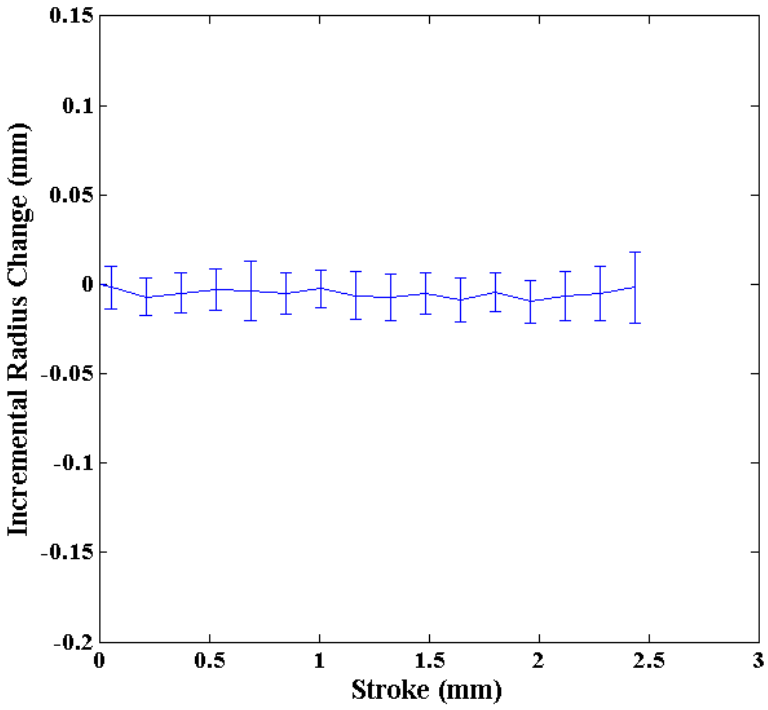

Figure 4.24 – The incremental radius change as a function of stroke for all samples in region 1 using the area method

Images were captured of the unit cells at the three designated regions for each test sample. The measurements in each region can be compared to find out if similar behaviours are being seen across the braid structure. The averaged cumulative radius change for regions 1, 2, and 3 for all samples can be seen in Figure 4.25. The average total radius change experienced before sample failure in regions 1, 2, and 3 are -0.077±0.080mm, -0.118±0.083mm, and -0.113±0.076mm respectively. All regions experienced a decrease in radius on the scale of 100µm. The standard deviations are all within similar ranges. The radius change value in the last frame of region 2 increases as a result of the removal of other failed samples. The last frame of region 2 is an average of the seven remaining samples that have not yet failed. These samples have an average cumulative radius change of -0.056±0.067mm, suggesting that the radius of these remaining samples experienced a smaller change in radius throughout testing.

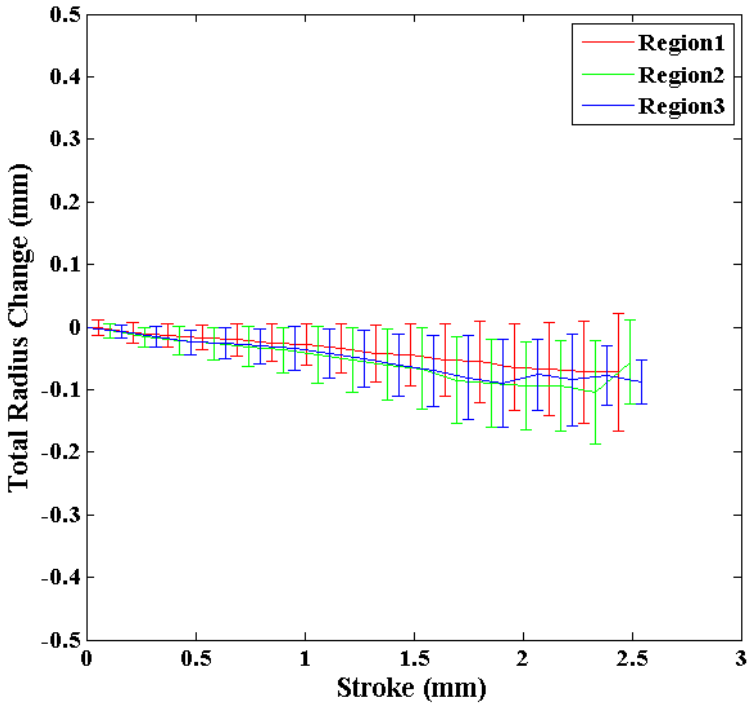

Figure 4.25 – The total radius change as a function of stroke for all samples in regions 1, 2, and 3 using the area method

4.3.3.2 Radius measurements using the band method

The band method radius measurements taken at the peak, mid and valley locations of all samples in region 1 are shown in Figures 4.26(a), (b), and (c). The radius measurements of unloaded samples (frame 1) at the peak, mid and valley locations have radius averages of 5.208±0.264mm, 6.248±0.411mm, and 6.194±0.495mm respectively.

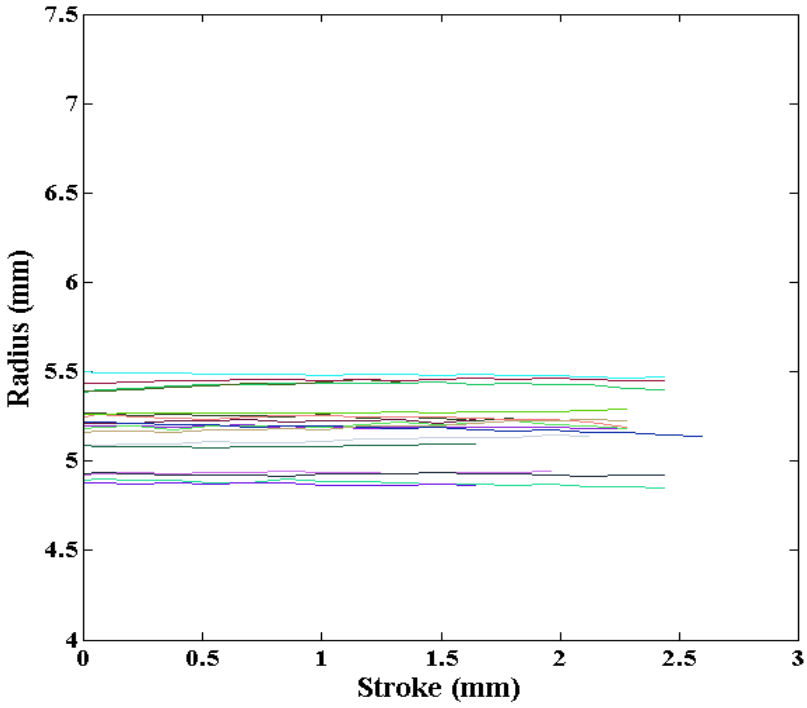
Radius (mm)
Stroke (mm)
7.5
7
6.5
6
5.5
5
4.5
4
0
0.5
1
1.5
2
2.5
3

(a)

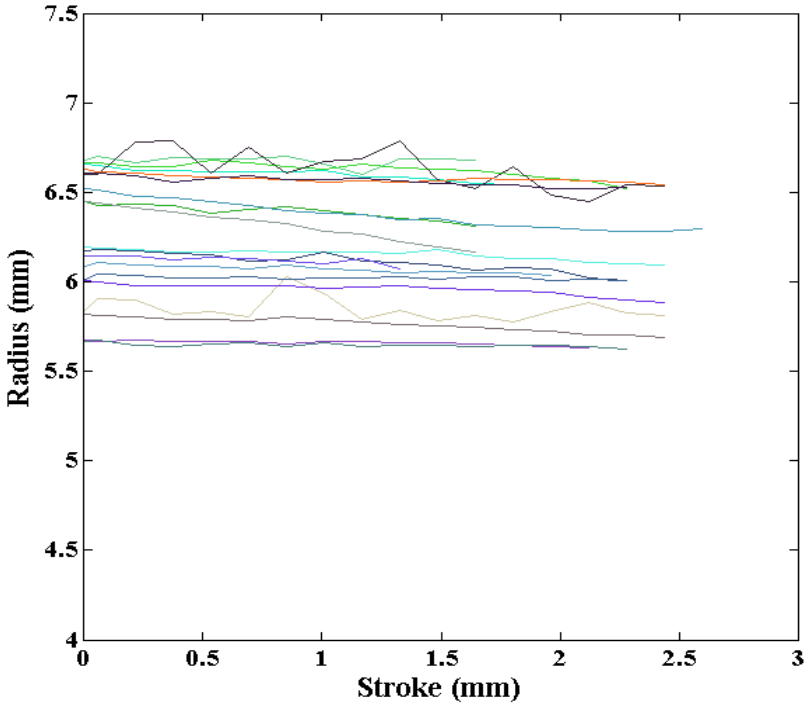
Radius (mm)
Stroke (mm)
7.5
7
6.5
6
5.5
5
4.5
4
0
0.5
1
1.5
2
2.5
3

(b)

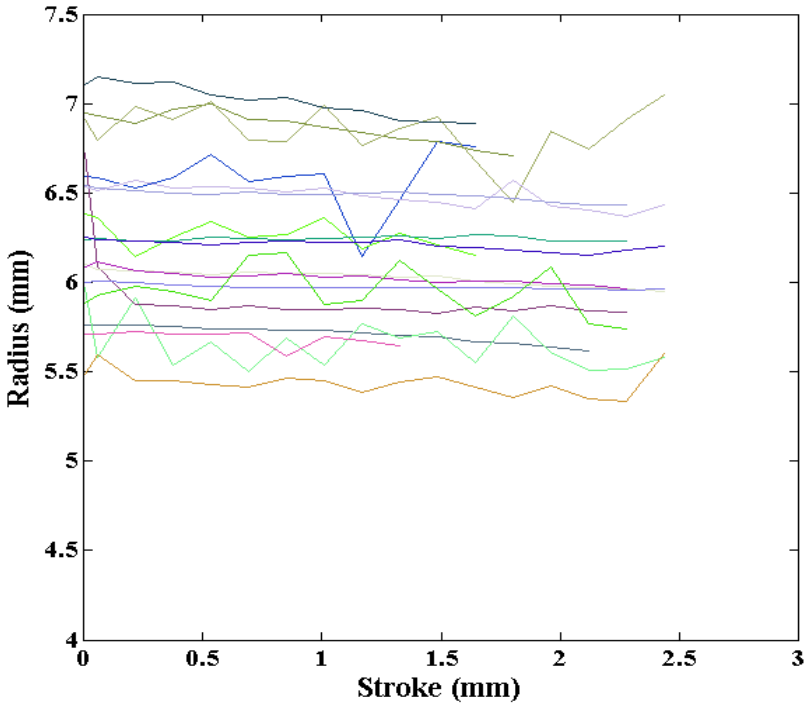

(c)

Figure 4.26 - All sample radius measurements in region 1 taken from the (a) peak, (b) mid, and (c) valley locations using the band method.

The cumulative change in radius at each frame for region 1 was averaged over all samples at each of the three measurement locations (Figure 4.27(a), (b) and (c)). The average total change in radius of all samples before failure at the peak, mid, and valley locations are 0.0058±0.0433mm, -0.1067±0.1078mm, and -0.1023±0.1478mm, respectively. Measurements at the peak location have the smallest deviations. The deviations increase as we move to the mid location and again at the valley location. The mid and valley locations both show decreasing radii with an approximate change of -0.1mm. The average change of 0.0058mm at the peak location suggests an increasing radius, which could potentially be a sign of a negative Poisson's ratio. However, the increase is small compared to the large standard deviations of ±0.0419mm. This behaviour is local as it was not observed in the mid and valley locations. Studies have observed negative through thickness Poisson's ratios in composite laminates [23–25].

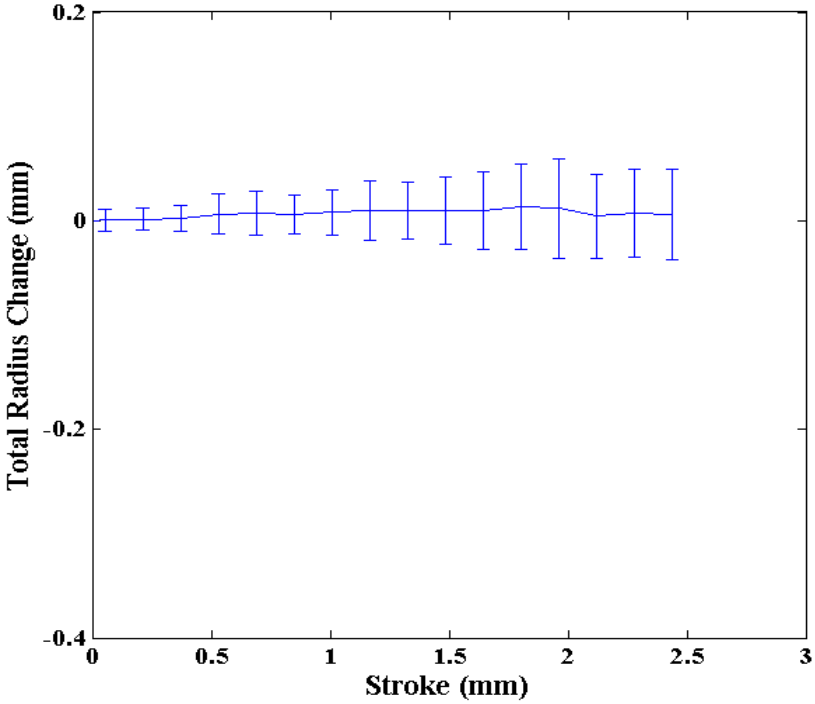
0.2
0
-0.2
-0.4
Total Radius Change (mm)
0
0.5
1
1.5
2
2.5
3
Stroke (mm)

(a)

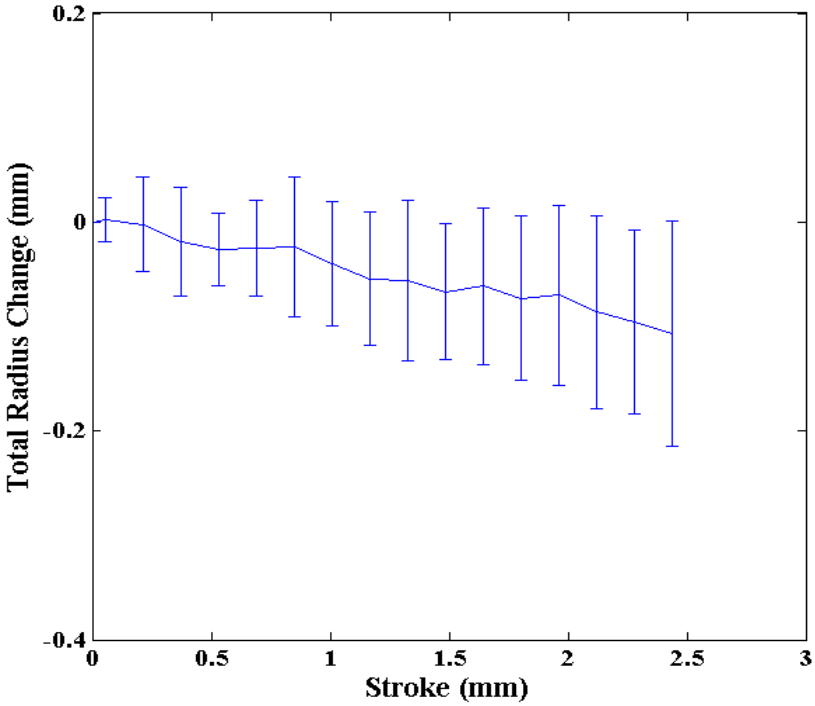
0.2
0
-0.2
-0.4
Total Radius Change (mm)
0
0.5
1
1.5
2
2.5
3
Stroke (mm)

(b)

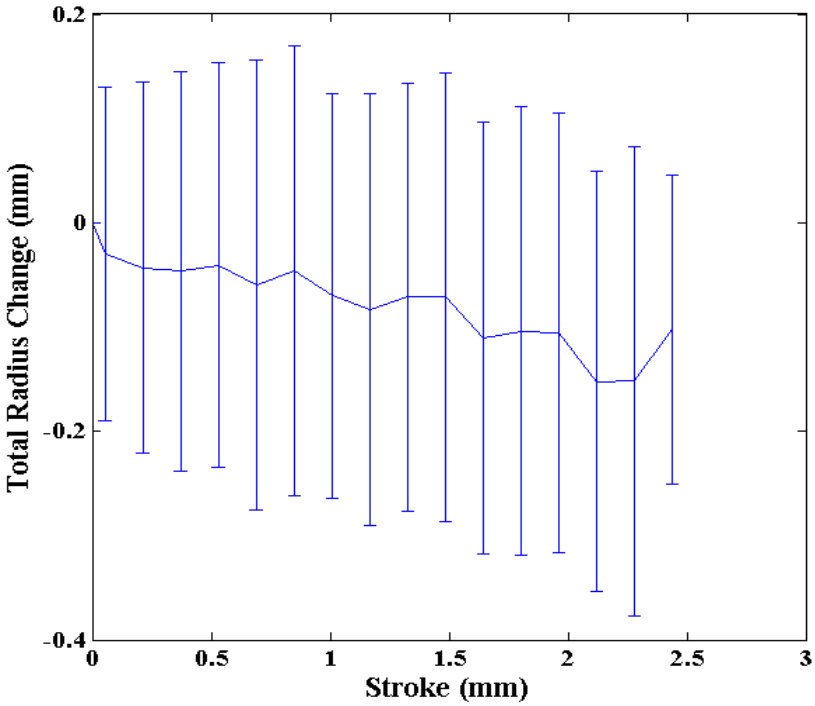

(c)

Figure 4.27 - The total change in radius in region 1 at the (a) peak, (b) mid, and (c) valley locations using the band method.

To investigate the rate of radius change, the increments of radius change between each subsequent frame were calculated. The incremental change at the peak location, Figure 4.28(a), has an average change of 0.0006mm between subsequent frames with the smallest standard deviation of ±0.0097mm. At the mid location, Figure 4.28(b), the average incremental change increases to -0.0067mm as does the standard deviation to ±0.0468mm. For the valley location, Figure 4.28(c), the average incremental change is -0.0007mm with a standard deviation of ±0.0887mm. The incremental change between subsequent frames at the valley location is unpredictable and can be seen jumping between positive and negative values. The radius change increments are generally small, in the range of a micron. A trend in the rate of change is unclear due to the large standard deviations.

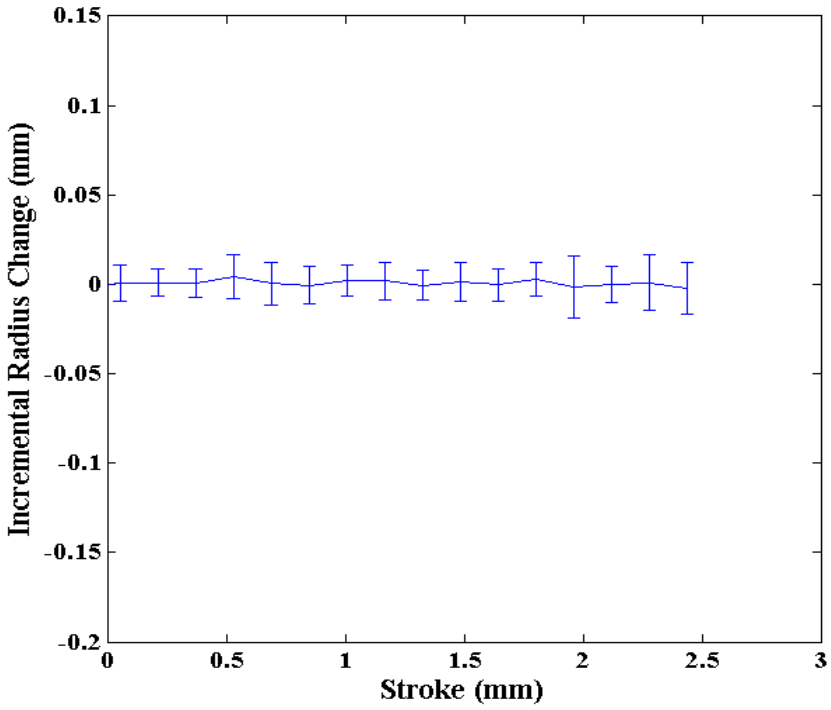
Incremental Radius Change (mm)
Stroke (mm)
0.15
0.1
0.05
0
-0.05
-0.1
-0.15
-0.2
0
0.5
1
1.5
2
2.5
3

(a)

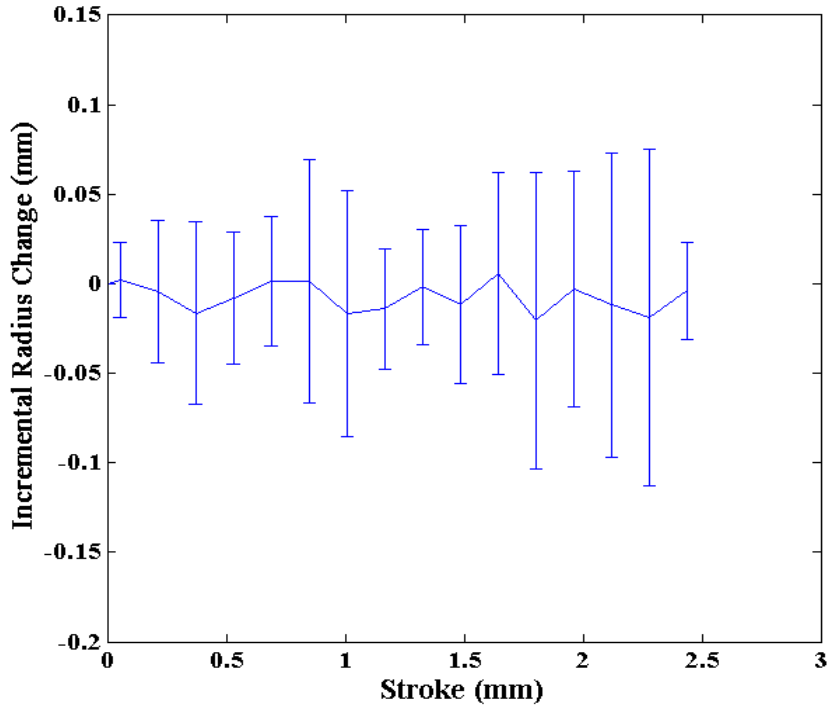
Incremental Radius Change (mm)
Stroke (mm)
0.15
0.1
0.05
0
-0.05
-0.1
-0.15
-0.2
0
0.5
1
1.5
2
2.5
3

(b)

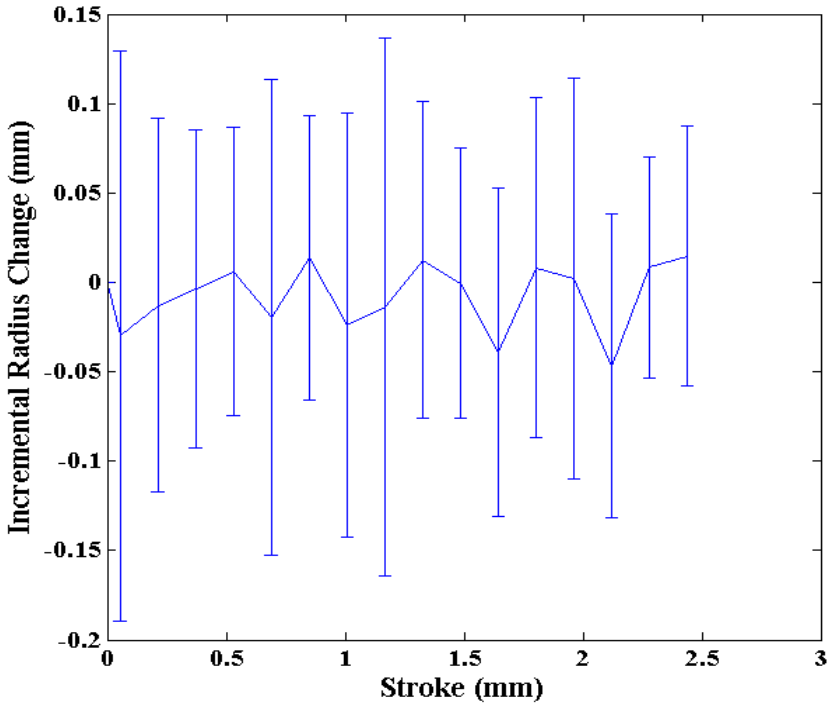

(c)

Figure 4.28 - The incremental change of radius in region 1 at the (a) peak, (b) mid, and (c) valley locations using the band method.

Images were captured of the unit cells at the three designated regions for each test sample. The measurements in each region can be compared to find out if similar behaviours are being seen across the braid structure. In Figure 4.29(a), all three region measurements at the peak location show little to no radius change. The peak location average total change in radii is 0.0058±0.0433mm, 0.0146±0.0545mm, and 0.013±0.0327mm for regions 1, 2 and 3 respectively. The standard deviations in region 1 are 20.5% smaller than region 2 and 32.4% larger than region 3. The mid and valley measurement locations also have strong agreement across all three regions for total radius change and standard deviations, as shown in Figures 4.29(b) and (c). The three regions appear to behave similarly at all three locations.

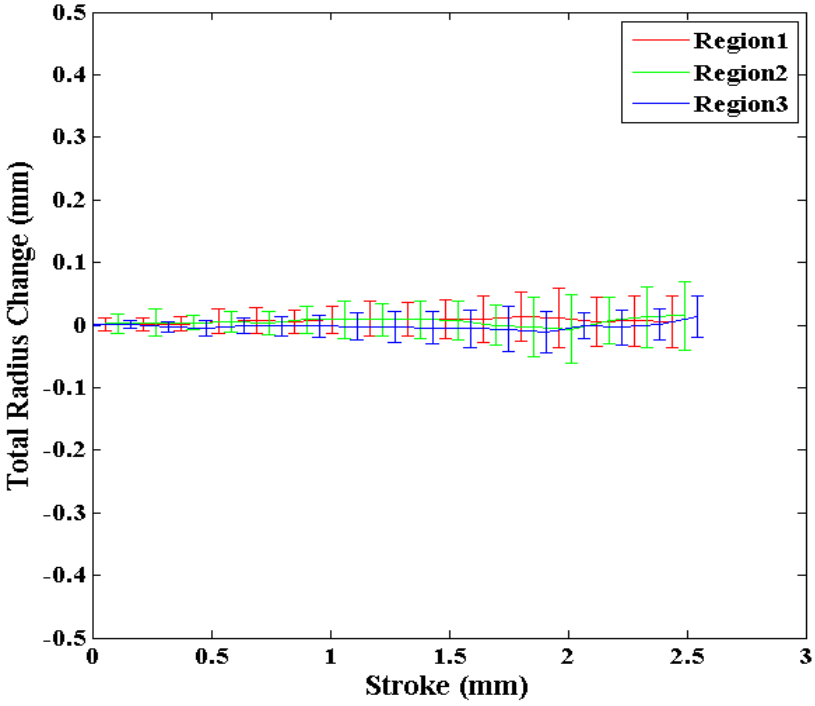
Region1
Region2
Region3
Total Radius Change (mm)
Stroke (mm)
0.5
0.4
0.3
0.2
0.1
0
-0.1
-0.2
-0.3
-0.4
-0.5
0
0.5
1
1.5
2
2.5
3

(a)

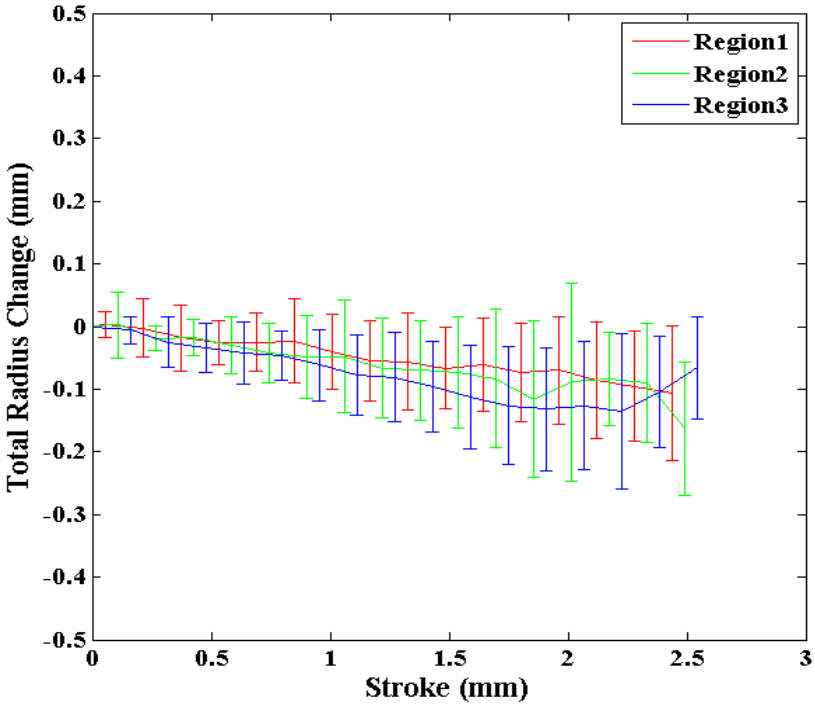
Region1
Region2
Region3
Total Radius Change (mm)
Stroke (mm)
0.5
0.4
0.3
0.2
0.1
0
-0.1
-0.2
-0.3
-0.4
-0.5
0
0.5
1
1.5
2
2.5
3

(b)

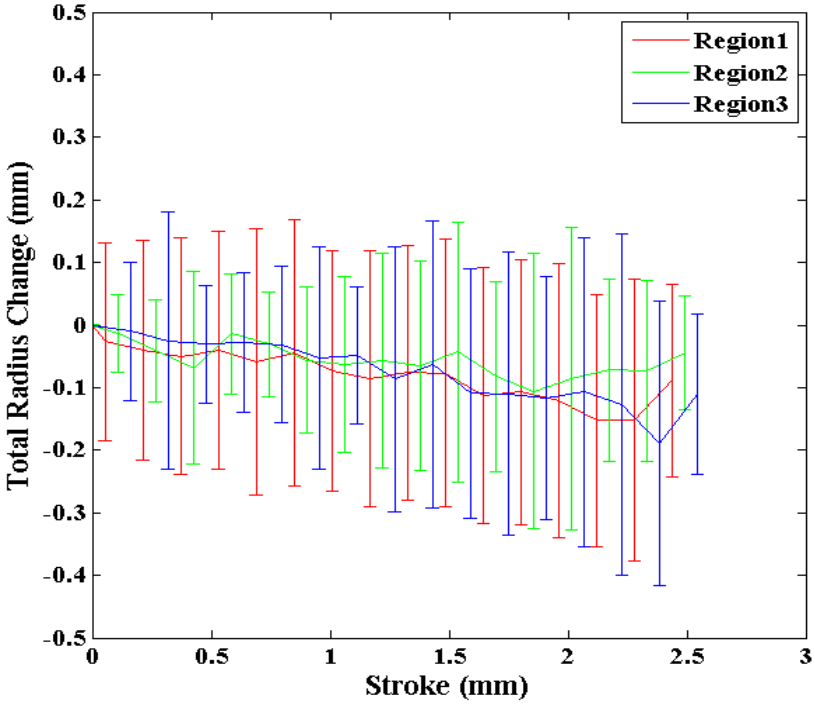

(c)

Figure 4.29 - Comparison of total change in radius measurements of unit cells in neighboring regions at the (a) peak, (b) mid, and (c) valley locations using the band method.

4.3.4 Radius Measurement Discussion

The radii measurements for both area and band measurement methods contain large standard deviations. Possible reasons for the inaccuracy include a shallow focal depth, and rough uneven sample surfaces. The depth of focus of the stereo microscope is 740µm. The images were focused at the centre of the braid with half of the depth of focus extending 0.37mm into the braid. In Figure 4.30 we see that the surface of an idealized tube remains in focus within 3.12mm in either direction from the centre. The reconstructed surface beyond the focal depth cannot be accurately reconstructed, as shown in Figure 4.31, and is removed. The area of surface reconstructed is reduced, limiting the amount of surface available for the circle fitting process.

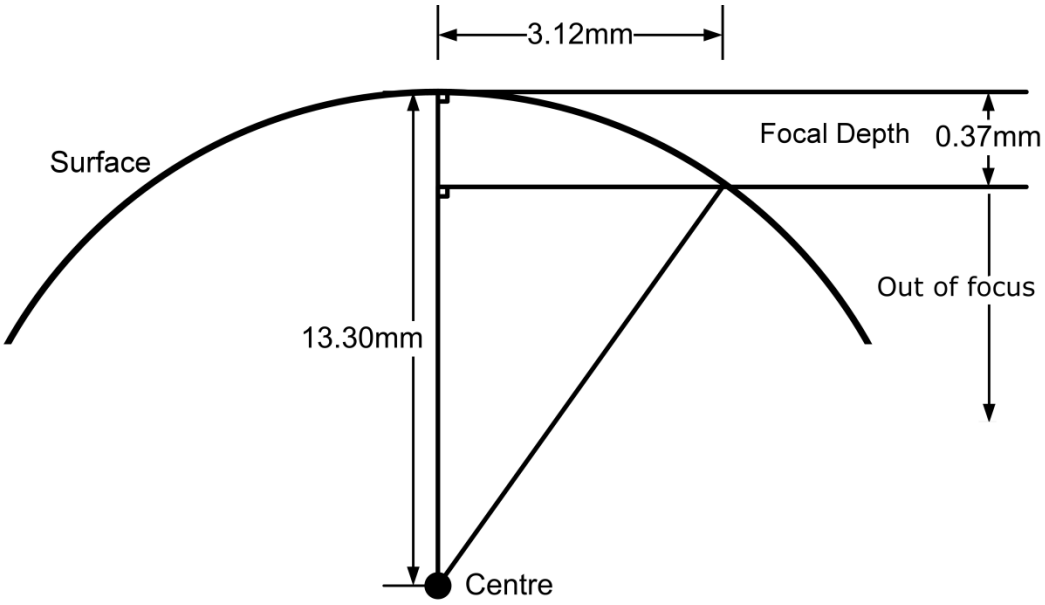

Figure 4.30 – A diagram of an idealized braid surface in and out of the focal depth.

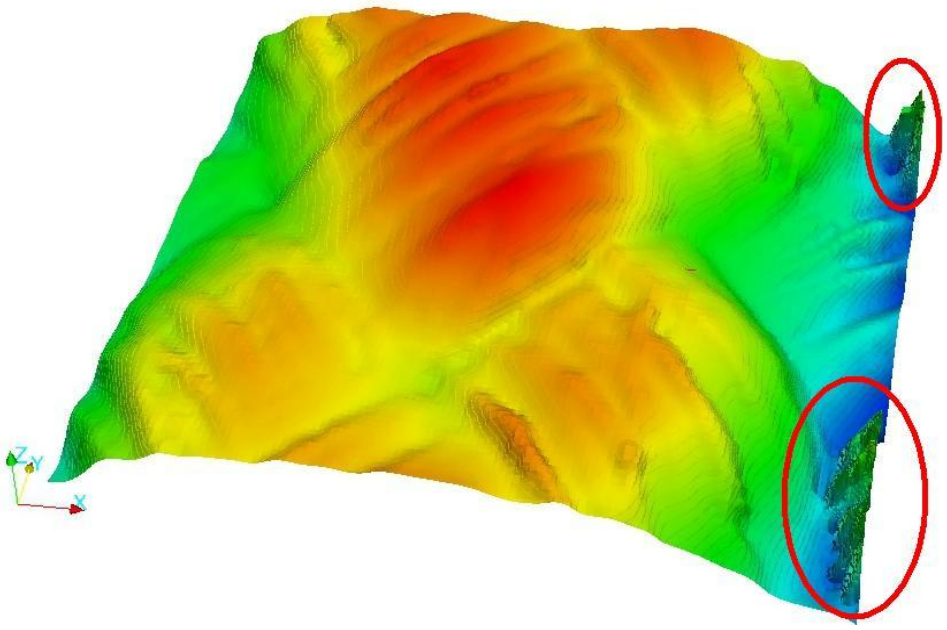

Figure 4.31 – A braided composite surface reconstruction including out of focus regions that are circled in red.

Further explanations for radii measurement inaccuracy can be found by looking at the cross sectional surfaces and estimated circle fits at each of the locations. The surface cross section at the peak location, Figure 4.32(a), shows the peak of the centered unit cell

and the two valleys on either side of the peak. Beyond the valleys there should be two more peaks at the center of the neighboring unit cells. However, the left and right sides are unfocused and cutoff before the neighboring peaks are reached. The cutoff results in the peak location cross section containing more points in the lower parts of the surface. The estimated circle appears to fit more closely to the curvature of the unit cell peak. This greatly decreases the size of the estimated circle fit to the cross section. The estimated circle appears to fit to the curvature of the peak throughout the test, thus resulting in a negligible measured radius change and a small standard deviation of 0.0058±0.0433mm.

At the mid location the surface cross sections have less variation. This is because the peak and valley locations of all nearby unit cells are completely avoided as seen in Figure 4.32(b). The resulting measurements underestimate, but more closely match, the micrometer measured radius than either of the other two measurement locations. This may be because the average surface height along this cross section is catching the lower portions of the surface roughness.

The cross section of the valley location is shown in Figure 4.32(c). The cross sections have a distinct drop in the middle that is surrounded by two peaks of the neighboring unit cells. This is the most variable measurement location. There are unit cells captured on the two sides of the cross section. The surface of the two unit cells makes a very uneven cross section plot. The ends of the cross section may end at high or low surface heights of the unit cells. This leads to a large variation in the estimated circle fits.

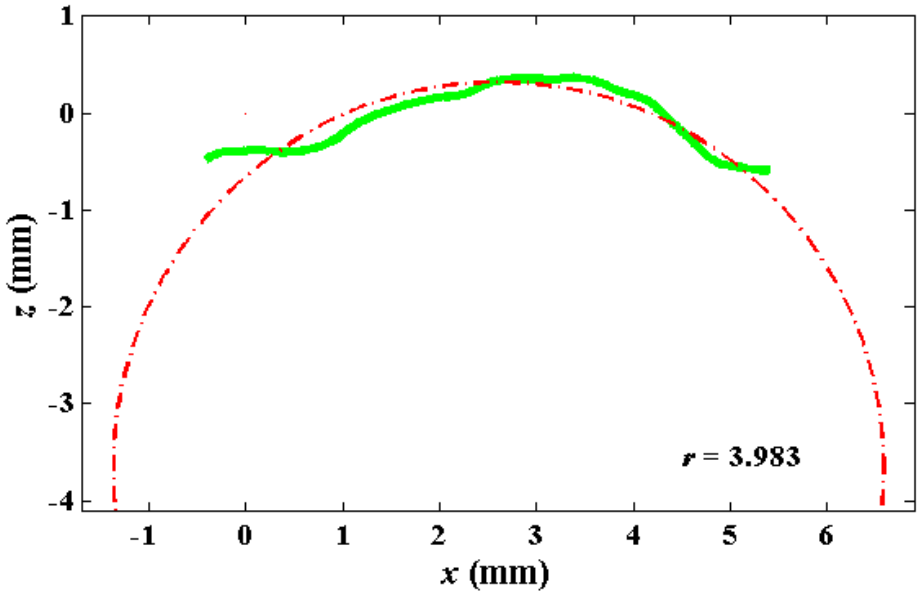

(a)

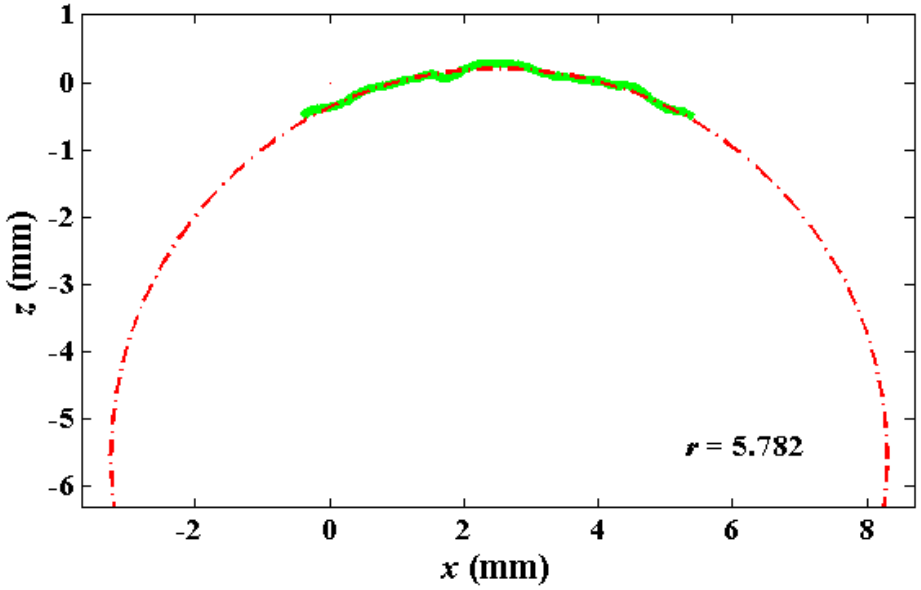

(b)

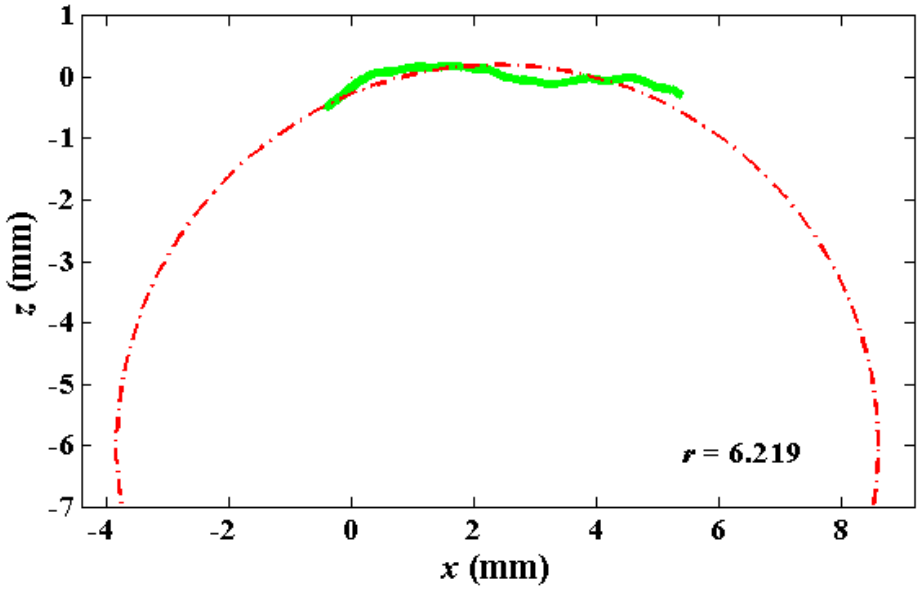

(c)

Figure 4.32 - Circle fits for cross sections located at the (a) peak, (b) mid and, (c) valley regions of a unit cell.

The radii of the braids were measured using a micrometer prior to testing. This measurement is also affected by the surface roughness. The micrometer arms contact surface is a circle with a 5mm diameter. This large surface causes the arm to contact and stop at the peaks of the unit cells. As a result, the micrometer measurements are affected by the surface roughness and measure the outer surface radius. The 3D DIC surface reconstruction measurements fit a circle to the average of the surface. The area method, which averages sixty measurements across a single unit cell, minimizes the impact of surface roughness. Radii measurements using the area method should give an outer radius measurement that averages the peaks and valleys across and thus should be smaller than the micrometer measurements. The average unloaded sample radii measured from region 1 using the area method is 5.36±0.40mm, which is 19.4% smaller than the micrometer measurement of 6.65±0.06mm. The wall thickness of the braids is 1.02±0.05mm which suggest a strand thickness of 0.51mm. The difference between surface heights at the peak

and valley locations is assumed to be 0.51mm. However, the inside surface of the braids contacted the mandrel during curing and are smooth. Thus, the difference in surface height is likely more than half the wall thickness. The DIC measurement method considers surface features and measures the average radius of these features, while the micrometer measures the radius given by the peak surface features. Furthermore, the DIC area measurement method was heavily influenced by the peak location surface features. The circle fit equation was shown to fit more closely to the peak surface feature rather than the overall surface features due to a limited fitting surface. This could explain the difference between the DIC area method averages and micrometer measurements. The band method averages measurements in a much thinner, band making it susceptible to both the peaks and the valleys of the surface roughness. As discussed above, the location of the band introduces specific surface features that largely influence the measurement. This is not an ideal method for determining the average outer radius resulting from composite braid surface roughness. However, the measurements in the peak, mid and valley locations give an idea as to how the area measurement is influenced by surface roughness.

The mandrel used to cure the composite braids had an outer radius of 5.69mm and should be similar to the inner radius of the composite braid samples. Thus, one would expect the initial sample radii to be between the inner radius of 5.69mm and the outer radius of 6.65mm resulting from the surface roughness peaks, as measured by the micrometer. The area method gave a measured unloaded sample radii in region 1 of 5.36±0.40mm, which is below the expected range. Band method measurements in the peak location have an average of 5.208±0.264mm, which is also below the expected range. Only the band method measurements in the mid and valley regions, with averages of 6.248±0.411mm, and 6.194±0.495mm respectively are within the expected range. The area method

measurement has only a 2.8% difference from the band method measurements at the peak location. This suggests that the average of measurements across a unit cell is strongly influenced by the surface roughness peaks similar to what was seen in the peak location measurements. At this magnification the limited surface and surface features are enough to bias the radius measurements, particularly in the peak measurement location.

From these results it is difficult to quantify a change in radius. In the mid and valley regions we have an average change of approximately -0.1mm. Calculating from the averaged values of the braid samples, There is an average undeformed outer . The average undeformed cross sectional area of the braids is 39.41mm^2. If the thickness is held constant but the outer radius has decreased from loading the deformed cross section is 38.77mm^2. The total difference in cross sectional area after the radius change is -1.7% over a strain range of 1.84%. This would lead to an increase in the stress.

The thickness also affects the cross sectional area but cannot be measured with the current images captured. Biaxial braided composites are similar to angle-ply laminates [±θ]s, which can be described using classical laminate theory (CLT) [26]. Using CLT to calculate the through thickness Poisson ratio of 0.32 for the composite, the thickness change resulting from loading was estimated as -5μm. The combined radius and thickness change results in a 2.12% decrease in cross sectional area before sample failure. The effect of cross sectional area change due to radius and thickness change can be found in Figure 4.33. In the plot the reduction in area was applied linearly such that the total cross sectional area reduction is reached at the end. The stress strain response has three distinct zones with linear slopes between 0-0.6% strain (zone 1), 0.6-0.96% strain (zone 2), and 0.96%-1.69% strain (zone 3). The tangent moduli for the constant cross sectional area plot are 5.48Gpa, 9.16GPa, and 3.95GPa in zones 1, 2, and 3 respectively, with an average modulus of 6.06GPa. The radius and thickness reduced cross sectional area plot

tangent moduli are 5.52Gpa, 9.27GPa, and 4.07GPa in zones 1, 2, and 3 respectively, with an average modulus of 6.15GPa.

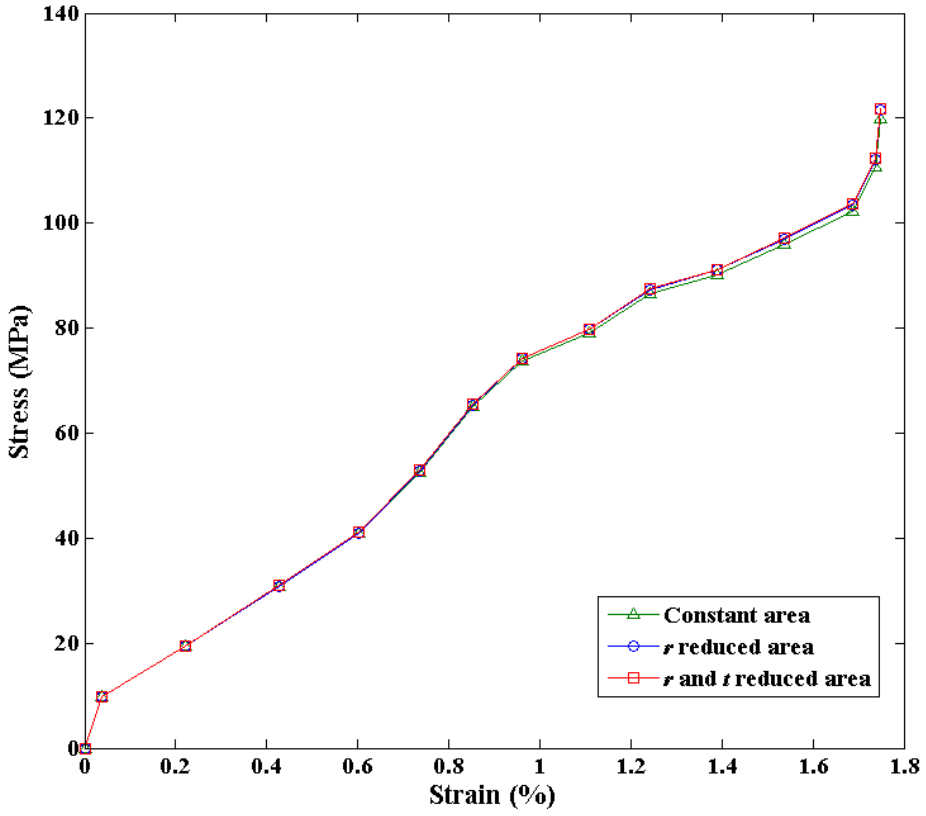

Figure 4.33 – A stress strain plot showing the effect of reduced cross sectional area from changing radius and thickness. Lines are for visual purposes only.

A study by Carey [22] loaded braided composite tubes uniaxially and compared the experimentally determined longitudinal elastic modulus as a function of braid angle to a prediction model. The expected longitudinal elastic modulus from the proposed model overestimated the experimentally determined values. In this study the cross sectional area was considered constant, thus engineering stress was used. A longitudinal elastic modulus of 6.25GPa was experimentally determined for samples with braid angles of 42.5°. A reduction in cross sectional area of 2.12% would increase the calculated longitudinal elastic modulus to 6.38GPa. The proposed model predicts a longitudinal

elastic modulus of approximately 7GPa for a braid angle of 42.5°. The reduction in cross sectional area due to radius and thickness change does not fully bridge the gap between experimental and predicted values. However, the braid angle may also be changing during tensile loading and could potentially explain the remaining discrepancy between the experimental values and the proposed model in the study.

The matrix constitutes approximately 40% of a composites volume and can largely influence the longitudinal elastic modulus [22]. The resin used in the manufacturing of the braided composite samples for this study gave a rigid matrix. However, braided composites can also be manufactured with an elastomeric matrix. The main difference is that elastomers have a low modulus of elasticity compared to rigid epoxies [22]. Thus we would expect an elastomeric polymer matrix composite to reach higher strains resulting in further reduction of both radius and wall thickness.

The composite braid features captured in the 3D surface reconstructions show the surface roughness in great detail. Smaller fiber bundle ridges could even be seen on the main strands (Figure 4.5). Features such as these could be identified and measured to determine locations of stress concentrations. Cross sections can be drawn in any direction to obtain information about the surface topography of a braid. For example, a cross section following the direction of travel of a strand could help describe the undulation angle. Geometric features can be identified and used to help verify current models.

4.4 Conclusions

The radius change of tubular composite braids under axial loading was examined using 3D DIC surface reconstructions. Surface reconstruction measurements were made using two methods; the area method and the band method. Unloaded braid radius measurements fell below the expected range of 5.69-6.65mm when using the area method

or the band method in the peak location. However, mid and valley measurements using the band method fall within the expected range. Possible explanations for the inaccuracy were discussed; major issues were a limited surface to fit a circle to and a high degree of surface roughness. Measurements were consistent when comparing across all three regions, suggesting that evaluating one unit cell in the gauge length is sufficient to describe radius change throughout the braid. The results from this test suggest that the composite braids experience a small decrease in radius on the order of 0.1mm. This radius change would decrease the cross sectional area, increasing the stress and affecting the calculated moduli. The decrease of radius and it's affects on stress and moduli calculation would be further amplified for elastomeric resin based composites.

4.5 References

[1] J. Carey, M. Munro, and A. Fahim, "Longitudinal Elastic Modulus Prediction of a 2-D Braided Fiber Composite," *Journal of Reinforced Plastics and Composites*, 2011.

[2] J. Carey, A. Fahim, and M. Munro, "Design of braided composite cardiovascular catheters based on required axial, flexural, and torsional rigidities.," *Journal of biomedical materials research. Part B, Applied biomaterials*, vol. 70, no. 1, pp. 73-81, Jul. 2004.

[3] H. Ghiasi, L. Lessard, D. Pasini, and M. Thouin, "Optimum Structural and Manufacturing Design of a Braided Hollow Composite Part," *Applied Composite Materials*, vol. 17, no. 2, pp. 159-173, Oct. 2009.

[4] P. Potluri, A. Manan, M. Francke, and R. Day, "Flexural and torsional behaviour of biaxial and triaxial braided composite structures," *Composite Structures*, vol. 75, no. 1–4, pp. 377-386, Sep. 2006.

[5] L. B. Meng, G. C. Jin, X. F. Yao, and H. Y. Yeh, "3D full-field deformation monitoring of fiber composite pressure vessel using 3D digital speckle correlation method," *Polymer Testing*, vol. 25, pp. 42-48, 2006.

[6] D. M. Revilock Jr, J. C. Thesken, B. H. Suite, W. Conshohocken, and B. S. Forsythe, "3D Digital Image Correlation of a Composite Overwrapped Pressure Vessel During Hydrostatic Pressure Tests."

[7] P. F. Luo, "Measurement of curved surface by stereo vision and error analysis," *Optics and Lasers in Engineering*, vol. 30, no. 6, pp. 471-486, Dec. 1998.

[8] C. K. Leung, G. Melenka, D. S. Nobes, and J. P. Carey, “Validation of DIC as an Effective Tool for Composite Tubular Braid Characterization,” *CSME International Congress 2012*, pp. 1-6, 2012.

[9] B. Pan, “Accurate Measurement of Satellite Antenna Surface Using 3D Digital Image Correlation Technique,” *Strain*, vol. 40, no. 2, pp. 393-200, Apr. 2009.

[10] P. F. Luo and J. N. Chen, “Measurement of curved-surface deformation in cylindrical coordinates,” *Experimental Mechanics*, vol. 1, no. 3, pp. 133-350, Dec. 2000.

[11] C. Ayranci and J. Carey, “2D braided composites: A review for stiffness critical applications,” *Composite Structures*, vol. 85, no. 1, pp. 43-58, Sep. 2008.

[12] C. Ayranci and J. P. Carey, “Experimental Validation of a Regression-Based Predictive Model for Elastic Constants of Open Mesh Tubular Diamond-Braid Composites,” *Polymer*, 2011.

[13] C. Ayranci, D. Romanyk, and J. P. Carey, “Elastic Properties of Large-Open-Mesh 2D Braided Composites: Model Predictions and Initial Experimental Findings,” *Polymer*, 2010.

[14] B. Pan, K. Qian, H. Xie, and A. Asundi, “Two-dimensional digital image correlation for in-plane displacement and strain measurement: a review,” *Measurement Science and Technology*, vol. 20, no. 6, p. 062001, Jun. 2009.

[15] LaVision GmbH, “DaVis 72 Product Manual - StrainMaster 3D - Getting Started.” Gottingen, Germany, p. 92, 2007.

[16] T. A. Berfield, J. K. Patel, R. G. Shimmin, P. V. Braun, J. Lambros, and N. R. Sottos, “Micro- and Nanoscale Deformation Measurement of Surface and Internal Planes via Digital Image Correlation,” *Experimental Mechanics*, vol. 47, no. 1, pp. 51-62, Jan. 2007.

[17] W. Sharpe and W. Sharpe Jr., *Springer Handbook of Experimental Solid Mechanics*. Berlin: Springer, 2008, p. 1098.

[18] G. Besnard, B. Etchessahar, J.-M. Lagrange, C. Voltz, F. Hild, and S. Roux, “Metrology and detonics: analysis of necking,” *Proceedings of SPIE*, vol. 7126, p. 71261N-71261N-12, 2008.

[19] R. Y. Tsai, “A Versatile Camera Calibration Technique for High-Accuracy 3D Machine Vision Metrology Using Off-the-shelf TV Cameras and Lenses,” no. 4, 1987.

[20] G. H. Golub and R. Strebel, “Least-Squares Fitting of Circles and Ellipses,” *Update*, vol. 34, pp. 558-578, 1994.

[21] A. Harte, “On the mechanics of braided composites in tension,” *European Journal of Mechanics - A/Solids*, vol. 19, no. 2, pp. 259-275, Mar. 2000.

[22] J. Carey, A. Fahim, and M. Munro, “Predicting Elastic Constants of 2D-Braided Fiber Rigid and Elastomeric-Polymeric Matrix Composites,” *Journal of Reinforced Plastics and Composites*, vol. 23, no. 17, pp. 1845-1857, Nov. 2004.

[23] M. Miki and Y. Murotsu, “The Peculiar Behavior of the Poisson’s Ratio of Laminated Fibrous Composites,” *JSME Internation Journal*, vol. 32, 1989.

[24] C. T. Herakovich, “Composite Laminates with Negative Through-the-Thickness Poisson’s Ratios,” *Journal of Composite Materials*, vol. 18, no. 5, pp. 447-455, Jan. 1984.

[25] G. W. Milton, “COMPOSITE MATERIALS WITH POISSON’S CLOSE TO -1,” *Journal of Mechanical Physics of Solids*, vol. 40, 1992.

[26] J. Tate, A. Kelkar, and J. Whitcomb, “Effect of braid angle on fatigue performance of biaxial braided composites,” *International Journal of Fatigue*, vol. 28, no. 10, pp. 1239-1247, Oct. 2006.

Chapter 5: Tubular Composite Braid Angle Change Under Tensile Loading

5.1. Introduction

Braids are cross ply composites, where the strand angles are mirrored about the central axial axis of the structure. The braid angle (θ) is the angle of the strands relative to the axial direction of the braid, as shown in Figure 5.1. It is an important geometric factor that greatly affects the mechanical properties of composite braids. The strength and stiffness of a composite braid can be largely influenced by braid angle [1].

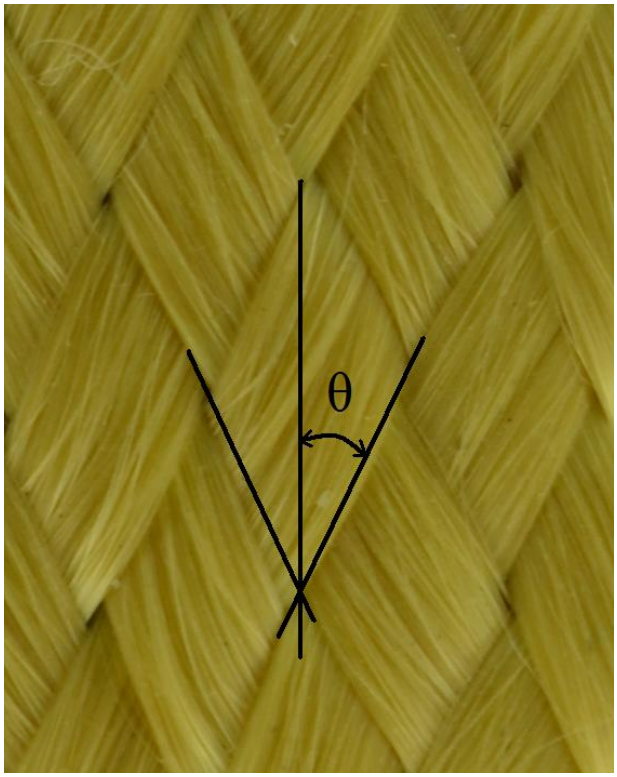

Figure 5.1 – The braid angle of a textile.

Many studies have looked at the effect of braid angle on elastic properties of composite braids, both experimentally [2–5] and theoretically [6–10]. Xu et al modeled biaxial and triaxial braids of differing textile architectures to predict the material properties with relation to the braid angle [6]. Other studies looked into the effect of fiber architecture on

the deformation and elastic moduli of braided composites both experimentally and analytically [1, 2, 4, 7, 11, 12]. However, these studies assume that the braid angle remains constant during loading. Studies focusing on the change in braid angle during loading have not been found.

The effect of braid angle on the longitudinal, transverse, and shear moduli of closed mesh braids can be seen in Figure 5.2. Between 30-40˚ the longitudinal modulus (Ex) are highly affected by a changing braid angle, whereas the transverse modulus (Ey) is affected most between braid angles of 50-60˚. The shear modulus (Gxy) is moderately sensitive to braid angle change in both the 30-40˚ and 50-60˚ ranges.

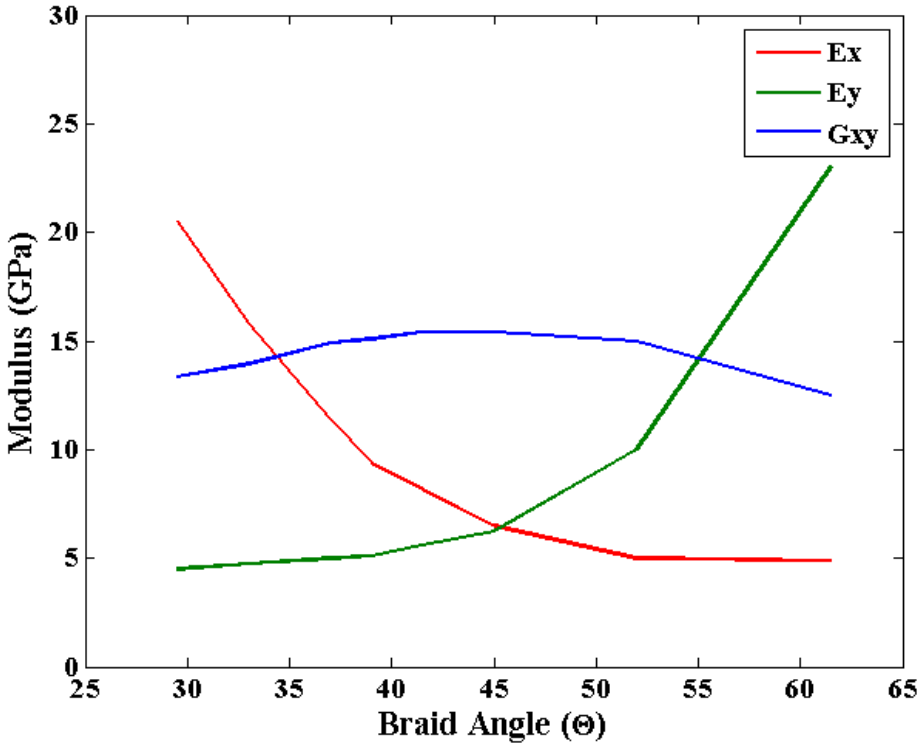

Figure 5.2 - Model predictions of longitudinal, transverse, and shear moduli for Kevlar 49/epoxy closed mesh braids as a function of braid angle recreated from a study by Carey [13]

The objective of this study is to examine, using digital image correlation (DIC), the deformation fields and change in braid angle of braided composite tubes axially loaded

until failure. Images of composite braid sample unit cells will be captured along the length of the samples to determine the effect of imaging position. This study also intends to examine the influence of braid angle changes on experimental measurements and elastic moduli prediction models.

5.2. Procedure and Methods

The experimental setup, sample preparation, and experimental procedure used in this study are similar to those described in chapter 4. Only a brief summary is provided below.

5.2.1. Experimental Setup

The experimental setup is shown in Figure 5.3. A three axis traverse (LES 5, isel Germany AG, Eichenzell, Germany) enables translations in the *x*, *y*, and *z* directions. Mounted on the z-rail of the translation stage is a stereomicroscope (Zeiss Stereo Discovery V8, Carl Zeiss MicroImaging Gmb, Gottingen, Germany) with one charged couple device (CCD) camera (LaVision Imager Intense, LaVision GmbH, Gottingen, Germany) in each of the two camera ports. The stereoscope is aimed at a composite braid sample held within the tensile frame (MTS, Eden Prairie, MN USA) used to apply loads. Loads were measured using a load cell (661.12B ±1000lb, MTS, Minneapolis, MN, USA) with an error of 1.5%. Translation stage motion and image capture triggering are controlled from a PC.

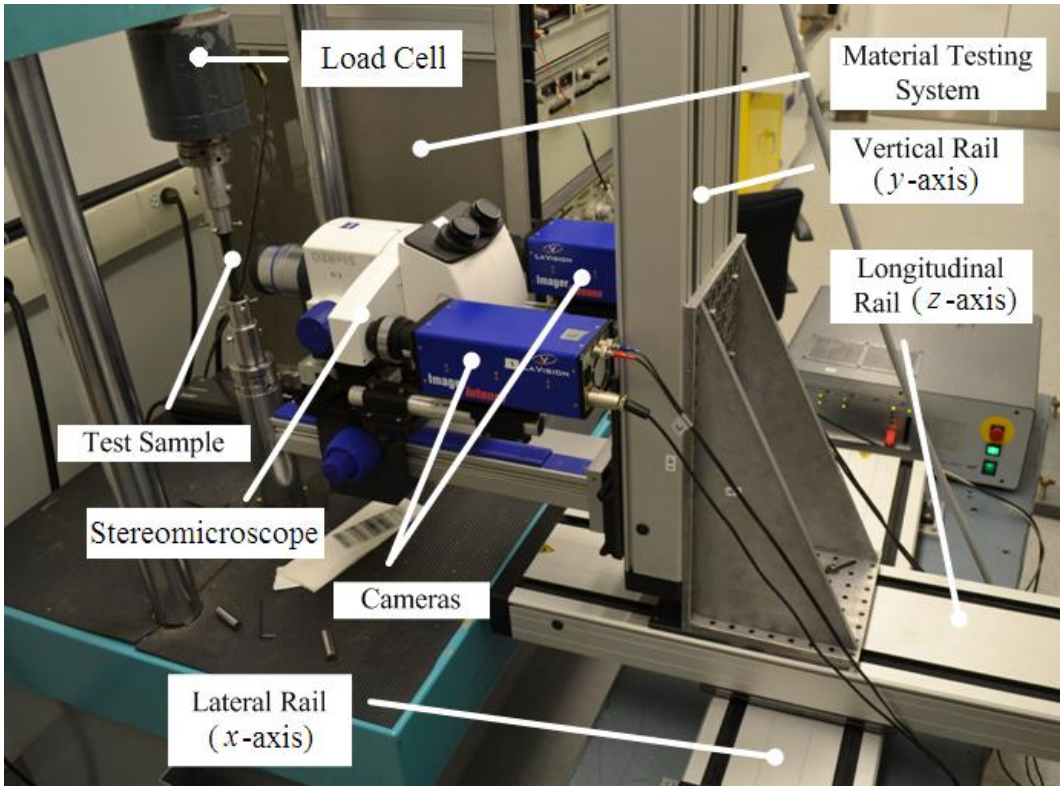

Figure 5.3 – A photo of the experimental setup.

5.2.2. Sample Preparation

A total of 31 tubular composite braid samples were manufactured and tested. The samples were cut to an average gauge length of 90.82±1.54mm with average initial cured braid angles of 42.48±1.96˚. A caliper (Mastercraft, Canadian Tire) was used to measure the sample gauge lengths. The initial braid angle was measured from unloaded composite braid images using DIC reconstructed surfaces.

Preform socks with diamond braid architectures were manufactured using a braider (Steeger USA K80-72, Steeger USA, Inman, South Carolina). The preforms, composed of Kevlar fibers (Kevlar 49, 5680 Denier, Dupont, Mississauga, Ontario, Canada), are fit on a mandrel with an outer diameter of 11.39±0.03mm. A rigid epoxy matrix material, composed of resin (EPON Resin 825, Resolution Performance Products, Pueblo, CO) and a hardener (Ancamine 1482, Air Products and Chemicals, Allentown, PA), mixed at

100:19 weight ratio, was massaged into the performs by hand. The samples were then cured for 2 hours at 110˚C. The braid preforms and cured braid samples are shown in Figure 5.4.

Figure 5.4 – A braid before and after matrix application and curing.

To perform DIC, the surface of the samples must have a randomized contrast pattern. A method, similar to one by Berfield [14], was used to apply a fluorescent speckle pattern to the sample surfaces. A paint mixture of fluorescent paint (Createx 5404, Createx Colors, East Granby CT) and reducer (Createx W100 Wicked, Createx Colors, East Granby CT) at a 2:1 ratio was applied to the surface of the samples using a an airbrush (custom-B micron, Iwata-medea Inc, Portland OR). A 2.64” ring light (Edmund Optics, Barrington, NJ, USA) with a 365nm black-light (Edmund Optics, Barrington, NJ, USA)

provided the light necessary to excite the fluorescent particles. An image of the sample surface in Figure 5.5(a) shows the resulting speckle pattern. The images were filtered to further improve the contrast resulting in the contrast pattern seen in Figure 5.5(b).

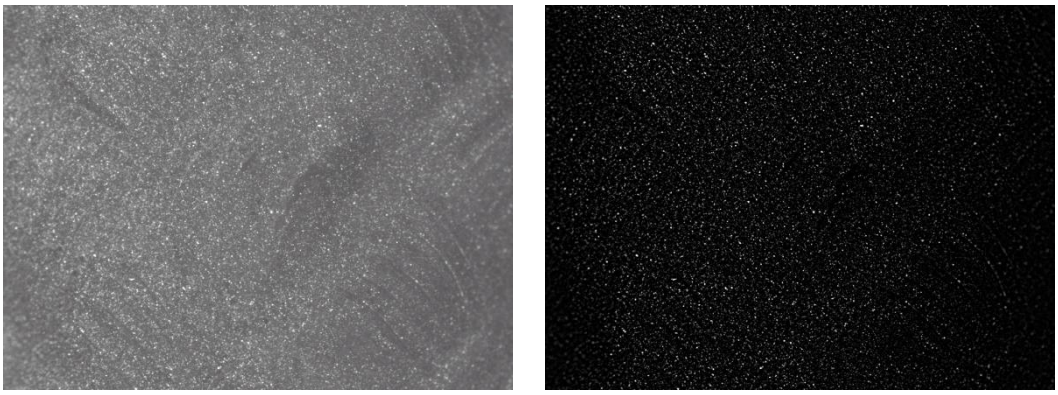

(a) (b)

Figure 5.5 – A stereomicroscope image of the applied speckling (a) before and (b) after filtering.

5.2.3. Post Processing

An image set for one region of one test contains 20 stereo image pairs. These image sets were processed using commercial software (DaVis version 8.0.6 StrainMaster 3D, LaVision GmbH, Gottingen, Germany). To increase image contrast, a subtract sliding minimum non linear filter was applied to all image sets. An example of the resulting image after applying the filter can be seen in Figure 5.5(b). The filtered stereo image pairs are then used to create 3D surface reconstructions through triangulation. Three dimensional DIC is then performed on the image sets to generate 3D displacement vector fields. Displacement vector fields were calculated using multiple passed with decreasing subset size. The first pass used 256x256 pixel subsets and 75% overlap to capture larger motions. The three subsequent passes used 64x64 pixel subsets with 75% overlap to capture smaller motions. Use of smaller subsets and overlap increase processing times but produce more dense displacement vector fields. These 3D displacement vector fields are broken down into a grid with each grid subset containing *x*, *y* and *z* coordinates, as well as displacements in the *x*, *y* and *z* directions.

Strain measurements were calculated from the displacement vector fields. Within a selected area, neighboring displacement vectors area are compared to one another to determine strain. A displacement vector field and the area from which strain was calculated are shown in Figure 5.6.

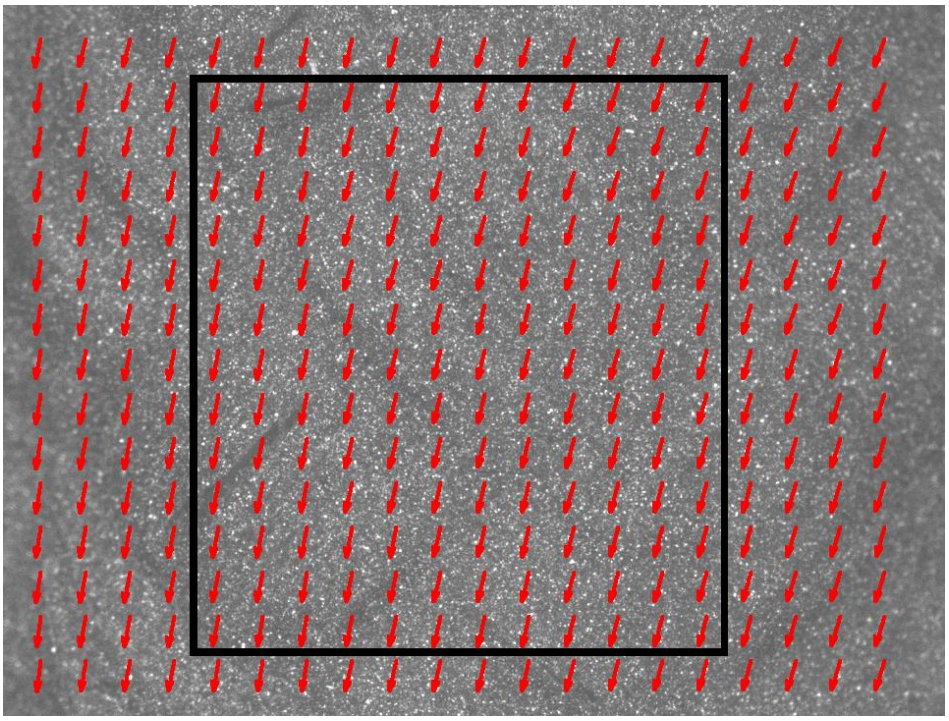

Figure 5.6 – The displacement vector field of a loaded sample and the area from which strain is calculated.

5.2.4. Braid Angle Measurement

Braid angle measurements were made on the captured images during testing. The braid angle was measured from the unit cell centered in the field of view. Points selected from the unit cell were selected as shown in Figure 5.7. The top corner of the central unit cell and the top corner of the unit cell beneath the central unit are connected to create the axial axis line. The left and right points are each connected with the top corner of the unit cell beneath the central unit to give a bottom left and bottom right line, respectively. All three of the lines are represented by vectors. The bottom left and bottom right light are both represented by vector *u*, while the axial axis line is represented by vector *v*. The

magnitudes of the vectors u and v are given by $\|u\|$ and $\|v\|$. Braid angles were calculated using equation 1, which gives the angle (θ) between two vectors. The two vectors, represented by u and υ, have both direction and magnitude in 3D space.

$$Cos\theta = \frac{u \bullet v}{\|u\|\|v\|} \tag{1}$$

The negative braid angle is found using the vectors representing the bottom left and axial line. The positive braid angle is found using the vectors representing the bottom right and axial line. The positive and negative braid angles are averaged to give the braid angle measurement for that frame. For each subsequent frame the selected points at the four corners are tracked using the displacement vector fields. At each frame the slope of the lines are recalculated and braid angle is measured for that frame.

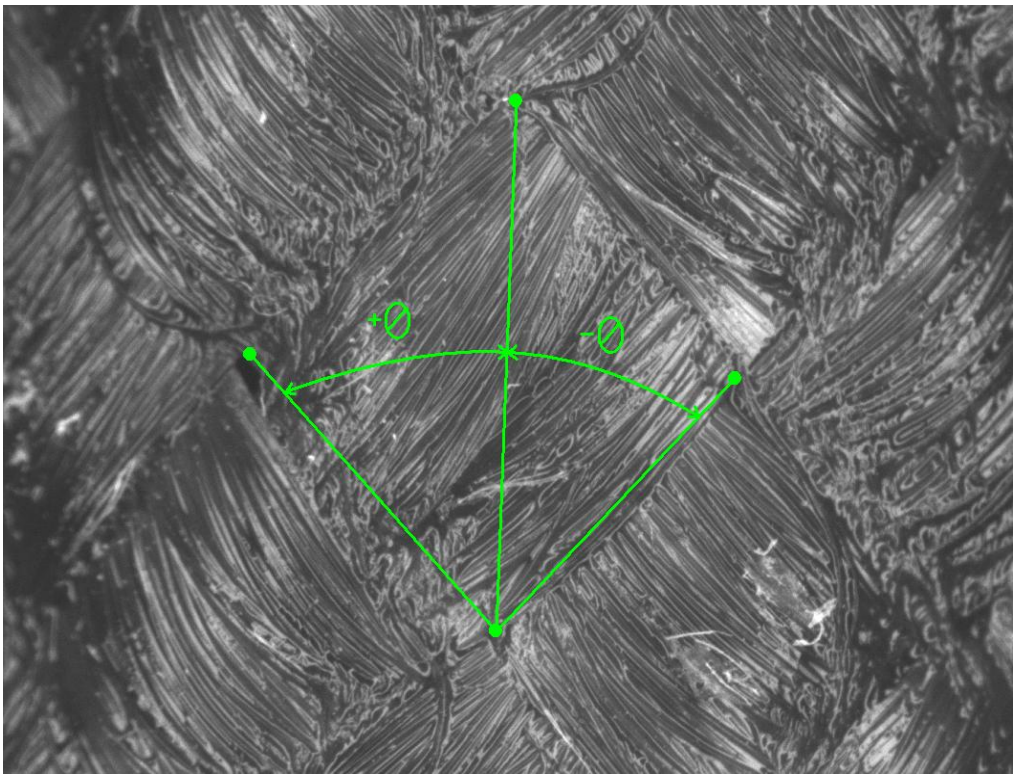

Figure 5.7 – A braid angle measurement diagram showing the four selected points, the lines formed when the points are connected, and the positive and negative braid angle.

After the specimens are speckled, the surface features of the braids become less visible. The corners of the unit cell can become difficult to locate in the raw images, as seen in Figure 5.8(a). A grayscale surface height map, shown in Figure 5.8(b), provides distinguishing surface heights making the corners of the unit cell more distinguishable. The grayscale image was used to select unit cell corner points.

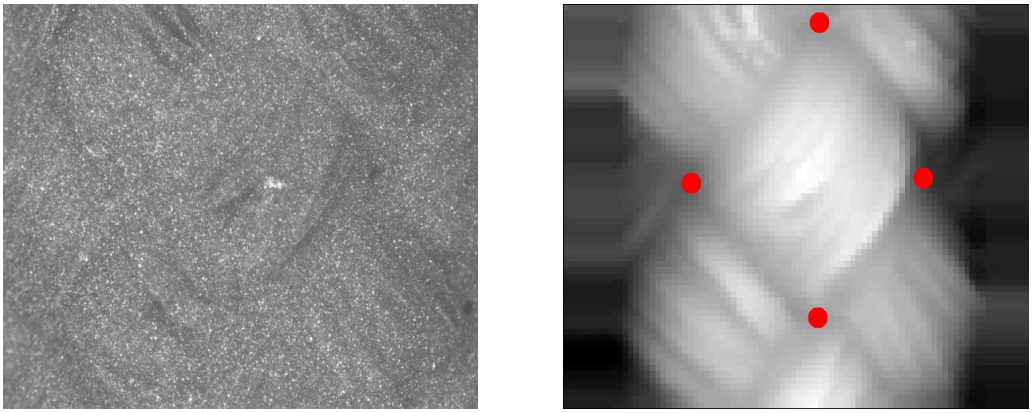

(a) (b)

Figure 5.8 - (a) A raw image of a composite braid captured through the stereomicroscope and the (b) grayscale surface height map with the selected points shown as red dots.

To determine the consistency of chosen points for the braid angle measurement procedure, a repeatability test was performed. The initial braid angle of a single sample was measured ten times from the same image using the braid angle measurement procedure described above. The measurements gave an average braid angle and standard deviation of 45.49±0.54˚.

5.2.5. Braid Angle Measurement Under Tensile Load Test

During testing, measurements were made in three distinct regions each containing its own unit cell as seen in Figure 5.9. Region 1 is located directly at the mid span of the samples. Region 2 and 3 are located above region 1 with a unit cell separating each of regions from one another. For these braids, the distance between the centers of the unit cells in neighboring regions is approximately 9mm. The samples were pulled downward during the tensile test however; the stereomicroscope continues to capture images in the same

locations throughout the test. This caused the sample to shift downward in the field of view of the cameras during loading. Thus unit cells were centered at the top of the stereomicroscope field of view to ensure that the unit cell remained visible. Measurements were made in these three regions and compared to one another to examine the consistency of deformation across the sample.

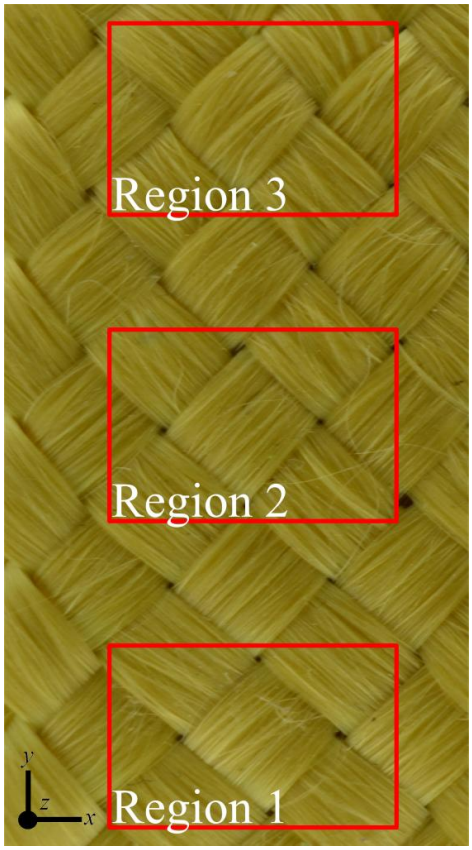

Figure 5.9 – The locations of regions 1, 2, and 3 relative to one another on a single sample. The coordinate system is also shown.

At each of the locations region 1, 2 and 3, a calibration procedure was performed. The calibration was performed using the same method presented and validated in an earlier study [15]. The calibrations were applied to all images captured in each specific region. This was possible as long as the traverse coordinates were the same across all test samples when imaging each specific region. With proper calibration, the testing could proceed.

A sample was placed between the grips of the tensile frame and positioned such that a unit cell at the mid span of the sample fell within region 1. The stereomicroscope was then traversed to regions 2 and 3 to check that unit cells fell within the regions and were in focus. The stereomicroscope was then returned to region 1 where image capture begins. The traverse and the stereomicroscope were coordinated with one another to alternate imaging and scanning of the sample surface. A loop begins with a stereo image pair captured in region 1, followed by traversing the stereomicroscope to region 2. A stereo image pair was then captured at region 2, before the stereomicroscope was traversed to region 3. A stereo image pair is then captured in region 3, before the stereomicroscope is returned to region 1, where the loop ends. A single loop consists of one full scan across the three regions capturing three stereo image pairs. To capture the initiation of loading two full loops are completed without any loading. As the second loop ends, the tensile frame begins to load the sample. Through the test the stereomicroscope and traverse cycle through twenty full loops before the loading ceases. Image sets containing 20 stereo image pairs are captured at each of the three regions for a total of 60 stereo image pairs. Loading was stroke controlled for a total stroke of 2.86mm at a pull rate of 7.6μm/s. The relation between stroke and image set frame is shown in Figure 5.10. The strain experienced by the sample at maximum stroke is expected to be 2.9%. However, samples are expected to experience matrix cracking earlier and failure at strains near1.5% [8]. Capturing the progression of braid angle change through to failure was desired. The stroke was chosen to ensure that samples would fail during image capture.

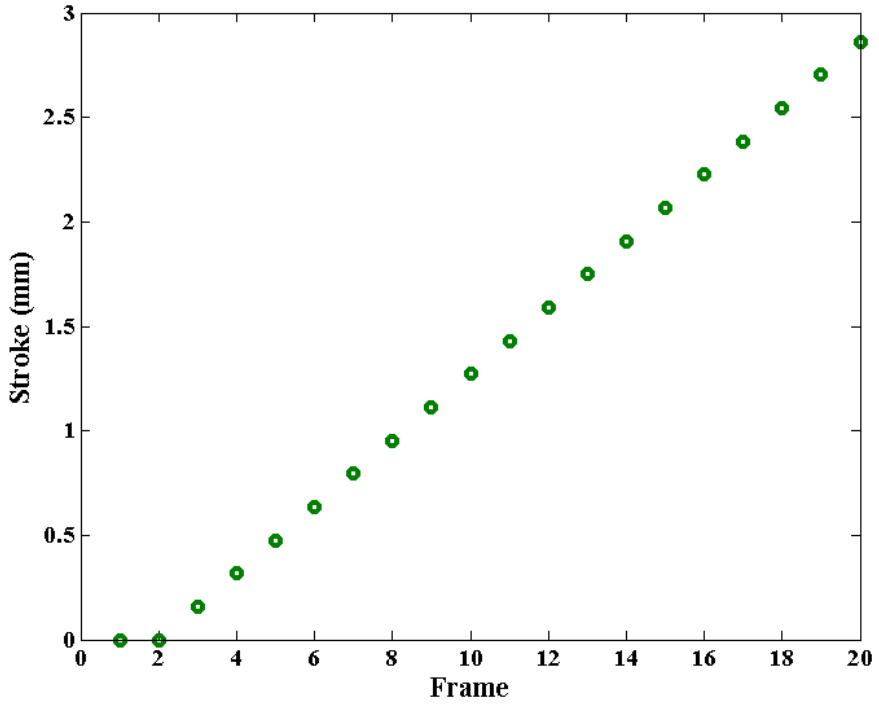

Figure 5.10 – The tensile arm stroke as a function of frame captured by the stereomicroscope.

5.3. Results and Discussion

5.3.1. Deformation Field Results

The progression towards sample failure is highlighted in figure 5.11. During the early loading of the sample at a strain of 0.47%, seen in the Figure 5.11(a) image, matrix cracks do not appear to be present. The displacement vectors corresponding to this frame all travel in the same direction, suggesting the matrix is continuous. The color scale which dictates magnitude of the displacement vectors is given in Figure 5.11(a) and is the same for all displacement vector fields in Figure 5.11. At a strain of 1.20%, the matrix begins to crack, as can be seen highlighted by the red circles in Figure 5.11(b). This begins around frame 13 and 14. The displacements vectors at these frames have increased in magnitude but all continue to travel in a similar direction. At a strain of 1.90%, the matrix cracks continue to propagate and can be seen in the Figure 5.11(c) image. For this image the corresponding displacement vectors are no longer all travelling in the same

direction. The unit cells appear to be moving in directions independent of the neighboring unit cell. At a strain of 2.32% the cracks have propagated and coalesced to cause matrix failure, as seen in the Figure 5.11(d) image. From the displacement vectors we see many diamond shaped regions shifting in different directions. The matrix is no longer effectively holding the structure together, and the fiber tows are able to shift around. These large shifts due to matrix cracking and failure make point tracking difficult and lead to inaccurate braid angle measurements. Thus, measurements made after sample failure were discarded.

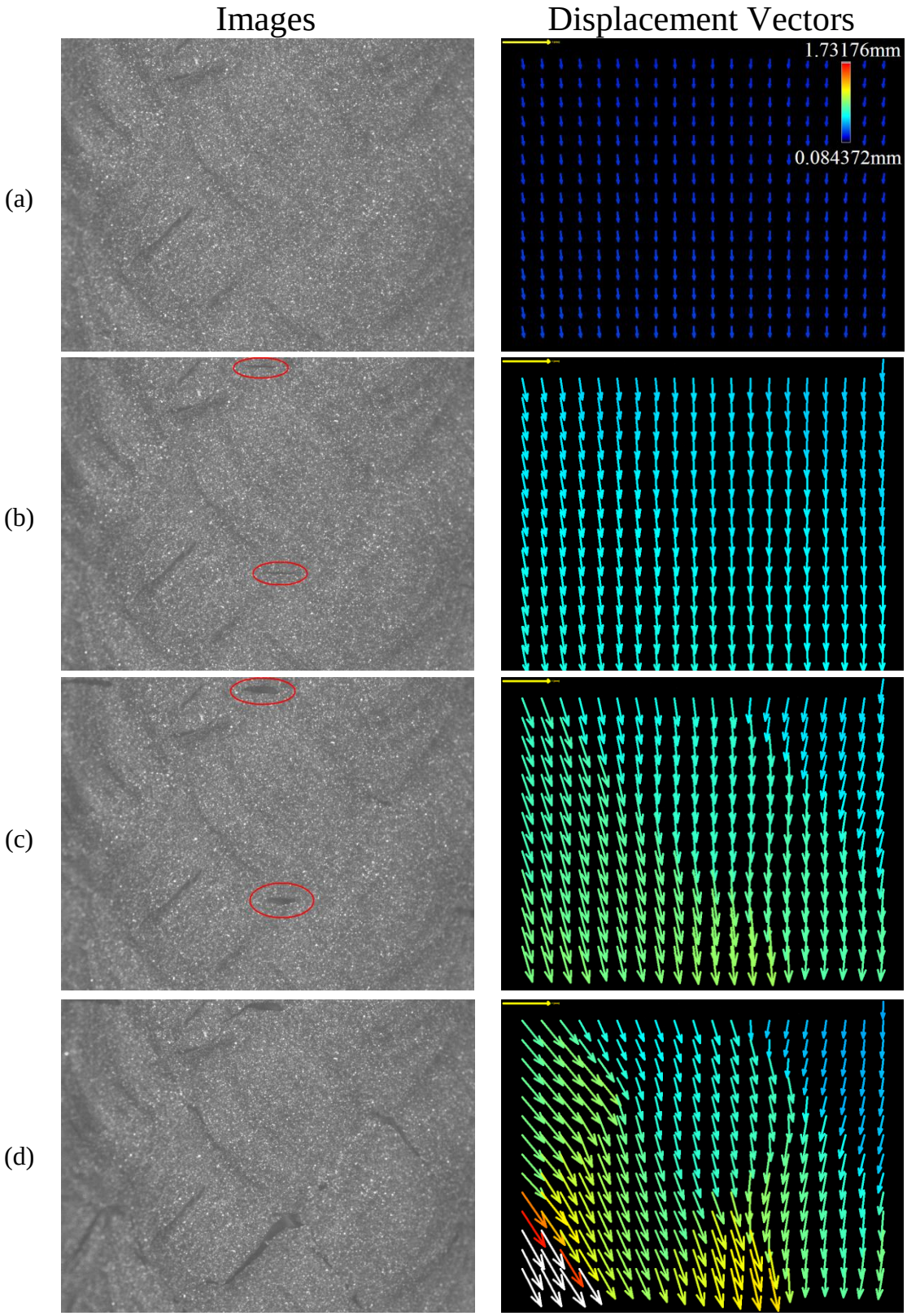

Figure 5.11- Images and the corresponding displacement vector fields at (a) initial loading, (b) crack formation, (c) crack growth, and (d) matrix failure. The colour scale in the first image applies to all subsequent images.

5.3.2. Braid Angle Measurement Under Tensile Load Test Results

In the plot of all angle measurements in region 1, Figure 5.12(a), erratic angle changes can be seen occurring after frame 14. This is because after frame 14 samples begin to fail. All braid angle measurements made after sample failures were removed for all further plots. The resulting data are shown in figure 5.12(b). The average initial braid angles of the cured samples is 42.48±1.96˚. The initial braid angle can range from 39-46˚as a result of the hand resin impregnation technique used to form the composite braid samples. Similar braid angle variations of 44.19±1.63˚ and 50.56±2.16˚ for composite braided tubes samples were found in a study by Ayranci [11]. The samples from the study were also manufactured by hand and used Kevlar fibers.

Sample preforms were manufactured with an expected braid angle of 45˚. The initial braid angles of the cured samples were found to be 42.48±1.96˚. This discrepancy can be attributed to the hand manufacturing process of samples. The preforms are braided on a mandrel with a smaller diameter than the final product. The first change in braid angle occurs when the preforms are placed onto mandrels with the final product diameter. This increase of inner diameter for the braid preforms alters the braid angle. The epoxy is then massaged into the braids by hand, further shifting the braid angle; all efforts are made to ensure the braid angle is set as consistently as possible.

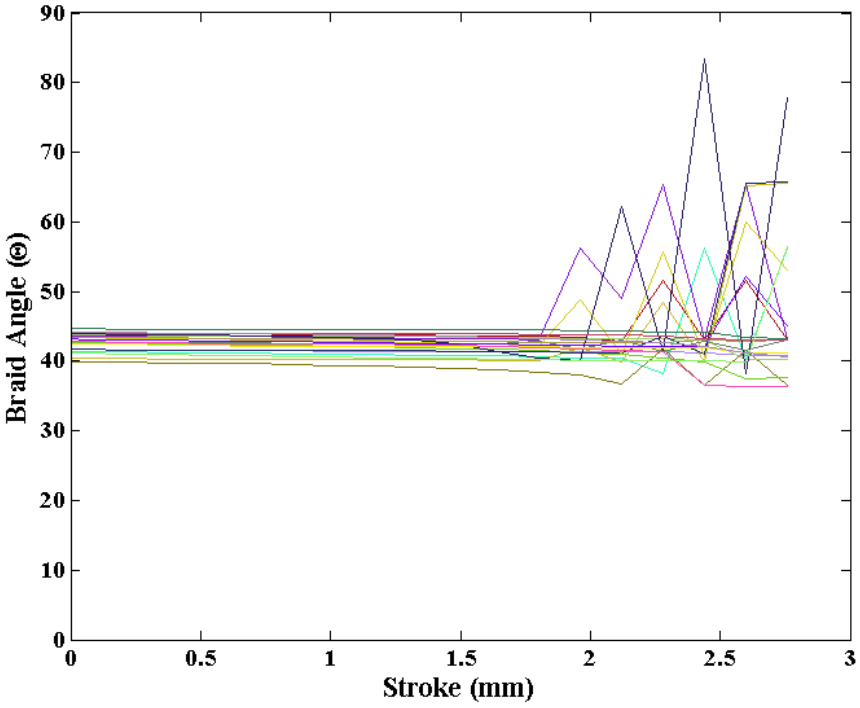

(a)

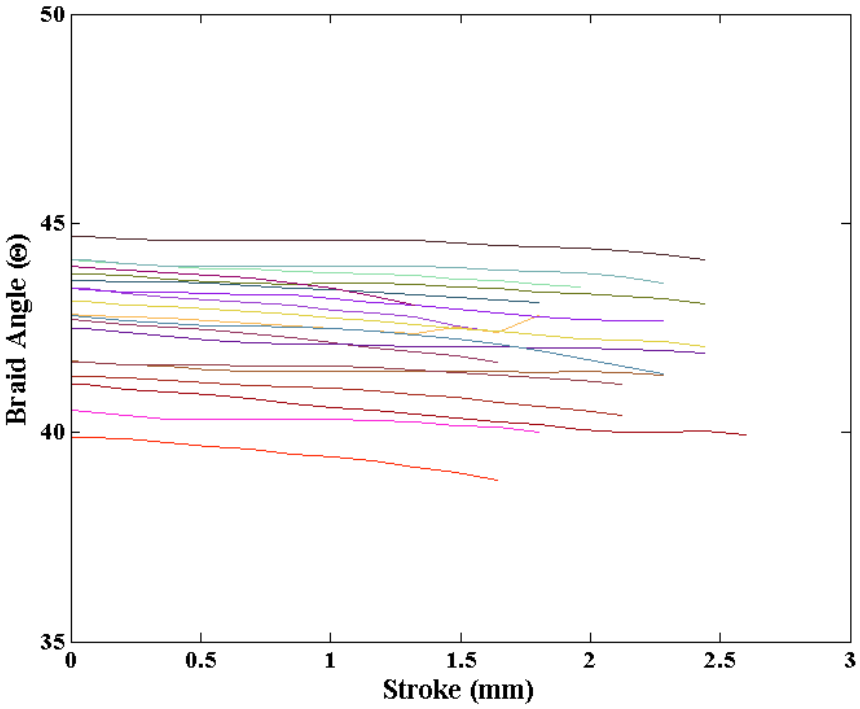

(b)

Figure 5.12 – Braid angles of all samples in region 1 as a function of stroke, (a) including data from all frames and (b) with data after failure removed.

The braid angle at the center of the braid (region 1) can be seen decreasing in Figure 5.13. By the last frame the braid angle has changed by -0.80±0.26˚. The standard deviations increase with each subsequent frame until frame 15, where it reaches its maximum of ±0.33˚. The standard deviation then decreases for the remaining frames, as samples fail and are removed from the pool of averaged samples.

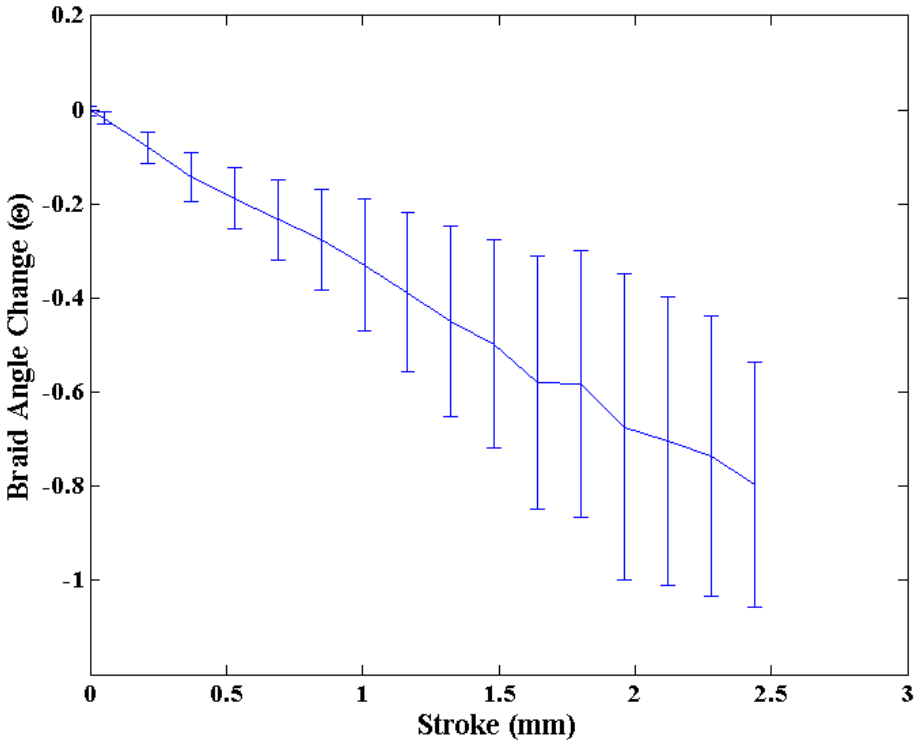

Figure 5.13 - Average total braid angle change of all samples as a function of stroke.

The incremental braid angle change between subsequent frames can be looked at to examine the rate of braid angle change. During initial loading a few larger incremental angle changes of -0.063±0.027˚ occur from frame 3 to 5 as seen in Figure 5.14. The incremental angle change then decreases to -0.043±0.035˚ before gradually becoming larger after frame 8 Both large incremental angle change and standard deviation can be seen in the last two frames. The gradual increase in incremental change followed by a sudden jump in standard deviation is likely caused by crack formation and propagation.

Matrix cracks decrease the ability of the matrix to hold the braid structure together allowing fiber movement and braid angle changes to occur; replicating the expected findings by Ayranci and Carey [2].

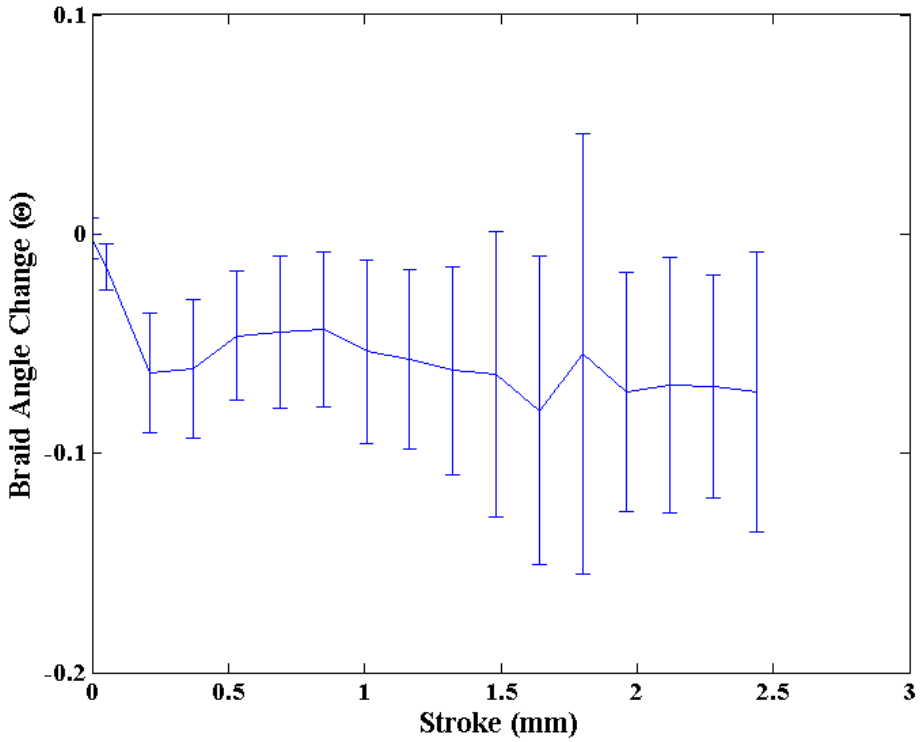

Figure 5.14 – The average incremental braid angle change of all samples as a function of stroke.

The average measured engineering stress strain response and incremental braid angle change of the samples, as a function of strain, can be seen in Figure 5.15. The stress strain response does not appear to be linear. The modulus is lower from a strain range of 0-0.6 approximately. Immediately beyond 0.6% strain, the modulus sharply increases up to 0.9% strain, before gradually dropping until a strain of 1.7%. This response can be related to the braid angle change, which is also plotted against strain. Initially from a range of 0-0.6% strain the braid angle is falling but has not yet changed greatly. The larger braid angle corresponds to a lower modulus as seen in figure 5.2. Beyond 0.6% strain the rate of angle change has decreased, however the braid angle has decreased

more significantly now, thus the modulus increases. As the incremental braid angle change increases beyond strains of 0.9%, we would expect an increase in modulus. However the slope of the stress strain line, or the instantaneous modulus, appears to decrease. This is likely due to the presence of matrix cracking, which could be seen visually at strains of 1.09%, but could begin to occur just before this strain is reached.

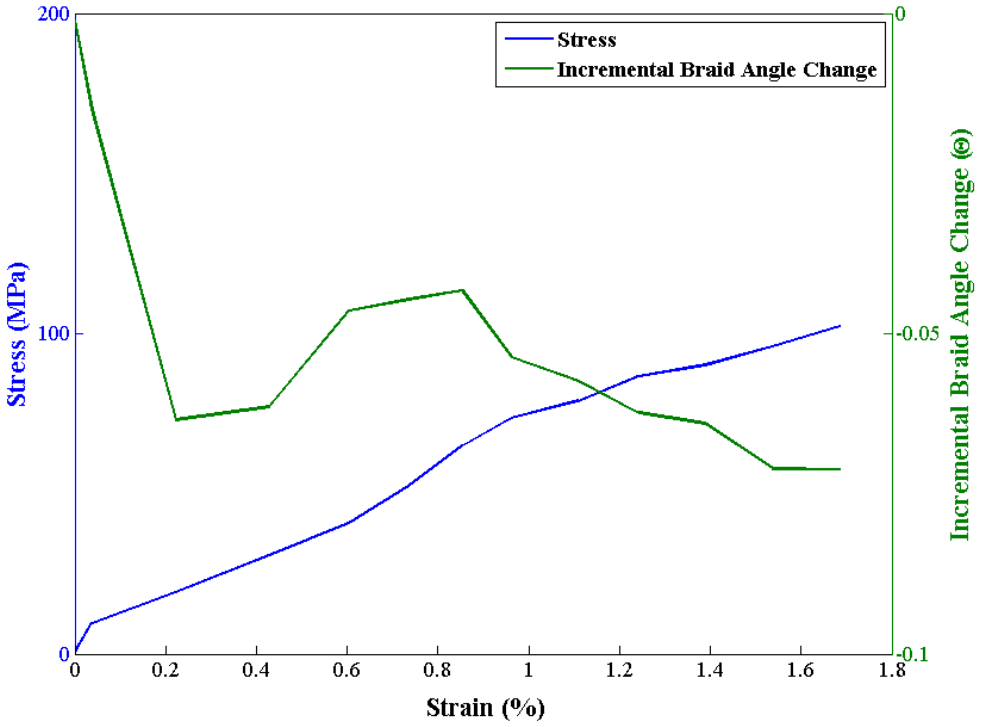

Figure 5.15 –The stress, calculated using initial area, and incremental braid angle change as a function of strain.

To determine if the braid angle change occurred evenly across the braid, angle changes in the three regions were compared, as shown in Figure 5.16. The average braid angle changes reached before sample failure for regions 1, 2, and 3 are -0.80±0.26˚, -0.81±0.33˚, and -0.79±0.37˚ respectively. The largest difference of 2.5% is found between region 2 and 3. Braid angle changes are consistent across the three regions until frame 14. As aforementioned, frame 14 is where sample failure and failed sample data

removal begins. At this point there may be larger deformations occurring in different regions of the braid.

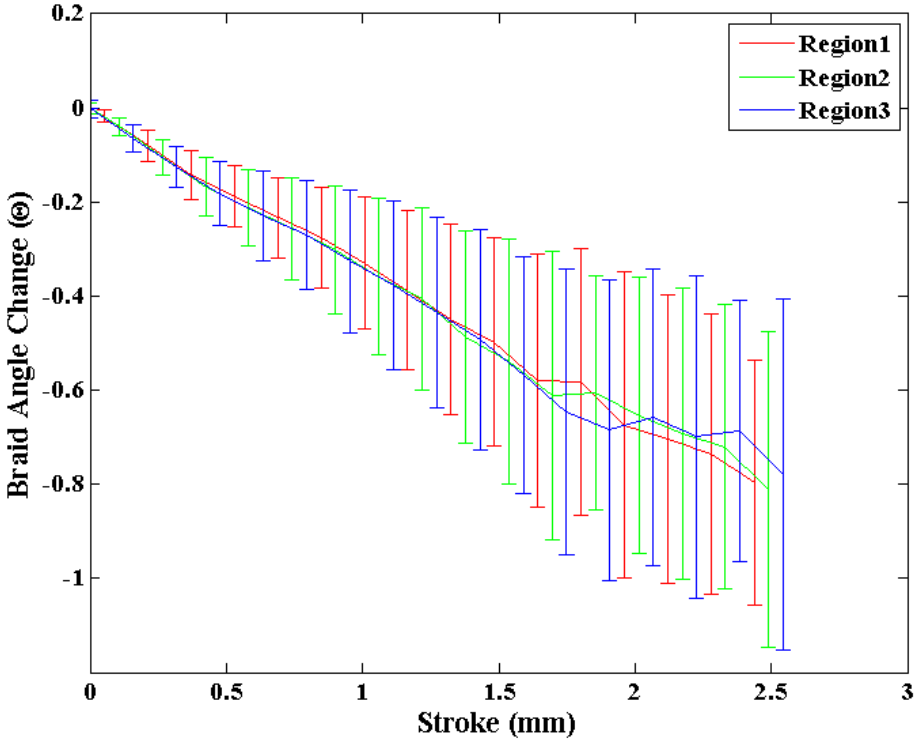

Figure 5.16 – Comparison of total braid angle change between regions as a function of stroke.

Over the duration of the test, the average braid angle decreases by 0.80˚, from an initial angle of 42.7˚ to a final angle of 41.9˚. To determine the effect of braid angle change on composite braid properties, studies that measured material properties as a function of braid angle were examined. Results from a tubular composite braid model for rigid epoxies, adapted from Carey [7], predicting the longitudinal elastic modulus can be seen in Figure 5.2. From the modulus curve, it can be seen that a braid angle change of less than 1 degree within the range of 50-60˚ does not drastically affect the longitudinal modulus of the braid. However, between the range of 30-45˚ the longitudinal modulus is extremely sensitive to a change in braid angle. From 30-35˚ the modulus decreases by 25.2% from 14.3GPa to 10.7Gpa. A braid angle change of 1 degree from 35˚ to 34˚

would increase the modulus from 10.7Gpa to 11.42Gpa. This is a 7% change and can greatly affect how the composite braid behaves. A change of this magnitude could greatly affect the design of any composite braids used in stiffness critical applications. The discrepancy between the experimental and model longitudinal elastic modulus values are near 7%. The changing braid angle and cross sectional area may account for this discrepancy.

In chapter 4, the effects of tubular composite braid radius change on braid behaviour were discussed. One main point was that, as the radius decreases the cross sectional area of the composite braid decreases, thus increasing the stress. The cross sectional area could be further decreased due to a thinning of the composite braid wall thickness resulting from the Poisson's ratio effect. For these samples, a total cross sectional area decrease of -2.12% before sample failure was found. If strain measurements remain the same the stress would increase by 2.12%, and in turn so would the longitudinal elastic modulus. The measured stress directly influences the calculation of elastic and shear moduli. This is compounded with the change in braid angle. The braid angle decreases with axial tension which further increases the longitudinal moduli. When the angle change is compared with the model in Figure 5.2, an increase in modulus of ~7% is expected. If the effects of braid radius and braid angle change are combined, the longitudinal elastic modulus of a braid may change by 9.12% before failure occurs. This change in modulus could be detrimental to the performance of composite braids and must be considered in models and when designing composite braid structures for stiffness critical applications. The effect could be further amplified if elastomeric polymers were used for the composite matrix.

5.4. Conclusions

The deformation fields and braid angle change of composite tubular braids under axial loading was successfully investigated using imaging technology. The initiation and propagation of matrix cracking could be seen occurring in the captured images. Angle measurements were made on images captured with the stereomicroscope system. The initial braid angles ranged between 39-46˚ with an average of 42.48±1.96˚. An average braid angle change of -0.80±0.26˚ was found at the center of the braid. Examination of the incremental braid angle change showed an increase in the rate of angle change as the samples were loaded further. Similar behaviours in terms of angle change and standard deviation were found when regions were compared to each other. The effect of braid angle change on the elastic constants of braided composites was discussed. A braid angle change of one degree can largely affect elastic moduli, depending on the initial braid angle, and should be considered in future design or models. The difference between modeled and experimental modulus values can potentially be attributed to the change in braid angle as well as a decrease in cross sectional area.

5.5. References

[1] C. Ayranci and J. Carey, "2D braided composites: A review for stiffness critical applications," *Composite Structures*, vol. 85, no. 1, pp. 43-58, Sep. 2008.

[2] C. Ayranci, D. Romanyk, and J. P. Carey, "Elastic Properties of Large-Open-Mesh 2D Braided Composites: Model Predictions and Initial Experimental Findings," *Polymer*, 2010.

[3] A. Harte, "Deformation and failure mechanisms of braided composite tubes in compression and torsion," *Acta Materialia*, vol. 48, no. 6, pp. 1259-1271, Apr. 2000.

[4] R. A. Naik, P. G. Ifju, and J. E. Masters, "Effect of Fiber Architecture Parameters," *Journal of Composite Materials*, vol. 28, no. 7, pp. 656-681, 1994.

[5] P. Potluri, A. Manan, M. Francke, and R. Day, "Flexural and torsional behaviour of biaxial and triaxial braided composite structures," *Composite Structures*, vol. 75, no. 1–4, pp. 377-386, Sep. 2006.

[6] L. Xu, S. J. Kim, C.-huat Ong, and S. K. Ha, “Prediction of material properties of biaxial and triaxial braided textile composites,” no. January, 2012.

[7] J. Carey, A. Fahim, and M. Munro, “Predicting Elastic Constants of 2D-Braided Fiber Rigid and Elastomeric-Polymeric Matrix Composites,” *Journal of Reinforced Plastics and Composites*, vol. 23, no. 17, pp. 1845-1857, Nov. 2004.

[8] A. Harte, “On the mechanics of braided composites in tension,” *European Journal of Mechanics - A/Solids*, vol. 19, no. 2, pp. 259-275, Mar. 2000.

[9] Z. Huang, “The mechanical properties of composites reinforced with woven and braided fabrics,” vol. 60, pp. 479-498, 2000.

[10] M. M. Shokrieh and M. S. Mazloomi, “An analytical method for calculating stiffness of two-dimensional tri-axial braided composites,” *Composite Structures*, vol. 92, no. 12, pp. 2901-2905, Nov. 2010.

[11] C. Ayranci and J. P. Carey, “Experimental Validation of a Regression-Based Predictive Model for Elastic Constants of Open Mesh Tubular Diamond-Braid Composites,” *Polymer*, 2011.

[12] J. Carey, M. Munro, and A. Fahim, “Longitudinal Elastic Modulus Prediction of a 2-D Braided Fiber Composite,” *Journal of Reinforced Plastics and Composites*, 2011.

[13] J. Carey, M. Munro, and A. Fahim, “Regression-based model for elastic constants of 2D braided/woven open mesh angle-ply composites,” *Polymer Composites*, vol. 26, no. 2, pp. 152-164, Apr. 2005.

[14] T. A. Berfield, J. K. Patel, R. G. Shimmin, P. V. Braun, J. Lambros, and N. R. Sottos, “Micro- and Nanoscale Deformation Measurement of Surface and Internal Planes via Digital Image Correlation,” *Experimental Mechanics*, vol. 47, no. 1, pp. 51-62, Jan. 2007.

[15] C. K. Leung, G. Melenka, D. S. Nobes, and J. P. Carey, “Validation of DIC as an Effective Tool for Composite Tubular Braid Characterization,” *CSME International Congress 2012*, pp. 1-6, 2012.

Chapter 6: Conclusions and Future Work

The first objective of this thesis was to develop and validate a 3D DIC based optical measurement system. The second objective was to examine key variables, braid angle and radius, for Kevlar-Epoxy tubular composite braids subjected to tensile loading.

6.1 Conclusions

A literature review of textile composite deformation measurement techniques was performed. Contact techniques, such as strain gauges and extensometers, and non contact techniques, such as interferometry and DIC, were looked at. Difficulties in deformation measurement of textile composites due to inhomogeneous deformation fields and rough surface features were detailed. The advantages and limitations of the deformation measurement techniques were evaluated in terms of their ability to deal with textile composites. Interferometry and DIC techniques were found to be capable of dealing with the deformation measurement difficulties inherent in textile composites. However, DIC, having fewer stability requirements, is more robust and was chosen for this study.

The 3D DIC measurement system is capable of evaluating surface deformations using captured stereo image pairs. Three tests were performed to validate the application of the 3D DIC measurement system on composite braids. The accuracy of the measurement system in detecting rigid body motions was assessed. The evaluation of rigid body motions revealed accurate measurements by the system; but with stronger accuracy for in plane motions compared to out of plane motions. The measurement systems ability to accurately measure strain was assessed by matching strain measurement using 3D DIC to extensometer strain measurements. The accuracy of surface reconstruction using the measurement system was examined. The measurement system is able to measure the rigid body motions and strains as well as reconstruct imaged surfaces in 3D.

The measurement system was used to evaluate the change in radius of tubular composite braid samples under axial tension, a unique set of experiments never before done for such composites. The camera stability tests performed on a composite braid show that the camera system traverse accurately and repeatedly returned the stereomicroscope to the same position. Braid radius measurements were made on 3D reconstructed surfaces using two methods; the area method and the band method. The area method results suggest that a decrease in the braid radius occurred. However, the average radius measured using this method fell below the expected range set by the outer and inner radius of the braid samples. The band method results showed a slight increase in radius at the peak measurement locations. The increase of radius could point to a localized negative Poisson's ratio for the composite braids in this limited region of the unit cell geometry. Further investigations are required to conclusively identify this behavior. This finding is a first for 2D braided composites. Band method measurements at the mid and valley locations showed a decreasing radius and fell within the expected range. A decrease in braid radius and wall thickness decreases the cross sectional area of the samples. This in turn increases the stress experienced through the sample cross section, thus affecting the calculation of elastic properties.

The measurement system was used to evaluate the change in braid angle of tubular composite braid samples under axial tension another innovative assessment in composite materials. Measurements were made at three unit cells along the length of the samples. The braid angle was found to decrease evenly across the braid as tensile loading was applied. The angle change with respect to sample strain followed trends seen in the stress strain response of the composite braid samples. Effects of both braid angle and radius change on elastic moduli were examined and help to explain the differences seen between experimental and model values. Change in braid angle and radius affect the elastic

properties of the braided composites and should be included in future models and considered when designing composite braid parts.

6.2 Recommendations

The first recommendation is improvement to the optical system; this would enhance the capabilities and accuracy in characterizing composite braids.

The stereomicroscope used set the cameras at a shallow relative camera angle. The shallow relative camera angle reduces the measurement systems ability to resolve out of plane motions. Using the two cameras with individual zooms would allow for control of the relative camera angle while maintaining the level of magnification. Another limitation of the stereomicroscope is a shallow focal depth. This leads to difficulties in focusing on the entire tubular composite braid sample surface due to surface roughness and curvature. Different optics are required to extend the focal depth and maintain focus on larger areas of the composite braid sample.

The calibration process can be improved to increase the accuracy of 3D DIC measurements. 3D calibrations were performed using a 2D calibration target and translation stages. The translation stages used were manually operated and have a resolution of 25.4μm. Automating the translation stages would eliminate human error. The resolution of the translation stages should be of the same magnitude as the resolution of the 3D DIC measurement system. The measurement system has a resolution of 1.54μm thus a translation stage with a similar resolution would maximize the accuracy of the calibration procedure.

The hand manufacturing process of the composite braids led to variations between samples. This was particularly noticeable in the braid angles. The braids were moved from a braiding mandrel to a Teflon curing mandrel with a different diameter. This

change in diameter of the samples caused the braid angle to shift. This problem can be solved by matching the braiding mandrel diameter to the curing mandrel diameter. The matrix resin was applied to the braided sock preforms using a hand resin impregnation technique. The resin is massaged into the braid, causing further variations to the surface and angle of the braids. Automation of the braiding and resin impregnation process would remove human inaccuracies and result in more consistent samples.

6.3 Future Work

Much work remains in the area of braided composite experimental and modeling research. Further experiments can be performed using the 3D DIC measurement system to expand our understanding of braided composite behavior targeting definition of Poisson's ratio for specific unit cell regions, different polymer types, and geometry.

Current models for composite braids should be developed further using information regarding changes in radius and braid angle. They can be verified with experimental work. Further verification can be achieved using finite element analysis.

A comprehensive study should be carried out to understand the behaviour of closed mesh composite braids. Closed mesh composite braids with variations in braid architecture, braid angle, braid radius, and composite constituents should be tested. Looking at all these variations would provide an understanding of how they affect composite braid properties. Further testing should also be expanded beyond uniaxial loading to include different loading types such as torsion, bending, biaxial, etc. This leads to improved accuracy of models to be used for the design of composite braid parts.

This thesis focused on closed mesh braids. Other types of composite braids should be looked at as well. One variation of composite braid that may result in different behaviours is the use of elastomeric resins. Elastomeric resin composites should be

evaluated and compared to rigid resin composites. Another of these variations is open mesh braids. Models describing open mesh braid behaviours are existent, but are even more limited in experimental validation than closed mesh braids. It would be possible to use the 3D measurement system to study open mesh braid behaviours and provide experimental validation to the models.

The tubular composite braid radius measurements were limited by the optics used. The shallow relative camera angle resulted in poor resolution of out of plane motions. The shallow focal depth limited the amount of surface that could be reconstructed. Optics should be chosen such that a larger amount the sample surface is in focus and can be reconstructed. This could also be expanded with the use of more than two cameras. A larger surface would give the radius circle fitter more data and potentially provide a better sample average radius resulting from sample surface features.

The composite braid 3D surface reconstructions were able to show the sample surfaces in great detail. There are many models that describe the geometric features of composite braids. The surface reconstructions could be used to describe the braid geometry features such as undulation length or angle. The reconstructed surface can also be used to determine the locations of stress concentration. Further examination of surface reconstructions would help to verify geometric models.

Surface reconstruction radius measurements on composite braid samples, using the band method in the peak region, reported an increase in the radius. This could potentially show a negative Poisson's ratio and should be investigated to see if the finding is repeatable.

The 3D DIC measurement system is a non-contact, full field measurement device that can determine the deformations of closed mesh composite braids. The recommendations provided can help to improve the capabilities, accuracy and repeatability of

measurements from the system. The measurement system enables the characterization of composite braid geometry and behaviour for composite braids of varying geometric factors and constituents.

Appendix A: Matlab Programs

A.1 Braid Radius Measurement

The MATLAB programs used for measuring braid radius of full image set are described here. The main function “ImageSetRadiiV2” is shown below.

```
% Author: Cheequn Leung
% email: cheequn@ualberta.ca
% date: March 26, 2012

% Select Vector Set
[FileName, path, FilterIndex] = uigetfile('*.dat');

% Select Surface Set
[FileName, path1, FilterIndex] = uigetfile('*.dat');

% Set # of frames in the set
frames = 20;

% Set measured radii array
Radii=zeros(frames,1);
Peak=zeros(frames,1);

% Open Vector Set
im = 1;
tecplotName = sprintf('%sB000%02d.dat',path,im);

[vector_data, rows, cols] = loadTecPlotFileVectors(tecplotName);

% Create x and y scales
xscale = vector_data(1:cols,1);
yscale = zeros(rows,1);

for i=1:rows,
ysc = vector_data(1+i*cols-cols,2);
yscale(i,:) = ysc;
end

% Determine the mm/pixel conversion in the x and y directions
xconv = (max(xscale) - min(xscale)) / cols;
yconv = (max(yscale) - min(yscale)) / rows;

% Set tracking vector arrays
dT = zeros(frames,2);

% Place z, u, v, and w data into grids
[zgrid, ugrid, vgrid, wgrid] = vectorgrid(rows, cols,
tecplotName);

% Bring up zscale image and select tracking points 1-3
```

```
figure;
imagesc(xscale,-yscale,zgrid)
colormap(gray)

[a,b]=ginput(1);
hold on;
plot(a,b, 'O','LineWidth',2,'Color','k');

b(1) = -b(1);

% Loop to measure the radius in each frame
for im = 1:frames,

% Open Vector Set
tecplotName = sprintf('%sB000%02d.dat',path,im);

[vector_data, rows, cols] = loadTecPlotFileVectors(tecplotName);

% Place z, u, v, and w data into grids
[zgrid, ugrid, vgrid, wgrid] = vectorgrid(rows, cols,
tecplotName);

% Set window size for tracking boxes
winsize = 1;

% Convert points to grid locations
[diff, x1] = min(abs(xscale-a(1)));
[diff, y1] = min(abs(yscale-b(1)));

% Set max and min bounds
x1min = x1-winsize;
x1max = x1+winsize;
y1min = y1-winsize;
y1max = y1+winsize;

% Populate tracking vector matrices and find the average
dT(im,1) = mean2(ugrid(y1min:y1max,x1min:x1max));
dT(im,2) = mean2(vgrid(y1min:y1max,x1min:x1max));

% New positions of points after displacement vectors applied
if im ==1
% a(1) = a(1) + dT(im,1);
b(1) = b(1) - dT(im,2);

else
% a(1) = a(1) + (dT(im,1) - dT(im-1,1));
b(im) = b(im-1) + (dT(im,2) - dT(im-1,2));

end

% Measure the radii
[Radii, Peak, surfvector_data] = measureradiusV2(im, path1,
xscale, dT, cols, b, Radii, Peak);
```

```
end
```

A total of three functions are called within this program. These functions are: loadTecPlotFileVectors, Vectorgrid, and measureradiusV2 in order of appearance. The program first sets correct pathing by asking the user to select the location of the displacement vector and surface reconstruction data sets. The number of frames within the sets is defined. Arrays are then created where measured values will be stored. The actual radius measurement is made in the function measureradiusV2. The vector data as well as numbers of columns and rows required are extracted from the vector set using the loadTecPlotFileVectors function. Using the vector data and number of rows and columns the *x* and *y* direction scales are set. An array is created to store displacement vectors for point tracking. The vectorgrid function is then used to place the *z* coordinates and vector data into grids that reflect the *x*, *y* spacing of the images. A surface height map is then brought up. The point selected on the image will determine where the radius measurements will be taken. A loop is set to run through all files within the set. The variable winsize determines the size of the window from which displacement vectors are averaged for point tracking. The points selected (coordinates [a,b]) are converted to a specific location on a grid. Using the variable winsize, the tracking vector window limits are set. The tracking vector dT is then populated and used to determine the new point in the subsequent frame. The radius is then measured using measureradiusV2.

Actual measurement of the braid radius occurs in the function measureradius V2. The function is shown below:

```
function [Radii, Peak, surfvector_data] = measureradiusV2(im,
path1, xscale, dT, cols, b, Radii, Peak)

% The function 'measureradius' measures the radius of a 3D
cylindrical
```

```
% surface. Firstly the excess information on the left and right
of the image are removed. Coordinates across the sample surface
are fit to a circle.

% Open files and extract data
tecplotName = sprintf('%sB000%02d.dat',path1,im);

[x, y, z, surfvector_data, surfrows, surfcols] =
loadTecPlotFile(tecplotName);

% Set yscale for surface file
for j=1:surfrows,
ysc = surfvector_data(1+j*surfcols-surfcols,2);
surfyscale(j,:) = ysc;
end

% Determine measurement row of interest
[diff, topn] = min(abs(surfyscale-b(im)));

% Determine Vector to Surface row conversion
rowconv = surfcols/cols;

% Determine the mm spacing per surface set column
mmpercol = (xscale(cols,1) - xscale(1,1))/surfcols;

% Convert vector rows to surface rows
% topn = round(topn(im)*rowconv);

% Set spacing between measurement rows
spacing = 10;
counts = 2;

for i = 1:counts

n = topn + (spacing*i) - (spacing*(counts/2));

% Set limits for acquisition of data from vector_data
minbound = 1+surfcols*n;
maxbound = 1+surfcols*(n+1);

% break data into xdata and zdata (1384 or 1400)
locX = surfvector_data(minbound:maxbound,1);
locZ = surfvector_data(minbound:maxbound,3);

% Determine lateral image shift (X-direction)
xshift = round(dT(im,1)/mmpercol);

% Select desired data within a row (left and right limits)
left = 200 + xshift;
right = 900 + xshift;

locX = locX(left:right);
locZ = locZ(left:right);
```

```
% run circle fit for top
circfit(locX,locZ);

% Create data for a circle + noise
  th = linspace(0,2*pi,400)';
  R=0;
  sigma = R/10;
  x = locX;
  y = locZ;
%
 figure;
  plot(x,y,'o'), title(' measured points')
   pause(1)

% reconstruct circle from data
   [xc,yc,Re,a] = circfit(locX,locZ);
      xe = Re*cos(th)+xc; ye = Re*sin(th)+yc;

     plot(x,y,'o',[xe;xe(1)],[ye;ye(1)],'-
.',R*cos(th),R*sin(th)),
     title(' measured fitted and true circles')
     legend('measured','fitted','true')
     text(xc-R*0.9,yc,sprintf('center (%g , %g );
R=%g',xc,yc,Re))
     xlabel x(mm), ylabel z(mm)
     axis equal

R(i,1) = Re;
P(i,1) = max(locZ);
end

% write radius measurements to output file
Radii(im,1) = mean(R);
Peak(im,1) = mean(P);
end
```

The function first extracts the surface vector data and their corresponding *x*, *y*, and *z* coordinates. The number of columns and rows are also extracted and are used to determine the scale in the *y* direction. The variable rowconv gives the conversion factor between vector file and surface file rows. The spacing between columns is determined in millimeters. The selected vector file row is converted into a surface file row. The spacing and counts determine the spacing between measurements and the number of measurements to be made respectively. A loop is set to make repeated radius measurements depending on the spacing and counts. The vertical limits for the cross

section are determined by the minbound and maxbound. The x and z coordinates of points along the surface cross section are determined as the variables locX and locZ. The variable xshift is the shift in the lateral direction that should be applied to the bounds to match lateral motion of the selected point. The left and right bounds are set here at and the xshift is applied to the boundaries. The points from the cross section are cutoff depending on the left and right limits. The point data is then input into the circle fitter function circfit. The cross section surface and the estimated circle can be plot. However, a plot will be created for every measurement made. Thus plots should only be made when there are a small number of measurements to be made. The radius of the estimated circle, R, determined from the circfit function is averaged for all measurements and recorded into the radii array Radii.

A.2 Braid Angle Measurement

To measure braid angles of full image set the function “ImageSetAngleFinderV2” was used. The code is shown below:

```
% Braid Angle Finder for Full Image Sets
% Cheequn Leung
% March 26, 2012

% Set # of frames in the set
frames = 20;

% Set main loop
for im = 1:frames,

    if im == 1
        % Set path 1 to vector set
[FileName, path1,FilterIndex] = uigetfile('*.dat');

tecplotName = sprintf('%sB000%02d.dat',path1,im);

[vector_data, rows, cols] = loadTecPlotFile(tecplotName);

% Create x and y scales
xscale = vector_data(1:cols,1);
yscale = zeros(rows,1);

for i=1:rows,
ysc = vector_data(1+i*cols-cols,2);
yscale(i,:) = -ysc;
end

% Set measured angle array
Angles = zeros(frames,3);

% Set tracking vector arrays
dB = zeros(frames,2);
dL = zeros(frames,2);
dT = zeros(frames,2);
dR = zeros(frames,2);

% Place z, u, v, and w data into grids
[zgrid, ugrid, vgrid, wgrid] = vectorgrid(rows, cols,
tecplotName);

% Bring up zscale image and select tracking points 1-4
imagesc(xscale,yscale,zgrid)
colormap(gray)
[a,b]=ginput(1);
hold on;
plot(a,b, 'O','LineWidth',2,'Color','r');
```

```
[c,d]=ginput(1);
hold on;
plot(a,b,c,d,'O','LineWidth',2,'Color','r');

[e,f]=ginput(1);
hold on;
plot(a,b,c,d,e,f,'O','LineWidth',2,'Color','r');

[g,h]=ginput(1);
hold on;
plot(a,b,c,d,e,f,g,h,'O','LineWidth',2,'Color','r');

a(2)=c(1);
b(2)=d(1);
a(3)=e(1);
b(3)=f(1);
a(4)=g(1);
b(4)=h(1);

clearvars d e f g h;

% Set point location arrays
ploc = zeros(frames,12);
c = zeros(1,4);

[dB, dL, dT, dR, Angles, ploc, a, b, c, xscale, yscale, rows,
cols] = measureangleV2(path1, im, a, b, c, xscale, yscale,
Angles, ploc, dB, dL, dT, dR);

clearvars vector_data i ysc
    else

[dB, dL, dT, dR, Angles, ploc, a, b, c, xscale, yscale, rows,
cols] = measureangleV2(path1, im, a, b, c, xscale, yscale,
Angles, ploc, dB, dL, dT, dR);

    end
end
```

A total of three functions are called within this program. These functions are: loadTecPlotFileVectors, vectorgrid, and measureangleV2 in order of appearance in the program. The functions loadTecPlotFileVectors and vectorgrid were also used when measuring braid radii and are described in appendix A.

Firstly, the number of frames within the image set is selected. For the tests performed this was 20 frames. A loop is set to run through all images within the set. The correct pathing

to reach the image files is set using uiget and sprint. The displacement vector data as well as the number of rows and columns required to store the data is extracted using the loadTecPlotFileVectors function. The image scales in the *x* and *y* directions are then set. The measured angle array as well as the tracking vector arrays for the four selected unit cell points is created. These are defined by dB, dL, dT, and dR (bottom, left, top, and right). The vector grid function is then used to place surface height (z) and displacement vector data into grids. A grayscale image is then brought up that is dependent on the surface height (z). On this image points are to be selected at the corners of the unit cell starting with the bottom corner, moving in a clockwise direction, and ending on the right corner. The grayscale image and selected points is shown below in Figure A.1.

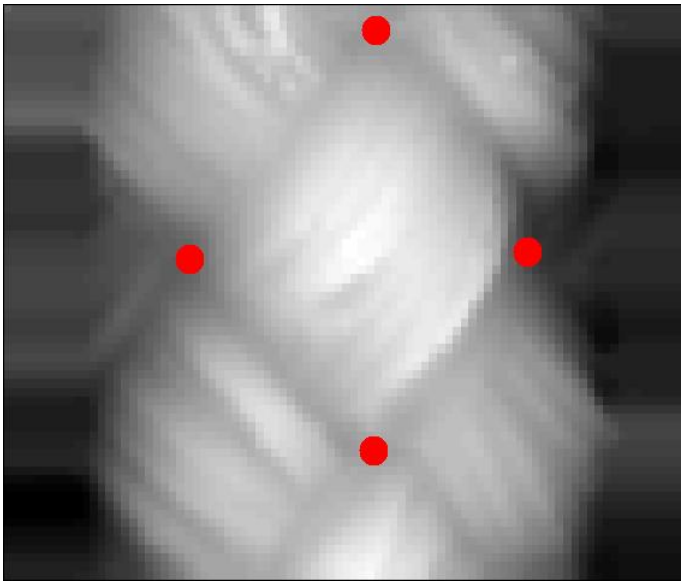

Figure A.1 - A grayscale surface height image with red dots indicating the selected points.

The selected points are fed into the function measureangleV2, which is used to measure the angle between the vectors formed by the selected points. The first loop set continues to loop through until the angle for all images in the image set are measured.

The actual braid angle measurement is made in the function measureangleV2. The function is shown below:

```
function [dB, dL, dT, dR, Angles, ploc, a, b, c, xscale, yscale,
rows, cols] = measureangleV2(path1, im, a, b, c, xscale, yscale,
Angles, ploc, dB, dL, dT, dR)

% measureangle - Determines the unit cell braid angle in each
image of an image set

% Input Tecplot data
tecplotName = sprintf('%sB000%02d.dat',path1,im);

[vector_data, rows, cols] = loadTecPlotFile(tecplotName);

% Place z, u, v, and w data into grids
[zgrid, ugrid, vgrid, wgrid] = vectorgrid(rows, cols,
tecplotName);

% Determine the mm/pixel conversion in the x and y directions
xconv = (max(xscale) - min(xscale)) / cols;
yconv = (max(yscale) - min(yscale)) / rows;

% Set window size for tracking boxes
winsize = 1;

% Convert points to grid locations
[diff, x1] = min(abs(xscale-a(1)));
[diff, y1] = min(abs(yscale-b(1)));

[diff, x2] = min(abs(xscale-a(2)));
[diff, y2] = min(abs(yscale-b(2)));

[diff, x3] = min(abs(xscale-a(3)));
[diff, y3] = min(abs(yscale-b(3)));

[diff, x4] = min(abs(xscale-a(4)));
[diff, y4] = min(abs(yscale-b(4)));

% Set max and min bounds
x1min = x1-winsize;
x1max = x1+winsize;
y1min = y1-winsize;
y1max = y1+winsize;

x2min = x2-winsize;
x2max = x2+winsize;
y2min = y2-winsize;
y2max = y2+winsize;

x3min = x3-winsize;
x3max = x3+winsize;
y3min = y3-winsize;
y3max = y3+winsize;

x4min = x4-winsize;
x4max = x4+winsize;
```

```
y4min = y4-winsize;
y4max = y4+winsize;

% Determine z coordinates for points
if im ==1

c(1) = mean2(zgrid(y1min:y1max,x1min:x1max));
c(2) = mean2(zgrid(y2min:y2max,x2min:x2max));
c(3) = mean2(zgrid(y3min:y3max,x3min:x3max));
c(4) = mean2(zgrid(y4min:y4max,x4min:x4max));
else
end

% Populate tracking vector matrices and find the average
dB(im,1) = mean2(ugrid(y1min:y1max,x1min:x1max));
dB(im,2) = mean2(vgrid(y1min:y1max,x1min:x1max));
dB(im,3) = mean2(wgrid(y1min:y1max,x1min:x1max));

dL(im,1) = mean2(ugrid(y2min:y2max,x2min:x2max));
dL(im,2) = mean2(vgrid(y2min:y2max,x2min:x2max));
dL(im,3) = mean2(wgrid(y2min:y2max,x2min:x2max));

dT(im,1) = mean2(ugrid(y3min:y3max,x3min:x3max));
dT(im,2) = mean2(vgrid(y3min:y3max,x3min:x3max));
dT(im,3) = mean2(wgrid(y3min:y3max,x3min:x3max));

dR(im,1) = mean2(ugrid(y4min:y4max,x4min:x4max));
dR(im,2) = mean2(vgrid(y4min:y4max,x4min:x4max));
dR(im,3) = mean2(wgrid(y4min:y4max,x4min:x4max));

% New positions of points after displacement vectors applied
if im ==1
a(1) = a(1) + dB(im,1);
b(1) = b(1) - dB(im,2);
c(1) = c(1) - dB(im,3);

a(2) = a(2) + dL(im,1);
b(2) = b(2) - dL(im,2);
c(2) = c(2) - dL(im,3);

a(3) = a(3) + dT(im,1);
b(3) = b(3) - dT(im,2);
c(3) = c(3) - dT(im,3);

a(4) = a(4) + dR(im,1);
b(4) = b(4) - dR(im,2);
c(4) = c(4) - dR(im,3);

else
a(1) = a(1) + (dB(im,1) - dB(im-1,1));
b(1) = b(1) - (dB(im,2) - dB(im-1,2));
c(1) = c(1) + (dB(im,3) - dB(im-1,3));

a(2) = a(2) + (dL(im,1) - dL(im-1,1));
```

```
b(2) = b(2) - (dL(im,2) - dL(im-1,2));
c(2) = c(2) + (dL(im,3) - dL(im-1,3));

a(3) = a(3) + (dT(im,1) - dT(im-1,1));
b(3) = b(3) - (dT(im,2) - dT(im-1,2));
c(3) = c(3) + (dT(im,3) - dT(im-1,3));

a(4) = a(4) + (dR(im,1) - dR(im-1,1));
b(4) = b(4) - (dR(im,2) - dR(im-1,2));
c(4) = c(4) + (dR(im,3) - dR(im-1,3));
end

% Determine slopes of lines between points
pleft = [a(1)-a(2),b(1)-b(2),c(1)-c(2)]; % Slope of left line
pright = [a(1)-a(4),b(1)-b(4),c(1)-c(4)]; % Slope of right line

%find slope of axial line
paxial = [a(1)-a(3),b(1)-b(3),c(1)-c(3)];

% determine the braid angles
magleft = sqrt(pleft(1)^2+pleft(2)^2+pleft(3)^2);
magright = sqrt(pright(1)^2+pright(2)^2+pright(3)^2);
magaxial = sqrt(paxial(1)^2+paxial(2)^2+paxial(3)^2);

degL = acosd(dot(pleft,paxial)/(magleft*magaxial));
degR = acosd(dot(pright,paxial)/(magright*magaxial));

% write radius measurements to output file
degavg = (degL+degR)/2;

Angles(im,1) = degL;
Angles(im,2) = degR;
Angles(im,3) = degavg;

ploc(im,1) = a(1);
ploc(im,2) = b(1);
ploc(im,3) = c(1);
ploc(im,4) = a(2);
ploc(im,5) = b(2);
ploc(im,6) = c(2);
ploc(im,7) = a(3);
ploc(im,8) = b(3);
ploc(im,9) = c(3);
ploc(im,10) = a(4);
ploc(im,11) = b(4);
ploc(im,12) = c(4);

end
```

First in this function the vector file is opened. The vector data as well as the number of rows and columns in the data set are extracted. The displacement vectors and the surface

heights are placed into the appropriate grids. The variables xconv and yconv are the mm/pixel conversion in the *x* and *y* direction. The winsize determines the size of the window for capturing tracking vectors. The next couple lines convert the selected points from the main program into grid coordinates. The vector tracking window min and max bounds are set. Using the min and max bounds the z coordinates and tracking vectors are averaged and represented by the variables c, dB, dL, dT, and dR. The averaged displacements are added to the coordinates of each point. Using the points the slopes of the left, right and axial lines are determined. Using the slopes the vectors are calculated and used to determine the left and right braid angles. The two angles are averaged and stored in the array Angles. The array ploc gives the *x*, *y*, and *z* coordinates of each point through all subsequent frames. It is used to ensure that the vector tracking corresponds with what is seen during testing.